

OPTICAL AND ELECTRO-OPTIC PROPERTIES OF TRANSITION METAL
DICHALCOGENIDE AND INORGANIC PEROVSKITE NANOMATERIALS

A Dissertation

by

DANIEL PEYTON ROSSI

Submitted to the Office of Graduate and Professional Studies of
Texas A&M University
in partial fulfillment of the requirements for the degree of

DOCTOR OF PHILOSOPHY

Chair of Committee,	Dong Hee Son
Committee Members,	Timothy Hughbanks
	Simon North
	Choongho Yu
Head of Department,	Simon North

August 2018

Major Subject: Chemistry

Copyright 2018 Daniel Rossi

ABSTRACT

The study of semiconductor nanocrystals and quantum dots with controlled size and shape offers a unique platform to study the effects of morphological and structural asymmetries, as well as quantum confinement on the optical properties of semiconductors. In the first part of this work we will study the asymmetric optical, vibrational, and electro-optic properties in transition metal dichalcogenide (TMDC) nanodiscs, resulting from the strong asymmetry in the crystal structure. The second part of this work will focus on the carrier dynamics in perovskite quantum dots and doped nanoparticles, materials currently being investigated for next generation optical and optoelectronic devices. In both material systems we will rely on the use of steady state and time resolved absorption spectroscopy to study carrier dynamics and vibrational properties, as well as electro-optic studies to probe the electronic properties in these novel semiconductor systems.

The effects of anisotropy are observed in the optical and electronic properties in the TMDC nanodiscs. In laterally confined TMDC nanodiscs, photoexcited charge carriers couple preferentially to the anisotropic in-plane phonons, and the carrier relaxation, band transport, and charge transfer properties are affected by the anisotropy of the material. The effect of anisotropy can also be observed in the macroscopic properties, including the electronic coupling between nanodiscs in stacked assemblies, and the anisotropy of electronic properties such as the induced dipole moment.

The carrier dynamics in perovskite quantum dots and doped nanoparticles were studied via time resolved absorption and photoluminescence. In the Mn^{2+} doped CsPbCl_3 nanoparticles, the exciton-Mn energy transfer time was extracted ($\sim 300\text{ps}$), roughly twice as long compared with Mn^{2+} doped CdSe suggesting weaker exciton-Mn exchange coupling. Taking advantage of recently developed synthetic protocol for the preparation of highly monodispersed CsPbBr_3

quantum dots, we studied confinement induced carrier dynamics. The turning on of formally forbidden transitions due to broken optical selection rules after photo excitation was observed in confined CsPbBr₃ quantum dots, resulting from the formation of a dipole moment in the presence of electron-hole pairs.

ACKNOWLEDGEMENTS

I would like to thank my graduate advisor Dr. Son for providing an environment where I learned how to succeed as both an independent researcher and as a member of a group. Dr. Son gives a certain amount of space for us to grow as independent thinkers, providing us with useful direction, but also with the motivation to independently learn about subjects directly and indirectly related to our research. For me, this balance between independent and directed research has proved ideal. One of the most endearing aspects of Dr. Sons research group is the collaborative effort we make as a group towards advancing each project. Dr. Son has the uncanny ability to direct the efforts of many students to tackle related topics in a complete fashion. He fosters an environment of teamwork which I believe could be a template for any research program. My time here will provide a tough standard by which I will always compare future work environments.

I would also like to thank Dr. Plass, my undergraduate research advisor and general chemistry teacher. Dr. Plass had perhaps the most profound impact on my academic career and my future, being the first teacher to inspire me academically. Without Dr. Plass I surely would not have studied chemistry and never have developed an interest in scientific research. To this day, Dr. Plass continues to be a motivating figure in my life.

I would also like to thank my mother, father, and brother, who supported me through my long education. Without their continued guidance throughout my early and continued education it is difficult to imagine that I would have ever produced this dissertation. Each member of my family has helped me with countless difficult decisions, providing additional insight and reminding me when I have become too narrowminded and stubborn.

I am very grateful to my friends and co-workers for the support over the past six years. Specifically, I would like to thank Yitong Dong who has been my co-worker for nearly six years

now. Yitong is perhaps one of the most intelligent, patient, and thoughtful people I have met, he is always willing to discuss difficult topics and has proven time and again to help me solve the most difficult challenges I have experienced during graduate school. Ho Jin who I shared an office with for two years was a wonderful addition to my time here. Perhaps he did not share his opinions all the time, but when he did he would usually provide me with much needed help. Yerok Park who helped Yitong and I acclimate to our lab served as an ideal role model for a younger graduate student. I would also like to thank the rest of my lab mates who help me on a day to day basis. I must also thank greatly three of my closest friends who I met during my time at Texas A&M, Damien Lebrun-Grandie, Josey Wallace, and Jordi Morales, who provided the much needed respite from work and school, as well as my oldest friend Mike DeLaurentis who has always been and continues to be a good friend.

Lastly, I would like to thank my girlfriend Gabby Obkirchner, and our two cats Toffer and Muffins. No matter how difficult I am, you makes me smile and laugh every day. You continue to remind me of the importance of a balance between work and the rest of life, and I will always be grateful for you as a role model on how to be a decent person who can find common ground and enjoyment with almost everyone.

CONTRIBUTORS AND FUNDING SOURCES

Contributors

This work was supervised by a Dissertation committee consisting of Dr. Dong Hee Son, Dr. Timothy Hughbanks, and Dr. Simon North of the Department of Chemistry, and professor Choongho Yu of the Department of Mechanical Engineering.

All TMD nanodisc materials used in chapters III, IV, V, and VI were prepared by Dr. Cheon from the Yonsei University Chemistry Department in South Korea. DFT calculations in chapter V were conducted by Dr. Perla Balbuena from Texas A&M Department of Chemical Engineering. All other work conducted for this dissertation was completed by the student independently.

Funding Sources

Graduate study was supported by a fellowship from the Texas A&M University.

NOMENCLATURE

TMDC	Transition Metal Dichalcogenide
VDW	Van der Waals
PL	Photoluminescence
QD	Quantum Dot
a_b	Bohr Radius
Oam	Oleylamine

TABLE OF CONTENTS

	Page
ABSTRACT.....	ii
ACKNOWLEDGEMENTS.....	iv
CONTRIBUTORS AND FUNDING SOURCES	vi
NOMENCLATURE	vii
TABLE OF CONTENTS.....	viii
LIST OF FIGURES	xi
LIST OF TABLES.....	xvi
CHAPTER I INTRODUCTION AND LITERATURE REVIEW	1
1.1 Introduction.....	1
1.2 Introduction to TMDC	3
1.2.1 2D Materials Overview.....	3
1.2.2 Properties of Single and Few Layer TMDC	5
1.2.3 Introduction to Colloidal TMDC Nanoparticles and Quantum Dots.....	9
1.2.4 Optical Anisotropy in 2D Systems	11
1.2.5 Interparticle Electronic Coupling in Anisotropic Systems.	13
1.2.6 Electron Phonon Coupling in TMDC	14
1.2.7 Charge Carrier Relaxation Dynamics in TMDC Nanoparticles	18
1.3 Introduction to Perovskite Nanoparticles and Quantum Dots	21
1.3.1 Perovskite Nanomaterials Overview.....	21
1.3.2 Confinement Effects in Quantum Dots.....	23
1.3.3 Doped Semiconductor Nanomaterials	28
1.3.4 Carrier Relaxation in Quantum Dots	30
CHAPTER II EXPERIMENTAL DETAILS”	35
2.1 Transient Absorption Measurements	35
2.2 Synthesis of TMDC Nanoparticles	37
2.3 Synthesis of CsPbBr ₃ Quantum Dots	38
2.4 Synthesis of Mn-Doped CsPbCl ₃ Nanoparticles.....	39
CHAPTER III PHOTOINDUCED SEPARATION OF STRONGLY INTERACTING 2-D LAYERED TiS ₂ NANODISCS IN SOLUTION.....	40
3.1 Introduction.....	40

3.2 Results and Discussion	43
3.3 Conclusion	52
3.4 Experimental Details.....	53
3.4.1 Photoinduced Separation of Nanodiscs	53
CHAPTER IV ORIENTATIONAL CONTROL OF COLLOIDAL 2D LAYERED TRANSITION METAL DICHALCOGENIDE NANODISCS VIA UNUSUAL ELECTROKINETIC RESPONSE.....	54
4.1 Introduction.....	54
4.2 Results and Discussion	58
4.3 Conclusion	68
4.4 Experimental Details.....	69
4.4.1 Measurement of Electrooptic Response.....	69
4.4.2 Preparation of Orientation-Controlled TiS ₂ Nanodisc Films.....	69
CHAPTER V ANISOTROPIC ELECTRON-PHONON COUPLING IN COLLOIDAL LAYERED TiS ₂ NANODISCS OBSERVED VIA COHERENT ACOUSTIC PHONON.....	71
5.1 Introduction.....	71
5.2 Results and Discussion	74
5.3 Conclusion	85
5.4 Experimental details.....	86
5.4.1 DFT Calculations	86
CHAPTER VI CARRIER DYNAMICS AND INTERFACIAL ELECTRON TRANSFER DYNAMICS IN TiS ₂ AND TiS ₂ /TiO ₂ TYPE II HETEROSTRUCTURED NANODISCS.....	88
6.1 Introduction.....	88
6.2 Results and Discussion	90
6.3 Conclusion	101
CHAPTER VII EXCITON INDUCED TURNING ON OF DARK STATES IN CsPbBr ₃ QUANTUM DOTS.....	102
7.1 Introduction.....	102
7.2 Results and Discussion	104
7.3 Conclusion	114
CHAPTER VIII DYNAMICS OF EXCITON-TO- Mn ENERGY TRANSFER IN Mn- DOPED CsPbCl ₃ PEROVSKITE NANOCRYSTALS	115
8.1 Introduction.....	115
8.2 Results and Discussion	118
8.3 Conclusion	130
8.4 Experimental Detail	131

8.4.1 Nanoparticle Structural and Chemical Characterization.....	131
CHAPTER IX CONCLUSIONS	132
9.1 Anisotropy of the Optical and Electro-Optic Properties in TMDC Nanodiscs.....	132
9.5 Relaxation Dynamics in CsPbBr ₃ Quantum Dots and Mn-Doped CsPbCl ₃ Nanoparticles	135
REFERENCES	137

LIST OF FIGURES

	Page
Figure 1: Periodic table of elements with elements commonly found in the MX ₂ layered TMDC compounds (top). Typical structure of a layered TMDC MoS ₂ (bottom left) and the structure of a single layer top and side view (bottom right).....	4
Figure 2: A _{1g} and E ¹ _{2g} vibrational modes observed in the Raman spectra of MoS ₂ (left). Evolution of the electronic band structure of MoS ₂ from bulk to single layer with arrows representing the direct and indirect bandgap transitions (right).....	6
Figure 3: Dispersion relation for optical and acoustic phonon modes in a diatomic linear chain of atoms (top left). Carton describing the relative motion of atoms for the acoustic and optical phonon modes (top right). Observation of acoustic phonon modes in time dependent absorption data (bottom).....	16
Figure 4: Absorption spectra of 100nm diameter TiS ₂ nanodiscs (left) and bleach recovery dynamics (right) pumped at 800nm and probed at the maximum of the visible interband transition. Inset shows the short time dynamics.....	19
Figure 5: Size dependent absorption spectra from a series of strongly confined CdSe quantum dots. The lowest energy transitions are labeled (left). Size dependent energy levels of the lowest electron and holes stats as a function of particle size (right).....	26
Figure 6: Schematic energy level diagram of undoped and Mn doped CsPbCl ₃ nanoparticles. with the conduction and valence band, trap states, and Mn ligand field transitions. Note the energy scale is not correct as the absolute energy levels are unknown.....	29
Figure 7: Color contour plot of the pump probe data from CdSe quantum dots (left). Early time bleach signal from the same sample overlaid on the absorption spectra demonstrating the bleach features and corresponding absorption features (right).....	32
Figure 8: Separation of strongly interacting colloidal 2-D layered TiS ₂ nanodiscs via photoinduced weakening of interparticle cohesive energy that facilitates the solvation of each nanodisc	42
Figure 9: (a),(b) Extinction spectra and (c),(d) effective hydrodynamic diameter distributions of the colloidal TiS ₂ nanodiscs of two different sizes after ultrasonication or photoexcitation. (Blue) 1 hr ultrasonication, (Green) 10 hrs ultrasonication, (Red) 1 hr ultrasonication and 10 mins of pulsed photoexcitation at 800 nm. <i>d</i> =50 nm for (a), (c) and <i>d</i> =150 nm for (b), (d). (e) TEM image of <i>d</i> =150 nm TiS ₂ sample before and after 30 mins of photoexcitation. Scale bar is 200 nm (f) XRD patterns of <i>d</i> =150 nm TiS ₂ nanodiscs before and after 30 mins of photoexcitation. The vertical bars represent the standard XRD pattern of bulk TiS ₂ (ICSD #: 000-015-0853). * is noise	44

Figure 10: (a), (c) The time-variation of the absorption spectra of $d=150\text{nm}$ TiS_2 nanodiscs in chloroform under (a) *cw* and (c) pulsed laser irradiation condition. (b) Time-dependence of the peak position under *cw* (red) and pulsed (blue) laser irradiation. (d) Time-dependence of the peak intensity, $A(t)$, normalized to the initial intensity, $A(0)$, under *cw* (red) and pulsed (blue) laser irradiation 47

Figure 11: The effect of solvent polarity on laser-induced changes in the absorption spectra of $d=150\text{ nm}$ TiS_2 nanodiscs. Blue and red curves are before and after 5 min of pulsed laser irradiation respectively. The relative solvent polarity with respect to water is indicated in each panel..... 50

Figure 12: Reformation of the assembly of interacting $d=150\text{ nm}$ TiS_2 nanodiscs by changing the solvent polarity. Red: photoexcited sample in deoxygenated chloroform. Blue: 20 hrs after the resuspension of the photoexcited TiS_2 nanodiscs in cyclohexane. The spectra are normalized to the peak intensities..... 51

Figure 13: (a,d) Illustration of the random and oriented states of the colloidal nanoparticles under the square wave electric field for (a) TiS_2 nanodiscs and (d) CdS nanorods. [1],[2],[3] indicates low, step edge and high state of the electric field respectively. (b,e) Electrooptic response of (b) TiS_2 nanodiscs in cyclohexane and (e) CdS nanorods in tetradecane to the square wave electric field shown in (c) and (f) respectively. $\Delta A/A$ is the fractional change in the absorbance measured with linearly polarized light representing the presence of the orientational order 55

Figure 14: Electrode configurations for the electric field perpendicular (E_x) and parallel (E_z) to the light propagation direction (k). The glass sample capillary was sandwiched between the two electrodes. The polarization of light (θ_p) is defined with respect to the direction of E_x field 58

Figure 15: $\Delta A/A$ of TiS_2 nanodisc under (a) DC and (b,c) square wave E_x electric field. Polarization angle of light is $\theta_p=0^\circ$ (red) and $\theta_p=90^\circ$ (blue). (d,e,f) Time variation of the DC and square wave electric field corresponding to panels (a,b,c) respectively..... 59

Figure 16: (a) Polarization angle (θ_p) dependence of $\Delta A/A_{\text{peak}}$ under the square wave E_x (green) and E_z (black) electric field. $\Delta A/A_{\text{peak}}$ is the peak value of the fractional change in the absorbance from the square wave electric field. (b) The absorption spectra of TiS_2 nanodiscs under square wave E_x field with $\Delta E = 2.5\text{ kV/mm}$ for $\theta_p=0^\circ$ (red) and $\theta_p=90^\circ$ (blue) polarization. Black curve is the isotropic absorption spectrum taken without electric field. (c) ΔE dependence of $\Delta A/A_{\text{peak}}$ under square wave E_x field for $\theta_p=0^\circ$ (red) and $\theta_p=90^\circ$ (blue) polarization 60

Figure 17: (a) $\Delta A/A$ of TiS_2 nanodiscs measured with $\theta_p=0^\circ$ polarization under trapezoidal E_x fields with varying slopes at the edges, (b) Time-profile of the applied E_x electric field..... 63

Figure 18: (a) $\Delta A/A$ under E_z square wave electric field at 2 kHz showing the near-steady state orientational order. (b, c) AFM images of TiS_2 nanodiscs deposited on the microscope cover slip in the absence (b) and the presence (c) of the 2kHz square wave E_z field. The average diameter and thickness of the nanodiscs are 60 nm and 7 nm respectively	65
Figure 19: (a) Normalized absorption spectra of the surface-deposited samples, where TiS_2 nanodiscs were deposited on the microscope coverslip with (blue) and without (red) the applied AC square wave electric field. (b) Photograph of the microscope coverslip with the deposited TiS_2 nanodiscs. (c) Normalized comparison of the solution-phase absorption spectra for $\theta_p=0^\circ$ (red) and $\theta_p=90^\circ$ (blue) under E_x field originally shown in Figure 16b	66
Figure 20: (a-f) TEM images and (g) optical absorption spectra of colloidal TiS_2 nanodiscs of different sizes	73
Figure 21: Color contour plot of the transient absorption spectra of colloidal TiS_2 nanodiscs	75
Figure 22: (a-c) Transient absorption data at two different probe wavelengths on the opposite sides of the absorption peak near 600 nm. The average diameter and thickness of the nanodiscs and the probe wavelengths are indicated in each panel. (d-f) The oscillatory component of the transient absorption signal extracted from the fitting of the data	75
Figure 23: Electronic band structure along high-symmetry directions (left) and DOS (right) of TiS_2 at optimized lattice parameter (strain-free system). Dashed blue line stands for the Fermi-level, which is set to be 0 eV. Black circles indicate points in the reciprocal lattice at which the indirect overlap is shown. The vertical dashed line indicates a point between K- and Γ -point (Σ -point), where the VBM is located for expansions above 0.1 Å.....	81
Figure 24: Imaginary part of refractive index (k) under varying degrees of lattice strain. k_\perp and k_\parallel are shown as solid and dashed lines respectively. (a,b) In-plane compressive and tensile strain respectively. Arrows indicate the direction of the peak shift of with increasing strain. (c,d) Out-of-plane compressive and tensile strain respectively. Δa and Δc are relative to the strain-free lattice parameters of $a=3.410$ Å and $c=6.064$ Å respectively	83
Figure 25: Dependence of the peak position of P3 in k_\perp on in-plane (blue, Δa) and out-of-plane (red, Δc) lattice strain. Δa and Δc are relative to the strain-free lattice parameters of $a = 3.410$ Å and $c = 6.064$ Å respectively	84
Figure 26: (a) Top and (b) side view of a portion of the TiS_2 structure. Gray and yellow spheres represent Ti and S atoms, respectively. (b,c) Arrows show the direction of the out-of-plane and in-plane strain	87

Figure 27: Side and top view TEM images of TiS ₂ nanodiscs with $\langle d \rangle = 60\text{nm}$ (a,c), and $\langle d \rangle = 150\text{nm}$ (b,d). Absorption spectra of $\langle d \rangle = 60\text{nm}$ and $\langle d \rangle = 150\text{nm}$ TiS ₂ nanodiscs with the relevant transitions marked as dashed vertical lines.....	90
Figure 28: Short time pump probe spectra and dynamics for $\langle d \rangle = 150$ (a,c), and $\langle d \rangle = 50\text{nm}$ (b,d) TiS ₂ nanodiscs. The black dashed line represents the long time dynamic spectra taken at $\sim 2\text{ns}$	91
Figure 29: Comparison of bleach dynamics of 60nm TiS ₂ naondiscs under 800nm (a), and 400nm (b) excitation	93
Figure 30 (a,b) TEM images of (a) TiS ₂ nanodiscs and (b) TiS ₂ /TiO ₂ heterostructured nanodiscs produced from partial chemical oxidation of TiS ₂ nanodiscs. (c) X-ray diffraction patterns of TiS ₂ (blue) and TiS ₂ /TiO ₂ (red) nanodiscs. (d) Absorption spectra of TiS ₂ (blue) and TiS ₂ /TiO ₂ (red) nanodiscs	94
Figure 31: (a,b) Transient absorption spectra for 60nm TiS ₂ nanodiscs (a), and TiS ₂ /TiO ₂ heterostructure nanodiscs (b) excited at 400 nm. (c) Transient absorption probed at the peak of bleach (580 nm) for TiS ₂ nanodiscs (blue) and TiS ₂ /TiO ₂ heterostructure nanodiscs (red) Pump probe relaxation dynamics probed for 60nm (blue) and TiS ₂ /TiO ₂ heterostructure nanodiscs (red) excited at 400 nm and probed at the wavelength of maximum bleach ($\sim 580\text{nm}$).....	96
Figure 32: (a,b) Transient absorption spectra for 60nm TiS ₂ nanodiscs (a), and TiS ₂ /TiO ₂ heterostructure nanodiscs (b) excited at 800 nm. (c) Transient absorption probed at the peak of bleach (580 nm) for TiS ₂ nanodiscs (blue) and TiS ₂ /TiO ₂ heterostructure nanodiscs (red)	98
Figure 33: (a) Absorption spectra from CsPbBr ₃ quantum dots with decreasing size. (b-d) TEM images from samples I, III, and V, scale bars are 20nm.....	104
Figure 34: (a-e) Time resolved transient absorption spectra from samples (I, III, IV, V, VI) after excitation at 3.14 eV. (f-j) Slices at 200 fs and 10 ps (blue and red curves) taken from the corresponding spectra a-e. (k-o) decay dynamics from the bleach (red line) and IA signal (black circles) from the corresponding spectra a-e	106
Figure 35: (a) Shift of E_{IA} and E_1 (open and closed circle) with particle size. (a) Shift of $E_{IA} - E_1$, $E_2 - E_1$, (open and closed circles), and the ratio $\frac{E_2 - E_{IA}}{E_2 - E_1}$ (stars) as a function of the first exciton energy. The first exciton energy is taken as a placeholder for the size of the particle.....	109
Figure 36: First five picoseconds showing the rise time of the bleach and both induced absorption signals from samples I, IV, and VI.....	112
Figure 37: (a,b) TEM images of undoped (a) and Mn-doped (b) CsPbCl ₃ nanocrystals. (c,d) Absorption and PL spectra of undoped (blue) and Mn-doped (red) CsPbCl ₃	

nanocrystals respectively. Small peak at ~370 nm in the PL spectra is from the excitation light. (e) Illustration of the crystal structure of Mn-doped CsPbCl₃ and the photographs of PL from Mn-doped and undoped CsPbCl₃ nanocrystal solutions. (f) XRD patterns from undoped (blue) and Mn-doped (red) CsPbCl₃ nanocrystals... 120

Figure 38: (a) The competing dynamic processes in undoped and Mn-doped perovskite nanocrystals. (b) Transient absorption data of undoped (blue) and Mn-doped (red) CsPbCl₃ nanocrystals with 395 nm pump and 400 nm probe. (c) Transient absorption data of undoped (blue) and Mn-doped (red) CdS/ZnS core/shell quantum dots. Data from Reference 14 are replotted. (d) The difference between the two transient absorption data in (b) taken after normalizing to the ns recovery component. See the text 121

Figure 39: Comparison of (a) absorption, (b) PL emission and (c) transient absorption probed at the peak of exciton absorption between freshly synthesized (blue) and self-anion exchanged (red) CsPbCl₃ nanocrystals..... 126

LIST OF TABLES

	Page
Table 1: Experimental (τ_{exp}) and calculated periods for intralayer (τ_{intra}) and interlayer (τ_{inter}) coherent acoustic phonon of TiS ₂ nanodiscs of different average diameter $\langle d \rangle$ and thickness $\langle t \rangle$	77
Table 2: Multi-exponential fit parameters of transient absorption data probed at the peak of the bleach. The time constant for the slow recovery component (τ_3) was fixed at 5ns	96
Table 3: Energy of the first two exciton absorption features (E_1 and E_2) extracted from fitting of absorption spectra in figure 1, as well as the induced absorption energy (E_{IA}) extracted from the 10ps transient absorption spectra figure 2 (f-j red curves).....	105
Table 4: Fitting parameters of normalized transient absorption data to $-\sum a_i \cdot \exp(t/\tau_i)$ for E_{IA} and E_1 rise and decay times	110
Table 5: Fitting parameters of normalized transient absorption data to $-\sum a_i \cdot \exp(t/\tau_i)$	123
Table 6: Comparison of the structural parameters and the energy transfer time (τ_{ET}) of Mn doped CsPbCl ₃ nanocrystal and Mn-doped CdS/ZnS core/shell quantum dots. The data for Mn-doped CdS/ZnS quantum dot were extracted from Reference 14.....	127

CHAPTER I

INTRODUCTION AND LITERATURE REVIEW

1.1 Introduction

Semiconductors have been at the forefront of the 20th-21st century technological revolution, making up the foundation for all digital technology, solar cell technology, and in recent years advanced telecommunication technologies. The solar cell has been a staple to track the evolution of semiconductor technology. There are typically three generations of solar cells discussed, first generation single junction silicon wafer cells; second generation single junction cells made from new materials such as CdTe and CIGS; third generation organic photovoltaics, quantum dot, multi-junction cells, generally any cell based on novel light harvesting materials. Similar trends can be observed in other semiconductor fields such as the drive for atomically thin transistors, and telecommunications systems which are currently transferring to optical based communications. The demand for technological advancement requires the development of the semiconductor and photonic industries at a rapid pace.

A particular area of interest for the latest round of technology are the confined semiconductor systems including atomically thin films, nano wires, and quantum dots. While confined systems were studied initially to understand the effects of quantum confinement, there now exists an extensive body of work regarding their practical applications such as atomically thin photo-detectors and all quantum dot electronic devices. The development of this technology requires the not only the preparation of novel materials, but also the rapid, careful, and thorough characterization of material properties.

This project will focus on the optical properties of novel semiconductor nanoparticles and quantum dots. The first half of the dissertation will discuss the effects of confinement in layered

TMDC materials with a focus on lateral confinement effects and the effects of anisotropy. Large area single layer TMDCs are well characterized and demonstrate many interesting properties such as the emission of circularly polarized light, however only recently have TMDC nanoparticle been available for study and there exists no detailed studies of their electronic and optical properties. The second half of this dissertation will discuss the confinement effect in metal halide perovskite quantum dots and Mn²⁺-doped perovskite nanoparticles. Metal halide perovskite quantum dots were only recently made available and have demonstrate remarkable optical properties such as near unity quantum yield and low threshold lasing. Unfortunately, in the rush discuss the properties such as the carrier dynamics, characterization has been rather sloppy. In our lab we have the most high-quality perovskite quantum dots available, and are in the unique opportunity to more carefully characterize their properties.

1.2 Introduction to TMDC

1.2.1 2D Materials Overview

The preparation of graphene, the single layer derivative of graphite, was a major scientific development bringing the study of 2D confined materials from strictly theoretical to experimental. While initially considered thermodynamically unstable, high quality graphene layers can be prepared through exfoliation with an adhesive layer, transfer to a substrate, followed by simple cleaning to remove unwanted organics. Utilizing these exfoliation methods, large area/high quality graphene sheets can be isolated (up to 100's of μm) and studied with a variety of optical and electrical characterization techniques. The uniqueness of graphene is highlighted by its mechanical and electronic properties, including high carrier mobility, strong visible light absorption ($\sim 2.3\%$ for a single layer), and large Young's Modulus. Furthermore charge carriers at the fermi level demonstrate extremely low effective-mass ($m_e \sim 0.06m_0$, $m_h \sim 0.03m_0$), an unusual property leading to a variety of unique physics. While a considerable amount of research on graphene continues, the 0 eV bandgap is undesirable for optoelectronic applications, prompting efforts to both modify the electronic structure of graphene find novel 2D confined semiconductors.

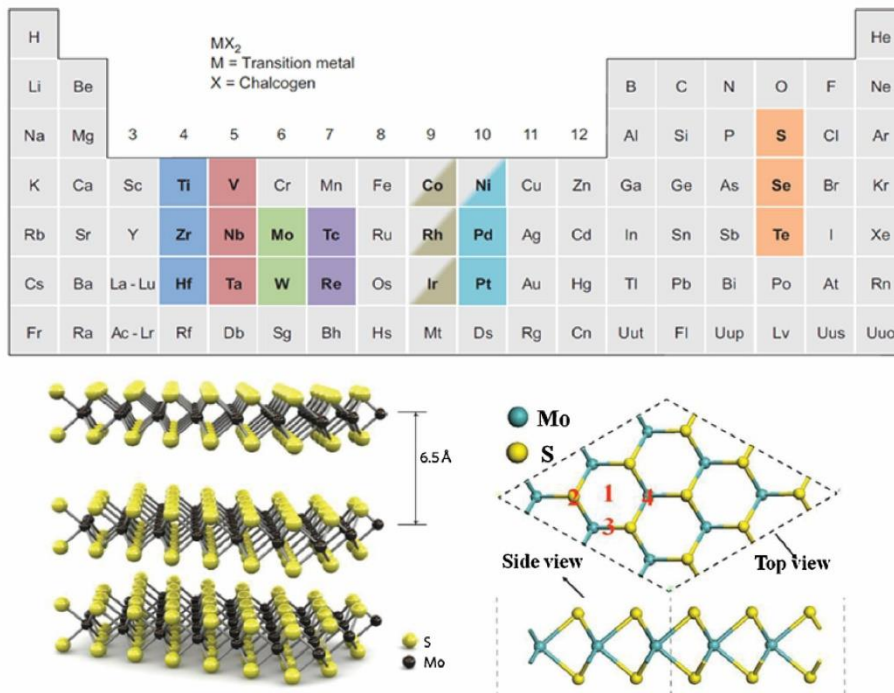


Figure 1: Periodic table of elements with elements commonly found in the MX₂ layered TMDC compounds (top). Typical structure of a layered TMDC MoS₂ (bottom left) and the structure of a single layer top and side view (bottom right). (Reprinted in part with permission from Zuoli He, Wenxiu Que. Molybdenum disulfide nanomaterials: Structures, properties, synthesis, and recent progress on hydrogen evolution reaction. *Appl. Mater. Today*, **2016**, 3, 23-36. Copyright 2016 by Elsevier.)¹

Efforts to find 2D materials with optical bandgaps have produced a library of materials including metals, semi-metals, semiconductors, and insulators, all with well-defined synthetic procedures and extensively characterized properties. From this library, the most notable group of materials is likely the TMDC family. TMDCs consist of tri-atomic (MX₂) layers where a metal atom (M) is sandwiched between two chalcogen atoms (X), and the sandwiches are stacked and held together via weak VDW forces. A typical crystal structure can be seen in the bottom of figure 1. The identity of both the cation and anion, the number of stacked layers, and the stacking order can all effect the vibrational and electronic properties, making TMDCs both interesting and

suitable for a number of applications. Figure 1 shows the typical structure of a TMDC material as well as a periodic table with elements highlighted indicating the common metal and chalcogen combinations in TMDC materials. Note the coordinate axis on the crystal structure where it is conventional to represent the z-axis in the direction perpendicular to the MX_2 plane.

1.2.2 Properties of Single and Few Layer TMDC

To date there are numerous synthetic schemes for TMDC growth. The general idea follows either top down methods where single layers are prepared from the bulk, or bottom up methods where samples are directly grown on substrates. The most common procedure to produce TMDCs remains mechanical cleavage from a bulk crystal, similar to the method described above for the preparation of graphene layers. While this method is useful for studying the material properties, it is not applicable to the large-scale single layer preparation as it is difficult to prepare truly homogeneous single layers. For the preparation of large scale single layers with more dimensional control, top down solution based exfoliation methods have been studied, notably ion intercalation methods. In these methods, ions such as Li^+ are intercalated between the TMDC layers, weakening the VDW forces, and the layers are then cleaved from one another via sonication. Ion intercalation have proven to produce large quantities of single layers, however, these methods are tedious, sensitive, and do not always produce high quality samples.

The bottom up approach has been more successful for the synthesis of large area high quality TMDC monolayers, and recently more complicated heterostructures. Particular interest has been given to chemical vapor deposition methods where reactive precursors are deposited onto a substrate at high temperatures and annealed into crystalline films.² With these methods high quality single layer films with sized up to a few centimeters have been reported.³ Chemical vapor deposition is now advanced to the point that a number of unique heterostructures can be formed

with high levels of control, including both inter-layer and intra-layer heterostructures, opening the door to a whole new area of research.⁴⁻⁵

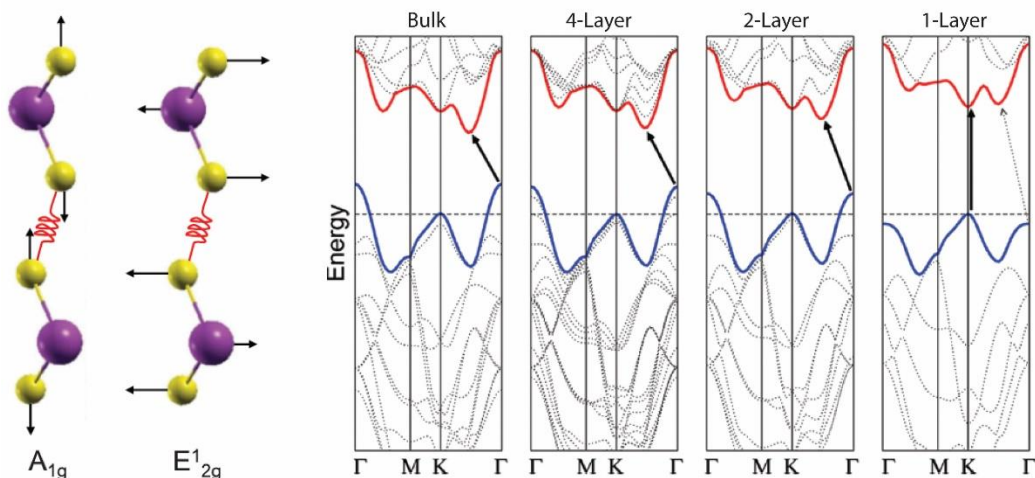


Figure 2: A_{1g} and E_{2g}^1 vibrational modes observed in the Raman spectra of MoS_2 (left). Evolution of the electronic band structure of MoS_2 from bulk to single layer with arrows representing the direct and indirect bandgap transitions (right). (Reprinted in part with permission from A. Molina-Sanchez and L Wirtz. Phonons in single-layer and few-layer MoS_2 and WS_2 . *Phys. Rev. B*, **2011**, 84, 155413-155421. Copyright 2011 by American Physical Society. Reprinted in part with permission from Zuoli He, Wenxiu Que. Molybdenum disulfide nanomaterials: Structures, properties, synthesis, and recent progress on hydrogen evolution reaction. *Appl. Mater. Today*, **2016**, 3, 23-36. Copyright 2016 by Elsevier.)^{1, 6}

The strength of electronic and vibrational coupling between layers in the bulk and how this coupling evolves as the material is brought to a single layer. In the case of TMDC materials, while the VDW forces that adhere the layers are weak, the electronic and vibrational coupling between the layers can be quite strong. The interlayer coupling of both electronic and vibrational degrees of freedom is observed in a number of studies on TMDC materials where the evolution of electronic and vibrational properties are studied as a function layer number. The modulation of the

electronic bandgap from indirect to direct as well as the shifting of phonon frequencies as the number of layer is decreased has been observed in many TMDC materials.

The layer dependent evolution of the vibrational structure in MoS₂ is both interesting as a probe of the interlayer vibrational coupling, and practical as a method to find and characterize single layers from multilayers. It is important to note that while MoS₂ is commonly used as the material to study TMDC single layers, most findings can typically be generalized to all TMDCs. In TMDC materials, two subsets of vibrations are commonly discussed, in-plane modes where the atoms move perpendicular to the z-axis, and the out-of-plane modes where the atoms move parallel to the z axis. Figure 2(left) shows the motion of the atoms for the A_{1g} and the E¹_{2g} vibrational modes commonly studied in the Raman spectra of MoS₂. Were the individual layers in the bulk completely isolated, the vibrational frequencies would be independent of the number of layers, and if one assumes that adjacent layers can be treated as a coupled harmonic oscillator, both modes would shift to higher frequencies with additional layers. From the Raman experiments, the A_{1g} mode shifts towards higher energy in the bulk, and the E¹_{2g} mode shifts towards lower energy, suggesting that there is coupling between the layers, however it is not described by the simple coupled harmonic oscillator.⁷⁻⁸

To explain the unusual shifting of vibrational modes observed in these experiments both short-range interactions between layers (additional spring constants) as well as the long-range interactions (coulomb interactions) must be considered. The shift of the A_{1g} mode, corresponding to the symmetric out-of-plane stretching of S atoms, to higher energy is intuitively rationalized by considering the interaction between S atoms on adjacent layers. The addition of a layers is equivalent to adding extra second spring constants coupling the layers and stiffening modes involving those interactions.⁶⁻⁷ The E¹_{2g} mode involves the asymmetric stretching of both Mo and

S atoms, and while it may be intuitive to apply the similar reasoning above, it does not describe the observed behavior. The shift of E_{2g}^1 to lower energy involves the increase in columbic screening as the number of layers are increased. In turn, this increases the Mo-Mo self-interaction energy causing the vibrational mode to shift towards lower frequencies.⁶ Similar shifts of A_{1g} and E_{2g}^1 Raman modes have been observed in other TMDC materials including MoSe_2 , WS_2 , WSe_2 , making this a generic tool for the identification of TMDC monolayers.⁸⁻¹¹ While these studies highlight the complexity of the coupling between the individual layers, more interest has been given to the electronic properties of the single layer TMDC materials.

The modulation of the bandgap as the number of layers is reduced is a striking feature of the TMDC family. Semiconducting TMDCs experience an indirect to direct bandgap crossover as the number of layers is reduced.¹²⁻¹³ Figure 2(right) shows the evolution of the electronic structure of MoS_2 from bulk to a single layer. The points of critical interest are at Γ and K, the origins of the indirect and direct transitions. The most striking feature in the electronic structure is the decrease in energy of the valence band maximum at the Γ point with decreasing number of layers, which in the monolayer drops below the conduction band maximum at K leading to the direct bandgap transition. This transition is a direct result of the modulated coupling between the individual layers in the TMDC, which is dictated by both the charge redistribution in each layer and the distance between adjacent layers. Experimental evidence suggesting that the interlayer distance expands by $\sim 5\%$ at the surface of a bulk crystal, and the in-plane Mo-Mo distance contracted $\sim 4\%$ in a single layer.¹³⁻¹⁵ Recent theoretical studies on single and multilayer MoS_2 corroborate the expansion of the interlayer distance, and contraction of the in-plane Mo-Mo distance in bilayer and monolayer samples compared to bulk. Since density of states at the Γ point is dominated by Mo d_{z^2} and p_z orbitals while the K point is dominated by MO $d_{x^2-y^2}/d_{xy}$, and S p_x/p_y , the modulation of the

electronic structure is more sensitive to the interlayer spacing at Γ where the atomic orbitals are protruding in the interlayer gap.¹⁶⁻¹⁷

The most well studied property of monolayer TMDC is the ability to emit circularly polarized light. The lattice symmetry of the TMDC consists of six energy degenerate K points in reciprocal space which form two distinct sets of momentum K^+ and K^- . In the monolayer where the K point becomes the optical bandgap, the K^+ and K^- points can be selectively excited by altering the helicity of the excitation source, and in turn emission from these points is coupled with the polarization of the excitation.¹⁸ While this “valley” selective excitation has become a staple of TMDC research, however it will not be discussed further here.

1.2.3 Introduction to Colloidal TMDC Nanoparticles and Quantum Dots

The anisotropy inherent in TMDC materials has been studied for several decades. In the 1970s and 1980s, a number of papers discussed TMDCs as intercalation compounds for lithium ion batteries, as superconductors, and as photovoltaic materials.¹⁹⁻²¹ These studies focused on utilizing the anisotropy of the material properties, for example taking advantage of the ability to intercalate ions and molecules between the loosely bound layers, or boosting extraction efficiency from a photovoltaic by utilizing the large in-plane mobility of the TMDC. More recently, there have been reports on the anisotropy of thermal properties including thermoelectric efficiency and thermal conductivity, however many of the more unique anisotropic properties remain unstudied, highlighting the need for further investigation.²²⁻²³

The effects of quantum confinement are now well established in many semiconductor systems, mainly, the reduction of dimensionality from bulk to 2D sheets, 1D rods and wires, and 0D dots manifest extraordinarily diverse size tunable properties. The most well known being the tuning of PL energies with particle size, the increase in exciton binding energies in confined

structures, and the confinement induced anisotropic optical properties. In 2D materials such as TMDCs, the effects of lateral confinement must be treated separately from effects of layer reduction, and since CVD and exfoliation are not capable of forming laterally confined structures, novel synthetic procedures are required. Only recently were laterally confined TMDC materials available. To date a number of laterally confined TMDC can be synthesized including M (Ti, W, Mo) and X (S, Se, Te) as well as others.²⁴⁻²⁵

There are two main synthetic methods for generating colloidal TMDC nanoparticles and QDs, hydrothermal synthesis from metal and chalcogen precursors, and generation of QDs from the decomposition of bulk. The decomposition from bulk is now a common method to synthesize TMDC QDs, however these particles have proven difficult to clean and characterize and they will not be discussed further.²⁵ The hydrothermal synthesis is more well controlled, and a variety of TMDC materials can be synthesized. This method gives control over the lateral size of the nanoparticle, however reaching the quantum confinement regime has been difficult for a number of materials. Nevertheless, particles synthesized in this method are highly soluble, clean, and their structures are well characterized.^{24,26} Borrowing common intercalation methods, it is also possible to exfoliate these nanoparticles to form single layer TMDC nanoparticles with controlled lateral dimension.²⁷⁻²⁸ Similar to the bulk films, in the monolayer nanoparticles appear to be a direct bandgap semiconductors demonstrating excitonic PL. Recently, PL studies of laterally confined single layer WSe₂ showed PL (which could be tuned up to 20% quantum yield) that correlated well with excitonic features in the absorption spectrum, and blue-shifted with decreasing particle diameter. More importantly, the laterally confined structures appeared to maintain the in-plane 2D dipole manifested as polarized PL from ensemble of particles on a film, a feature not observed in other QD systems.²⁸

The study of confinement effects and anisotropy in TMDC nanoparticles will be discussed in detail in chapters III, IV, V, and VI. Attention will be paid to the anisotropy and confinement of electron-phonon coupling, anisotropy of the polarizability and absorption, and the dynamics of charge transfer in 2D systems. In the majority of studies TiS₂ nanodiscs will be used, however, where applicable the generalization to all TMDCs will be made. TiS₂ was chosen for these studies as it was the nanoparticle with the most well controlled size. Thicknesses ranging from 7-10 nm and diameters ranging from 30-150nm were available, making it possible to study the dependence of properties on both the thickness and diameter.

1.2.4 Optical Anisotropy in 2D Systems

The suspension of particles in colloidal solution offers the opportunity to study unique dimensionally dependent properties not available to substrate bound samples. Spectroscopic studies to date have focused on TMDC films where the investigation of out of plane properties have been difficult. Since colloidal solutions of TMDC are orientationally averaged in solution, spectroscopic signals probe a combination of both in-plane and out-of-plane properties. Numerous techniques for the manipulation and assembly of nanoparticles via external stimuli are well developed, including various techniques to align nanoparticles in solution as well as for the preparation of aligned particles on substrate.²⁹⁻³¹ Typically these methods involve the interaction of static electric or magnetic dipoles with an external electric or magnetic field, and can be used to measure a number of properties including the magnitude of static or induced electric/magnetic dipole moments, rotational diffusion constants, and optical anisotropies.^{30, 32-33}

The observation of electric field alignment induced birefringence in CdSe nanorods is an instructive study to understand these experiments. CdSe with hexagonal symmetry possess a dipole moment. When grown in an anisotropic structure like a rod, the size of the dipole scales with length

of the rod. When this dipole interacts with a electric field, alignment of the rod with the field becomes favorable and a suspension of particles will show preferential alignment to the field. In these anisotropic systems where there is also anisotropy in the optical absorption, the transmission of polarized light is modulation with the orientation of the particles.³²

It is also possible to orient materials via anisotropic polarizability, for example gold nanorods. When the total induced dipole moment in the gold nanorod is anisotropic, a dispersion can align in an electric field. In such a case one can selectively observe the longitudinal or transverse plasmon modes in a polarized transmission experiment depending on the direction of the electric field.³⁴ In chapter IV will discuss the observation of electric field induced birefringence in TMDC nanoparticles.

Orientation control of TMDC nanodiscs would be a useful tool to study anisotropic optical properties, however, the inversion symmetric octahedral coordination of atoms in most TMDC means that no permanent dipole moment is expected and the alignment of TMDC nanoparticles in an electric field is unlikely. The observation of electric field induced dichroism is completely absent in all samples even in DC fields up to 1.5kV/mm. Interestingly, in a number of TMDC nanoparticles a transient orientational order can be induced in AC fields only during the period of changing electric field, for example the rising or falling step edge of a square wave. While this effect will be discussed in more detail later, it is related to the anisotropy of nanodisc polarizability.³⁵ Upon application of the electric field, a strong in-plane polarization is formed, however over a short period of time (~ms) the out-of-plane polarization grows the and the total polarization anisotropy is not large enough to maintain orientation in the field. Regardless, utilizing this technique we observed the relative contributions to visible interband transition from in-plane and out-of-plane transitions. Furthermore, utilizing high frequency AC fields we achieved

orientational order on a substrate with the c-axis parallel to the substrate allowing us to study in more detail the optical anisotropies.

1.2.5 Interparticle Electronic Coupling in Anisotropic Systems.

The optical excitation of nanoparticles leads to the formation of electrons and holes, whose wavefunction can exceed the dimensions of the particle. In such a case, the wavefunction tends to spill out of the particle, sensing the local environment, this leads solvatochromism in quantum dots. In the case of ordered assemblies or aggregates, where the wavefunction of neighboring particles can interact, the interparticle electronic coupling can have a profound impact on the electronic and optical properties of the material.

Interparticle electronic coupling has been observed in both metal and semiconductor nanostructures, and used as a tool to modulate the transport properties in quantum dot films.³⁶ One of the most common studies on the interparticle coupling is the coupling of two plasmonic nanostructures. In metal nanoparticles, the near-field interactions between two surface plasmon leads to the red-shifted plasmon scattering peaks. Furthermore, the effects of enhanced electric fields in these coupled nanoparticles is observed as hot spots, where up to a million-fold enhancement of electric fields can be achieved.³⁶⁻³⁷

In the case of semiconductor and non-plasmonic metal nanoparticles and quantum dots, the coupling of nanoparticles and the formation of nanoparticle super lattice leads to a variety of new optical and electronic properties.³⁸⁻³⁹ As particle are brought close enough to experience electronic coupling, a red shift of the absorption and PL spectra is observed effectively a decrease in the spatial confinement, as well as changes in transport properties from inter-particle charge hopping to band-like transport. The relative size of these effects are governed by the interparticle separation distance and can be tuned by the choice of appropriately small ligands. In films of very close

packed (necking) particles, the resistivity of the film can drop low enough to be useful in device manufacturing.⁴⁰ In fact, a number of recent studies have focused on all nano particle electronic devices such as transistors, which take advantage of the easy low cost nanoparticle synthesis in devices with viable performance.⁴¹

The magnitude of the interparticle electronic coupling can also be tuned by adjusting the relative interparticle interaction area. As such spherical dots demonstrate inherently weak interparticle coupling due to the point like nature of the interfacial interaction. For systems with much large interfacial interactions the effects can be greatly amplified, for example the effect of coupling in the CdSe nanorod is significantly stronger than in quantum dots. In chapter III, we will discuss the interparticle electronic coupling in TMDC nanodiscs. A simple comparison of the structure of the TMDC nanodisc suggests that the potential for interparticle electronic coupling is much larger than in 0D or 1D structures due to the large flat nanodisc basal plains. Monitoring the absorption spectra we observe shifts of over 500nm in vertically stacked nanodisc assemblies compared to the isolated discs, compared to the 10-15nm absorption shift in close packed CdSe QD films.

1.2.6 Electron Phonon Coupling in TMDC

Similar to bond vibrations in molecules, the ions in crystals vibrate about their nuclear coordinate, these vibrations are called phonons. Phonons are significant to many processes in solid state chemistry/physics, for example the PL linewidth in semiconductor QD typically experiences significant broadening due to contribution from phonons. Other important material properties such as heat capacity, thermal expansion, and charge carrier mobility are also affected by the density and dispersion of phonon modes of the crystalline lattice. Before discussing this topics in TMDCs it is instructive to consider a simple model for describing phonon modes.

Considering a one-dimensional chain of diatomic atoms, in the harmonic oscillator model, the force acting on an atom is, $F = -\frac{\partial}{\partial x}V(x) = -cs$ where $V(x) \approx V(x_0) + \frac{1}{2}\left[\frac{\partial^2}{\partial x^2}V(x)\right]_{x_0} s^2$.

Solving the equations of motion for the diatomic system one arrives at the dispersion relation,

$$\omega_{\pm}^2 = \frac{c}{M^*} \pm c \sqrt{M^{*2} - \frac{4}{M_1 M_2} \sin^2\left(\frac{ka}{2}\right)}, \text{ where } M^* = \frac{1}{M_1} + \frac{1}{M_2} \text{ and } k \text{ is the wave-vector of the}$$

phonon. This dispersion relation is important because it highlights two solutions, ω_{+}^2 and ω_{-}^2 , which correspond to physically different subsets of phonons in that $\omega_{-}^2=0$ at $k=0$ and $\omega_{+}^2 \neq 0$ at all k . Figure 3 (left, right) shows the dispersion relation for the diatomic linear, the upper branch corresponds to the ω_{+}^2 solution commonly referred to as optical phonons, and the lower branch corresponds to the ω_{-}^2 solution commonly referred to as acoustic phonons, as well as a cartoon describing the nuclear motion. A more intuitive description, acoustic phonons correspond to the motion of different atoms in the same direction, and optical phonons to the movement of different atoms in opposite directions.

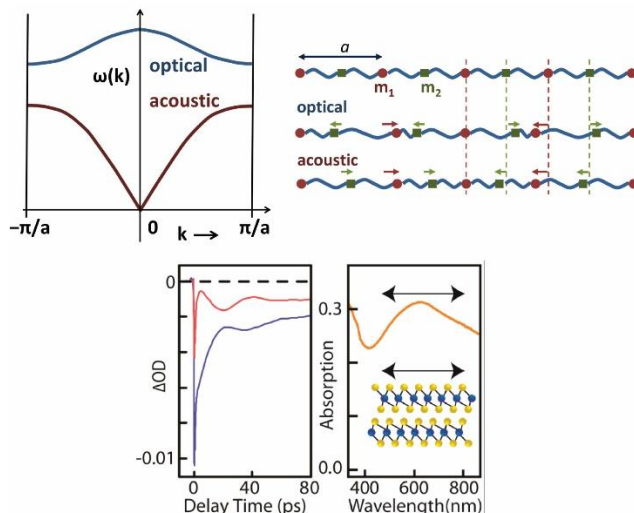


Figure 3: Dispersion relation for optical and acoustic phonon modes in a diatomic linear chain of atoms (top left). Carton describing the relative motion of atoms for the acoustic and optical phonon modes (top right). Observation of acoustic phonon modes in time dependent absorption data (bottom). (Reprinted in part with permission from Daniel Rossi, Luis E. Camacho-Forero, Guadalupe Ramos-Sanchez, Jae Hyo Han, Jinwoo Cheon, Perla Balbuena and Dong Hee Son. Anisotropic Electron-Phonon Coupling in Colloidal Layered TiS_2 Nanodiscs Observed Via Coherent Acoustic Phonon. *J. Phys. Chem. C*, **2015**, 119(13), 7436-7442. Copyright 2015 by the American Chemical Society.)⁴²

The role of phonons is critical in the dynamics of many charge carrier relaxation and charge transfer processes. Following photoexcitation in semiconductors, both band edge and hot charge carriers, as well as bound excitons, interact with the phonon modes. Phonons mediate the relaxation processes by accepting energy equal to the energy of the phonon, typically 10-several hundred cm^{-1} . The release of energy to phonons dictates the relaxation dynamics in QD systems, for example in PbS the mismatch of the confined electronic energy states with phonon states causes a “phonon bottleneck”, a decrease in the carrier cooling rate as there are no available phonons to accept the excesses carrier energy.⁴³⁻⁴⁴ Phonons also play a role in band transport, for example loss of circularly polarized emission in TMDC monolayers is related to the phonon mediated intervalley scattering processes.⁴⁵

The anisotropic crystal structure of TMDCs results in anisotropy of the phonon modes into inter-layer and intra-layer modes. An interesting question regarding the relaxation dynamics in TMDC is how optical excitations couple to the anisotropic phonon modes. In TMDCs the absorption is expected to have strong in-plane polarization, meaning the strongest excitation is an in-plane dipole excitation. Since the utility of TMDC relies on taking advantage of the anisotropic properties, understanding how electronic excitation couples to anisotropy of the phonon modes provides critical information for tailoring these systems. For example, the mobility is suggested to be limited by the scattering of carriers with intra-layer phonons, information which is helpful for building devices such as solar cells or transistors. However since there is little evidence to support this claim more experimental understanding is critical. Raman spectroscopy is typically used to study the charge carrier-phonon coupling, it has limitations in that not all phonon modes are Raman active, and low energy acoustic phonons are not easily resolved. A full description of charge carrier-phonon coupling requires expanded experimental techniques.

To extract information on the anisotropy of carrier-phonon coupling in TMDCs, we will employ time resolved femtosecond absorption spectroscopy on TiS_2 nanodiscs with variable size and thickness. The details of this experiment will be discussed in chapter V, in brief, following excitation with a short pulse of light phonons can be generated via a number of methods. The vibrational period of the phonon can be observed in the shifting of the excited state absorption spectrum, corresponding the excited state potential shifting along the phonon coordinate. This method is powerful in that it can resolve both acoustic and optical modes, is insensitive to optical selection rules, and can observe sub cm^{-1} phonon modes. Figure 3 (bottom) shows a schematic and an example of data used to extract the phonon frequencies. In chapter V, the application of this method to study anisotropic electron-phonon coupling in TiS_2 nanodiscs with variable radius and

thickness will be discussed. The relationship between the structural anisotropy and the effects of lateral confinement on the electron phonon coupling will be extrapolated.

1.2.7 Charge Carrier Relaxation Dynamics in TMDC Nanoparticles

The application of semiconductor nanoparticles for photo-catalytic systems has been studied since colloidal samples were made available. Colloidal nanoparticles offer a remarkably tunable platform where the electron and hole potential can be varied over a wide range with appropriate tuning of the particle size, shape, and composition.⁴⁶ Furthermore, the preparation of heterostructures where an electron and hole can be spatially separated in the structure can extend charge carrier lifetimes enhancing catalytic efficiencies. The heterostructure system is particularly interesting in that the absorbing material and the catalytic material are separated, meaning they can be independently tuned to suit specific applications. One commonly studied structure is the semiconductor nanoparticle/TiO₂ heterostructure, where a semiconductor nano-particle absorbs light generating electron-hole pairs, and electrons are injected into TiO₂ where they can be used as long lived carriers for photo-catalysis. This scheme has been employed with numerous QD systems including CdS, CdSe, and PbS.⁴⁷

Tuning semiconductor systems for photocatalytic use requires knowledge of the nature and timescales of carrier relaxation. In semiconductors, following photo-excitation above the band gap electrons and holes relax via many competing processes. The typical examples include relaxation via emission of phonons, radiative electron-hole recombination, carrier localization at a variety of charge trapping sites, and charge/energy transfer processes. When multiple electron/holes are generated, multicarrier processes such as auger recombination and exciton-exciton annihilation can take place. In a given system the complete relaxation is typically dictated by the combination of all these mechanisms leading to complex decay dynamics.

Since understanding the relaxation pathways is important, a number of tools have been developed for this purpose. Transient absorption spectroscopy allows the study of a wide range of dynamic processes down to sub fs timescales, and is widely employed to characterize the dynamics in semiconductor systems. A more detailed description of the transient absorption experiment will be given in the next section, but it is sufficient to say that without a thorough characterization of the electronic and optical properties the transient absorption dynamics can be nearly uninterpretable. In chapter VI we will study the carrier dynamics in size controlled TiS_2 to extract a basic understanding of the dynamics of carrier relaxation and how they are affected by the material anisotropy. We will also study the $\text{TiS}_2/\text{TiO}_2$ heterostructures to characterize the efficiency of electron transfer in hopes of tuning this system for potential photocatalytic use.

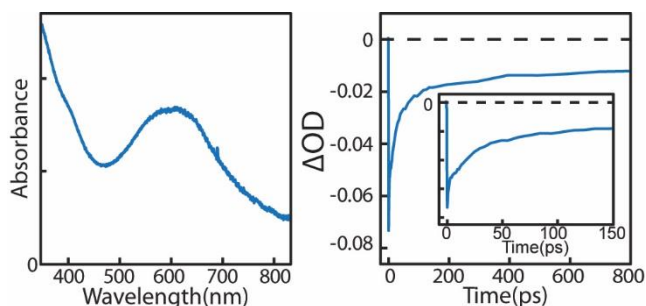


Figure 4: Absorption spectra of 100nm diameter TiS_2 nanodiscs (left) and bleach recovery dynamics (right) pumped at 800nm and probed at the maximum of the visible interband transition. Inset shows the short time dynamics.

Since the transient absorption study can be used to extract the dynamics on a sub ps timescale, it can be employed to study the effects of lateral confinement and layer number on the relaxation processes including carrier cooling, multi carrier relaxation, and electron transfer. For these studies, TiS_2 was used because the synthesis was well developed, it has an extinction

coefficient almost an order of magnitude larger than other semiconductors with comparable volume, and it can be easily formed into $\text{TiS}_2/\text{TiO}_2$ heterostructures via chemical oxidation. This is quite useful as preparation of heterostructures is typically a complicated experimental difficulty. Figure 4 shows a sample absorption spectra and decay dynamics from TiS_2 nanodiscs probed at the visible interband transition. It is difficult to know the exact nature of the time dependent processes in a system without detailed theoretical study, however since the carrier relaxation processes in semiconductors are rather general one can make inferences as long as the samples are well defined. In this case, the dynamics consist of fast (few ps) relaxation, and slow (many ns) relaxation, likely corresponding to carrier trapping or auger relaxation and the relaxation of either band edge or trapped charge carriers. In the TMDC materials the effects of anisotropy can extend to the carrier relaxation dynamics in that optical excitation couples differently to in-plane vs out-of-plane dipoles. The differences in coupling could be amplified in the structures with larger anisotropy such as the coupling if in plane polarized excitations to out of plane polarized excitations. Another interesting question which could be studied in the colloidal nanodiscs is how the anisotropy effects photoexcited carrier transport. In particular whether or not interlayer charge transport occurs, or whether carriers are confined to the plane they are generated in. The effects of lateral confinement were studied on size controlled TiS_2 nanodiscs, demonstrating pump energy selected electron hole excitations and faster relaxation dynamics in the larger particles, as well as a general insensitivity in the dynamics to the number of layers. In addition, the electron transfer time in the heterostructures were characterized demonstrating more complete relaxation in the $\text{TiS}_2/\text{TiO}_2$ compared to the bare TiS_2 .

1.3 Introduction to Perovskite Nanoparticles and Quantum Dots

1.3.1 Perovskite Nanomaterials Overview

Perovskites represent a diverse group of inorganic, organic, and mixed inorganic/organic solids which are currently one of the cutting edge materials for photonic and opto-electronic applications.⁴⁸⁻⁵⁰ The perovskite family of materials refers to the crystals with the structure $A^{2+}B^{4+}X^{2-}_3$ where X is either oxygen or halogen, and A/B are highly substitutable, leading to a highly diverse properties. Notably, these materials can be formed as both all inorganic and hybrid organic/inorganic where A and B are organic/inorganic cations.^{48, 51} While perovskite is a general term used for a family of materials, throughout this work, it will refer mainly to all inorganic $CsPbX_3$ or hybrid $[Organic]PbX_3$. In 2009 the first photo-voltaic utilizing a hybrid (methylammonium lead triiodide) perovskite film was prepared reaching ~3.8% power conversion efficiency, and in only seven years the efficiency of perovskite cells reached 22%.⁴⁹ Not only have these materials demonstrated remarkable properties for photo-voltaic devices, but they are solution and low temperature processable, making them an inexpensive alternative to other high efficiency devices. This unprecedented rate of advancement in the maturity of this technology is a testament to the robust optical and electronic properties of the perovskite materials.

The most important aspect of a solar cell is its ability to absorb photons efficiently, meaning materials with large absorption coefficients are desirable. An important feature of the hybrid perovskites is the large absorption coefficients, in fact, a 500nm thick perovskite can fully absorb one sun of illumination, compared to the 2 μ m thick films in typical solar cells.⁵² Along with strong absorption, the bandgap of mixed halide perovskites can be tuned from the near-UV to the near-IR, making it possible to dial in the cell efficiency.^{48, 52} After absorption of a photon, the photo-excited charge carriers must be extracted from the light absorbing material for use in a

photo-voltaic cell. There are numerous pathways which inhibit the efficiency of charge extraction, including as trapping, radiative recombination, and exciton formation. In most cells charge extraction tends to limit the efficiency. While charge extraction is a complex process, a few key material parameters help to characterize the efficiency, for example, carrier lifetimes, carrier mobility, and diffusion length. Hybrid perovskites boast superior performance in these areas as well, with diffusion lengths over 1 μm , high carrier mobility $25\text{cm}^2/\text{Vs}$, and long carrier lifetimes $> \mu\text{s}$.^{48, 52} The high performance of the perovskite solar cell has generated a boom in related research, specifically in the all inorganic materials.

The most significant problem facing hybrid perovskite solar cells is the instability in ambient conditions.^{48, 52} As these are polar crystalline materials with highly labile organic cations, the hybrid films tend to be highly soluble in polar solvent and are easily destroyed by humidity, particularly under illumination. For thin film devices, improving the device stability is currently the most important area of research which has lead to novel device architectures, designer organic cations, and the development of new all inorganic perovskites. Regardless of the methods to improve the stability, such as replacement of ligands with specially developed organics, and the development new solid-state hole scavenging materials, the organic cation instability continues to be a problem.⁵³⁻⁵⁴ The most viable solution to solve this problem has be the all inorganic perovskites, typically CsPbX_3 , where X is I, Br, or Cl. Not only does the removal of the organic cation increase the stability of the perovskite structure, it also dramatically reduces the cost and complexity of device manufacturing as the all inorganic materials can be formed in ambient conditions and devices can be made without specialized layers used to increase the hybrid stability.⁵¹

All inorganic perovskites were first prepared as films however they are now available as 1D, 2D and 3D confined wires, platelets and quantum dots, and recently the quantum dot/nanoparticle systems have received intense study.⁵⁵⁻⁵⁷ Perovskite nanoparticles and quantum dots have received special attention for a number of reasons, the synthesis is easy and the yields are high, the materials bandgap can be precisely tuned post-synthetically via a number of methods, the particles are highly soluble, albeit only in non-polar solvents, and they boast incredibly PL quantum yields >90% without post synthesis ligand treatment.^{55, 58-59} While many papers have been published in the last few years regarding the photo-physics of perovskite nanoparticles, most are plagued by problems such as sample inhomogeneity in both size distribution and particle shape.⁶⁰⁻⁶¹ The second half of this dissertation will discuss the optical properties and photo-physics of CsPbX₃ nanoparticles, quantum dots, and doped nanoparticles. We will focus in particular on the energy transfer dynamics in Mn-Doped CsPbCl₃, and the effects of quantum confinement on the photoexcited carrier dynamics, a topic our lab has a particular advantage in as we recently developed synthetic procedures for samples with the best size and shape control.

1.3.2 Confinement Effects in Quantum Dots

Semiconductor quantum dots exhibit size tunable properties that offer a diverse platform to study the confinement effects in quantum systems in the size ranges between bulk and atomic/molecular scales. Generically a quantum dot is described as a crystal with dimensions smaller than twice a_b , in this size regime the optical and electronic properties are affected by spatial confinement of the carrier wavefunctions. The most easily observed size tunable property in quantum dots is the blueshift of absorption and emission features with decreasing size. The confinement range is broken into strong, intermediate, and weak confinement regimes which correspond to size ranges where $a \ll a_b$, $a \sim a_b$, and $a \gg a_b$.⁶² This discussion will focus mostly on

quantum dots in the strong to medium confinement regime. To understand the basics of semiconductor quantum dots it is instructive to start with a discussion of CdSe which is probably the most well studied quantum dot system.

In quantum dots, the continuous bulk like energy states at the conduction and valence band edges are broken into discrete electron and hole energy levels. Compared to the smooth absorption spectra observed in the bulk, a series of transitions between discrete electron and hole levels are observed.⁶³ The wavefunctions of these discrete electron and hole states include contributions from the atomic orbitals which make up the bulk band edge states (Bloch functions), and an envelope wave function, typically a combination of Bessel functions and spherical harmonics forced to terminate at the particle surface.⁶² During the initial studies on CdSe quantum dots a useful notation was created to describe the wavefunctions of the confined carrier energy levels, typically each level is assigned a term nL_l . This term includes the radial and orbital angular momentum quantum numbers of the envelope function (n,L), and the total angular momentum including the envelope function and Bloch function (l), as well as the wavefunction symmetry. While a complete discussion of the carrier wavefunction is beyond the scope of this dissertation, it is important to note that the wavefunctions for all electron and hole states typically contain contributions from all valence/conduction band envelope functions/Bloch functions.⁶² In CdSe the mixing of valence band edge states, typically referred to as s-d mixing, is responsible for many of the unique size dependent properties in CdSe including the anomalous shifting of absorption features and strong size dependent oscillator strengths.⁶³ These calculations which were developed over a decade for CdSe can reproduce the size dependent optical properties with high accuracy, and in recent years have been used to describe the confinement effects in other systems such as PbS and CsPbX₃.

Full characterization of the electronic absorption spectra requires not only the energy levels, but also the strength of the transitions, characterized by the transition oscillator strength. In quantum dots, the transition oscillator strength is characterized by the dipole matrix element between the ground and excited state and the electron hole wavefunction overlap, $W_{g,ex} = \langle \psi_g | \frac{e}{r} | \psi_{ex} \rangle * \langle \psi_e | \psi_h \rangle$.⁶³ The first term dictates that the parity must change during an optical transition, and the second term that the electron and hole must have significant wavefunction overlap for a transition to be observed ($\int \psi_e * \psi_h \neq 0$). The typical selection rules considered for CdSe quantum dots are $\Delta L=0, \pm 1, \pm 2$ and $\Delta l=0, \pm 2$ which are both derived from the second term in the above equation. In complex systems such as CdSe, the strict selection rules are relaxed due to the strong mixing of valence and conduction band states.⁶³ The energy of the transitions can be written down as:

$$\hbar\omega = E_g + E_e + E_h^{\pm} - E_{eh}$$

where \pm revers to odd or even hole wave functions, E_g the bulk bandgap, and E_{eh} the electron hole coulomb interaction.

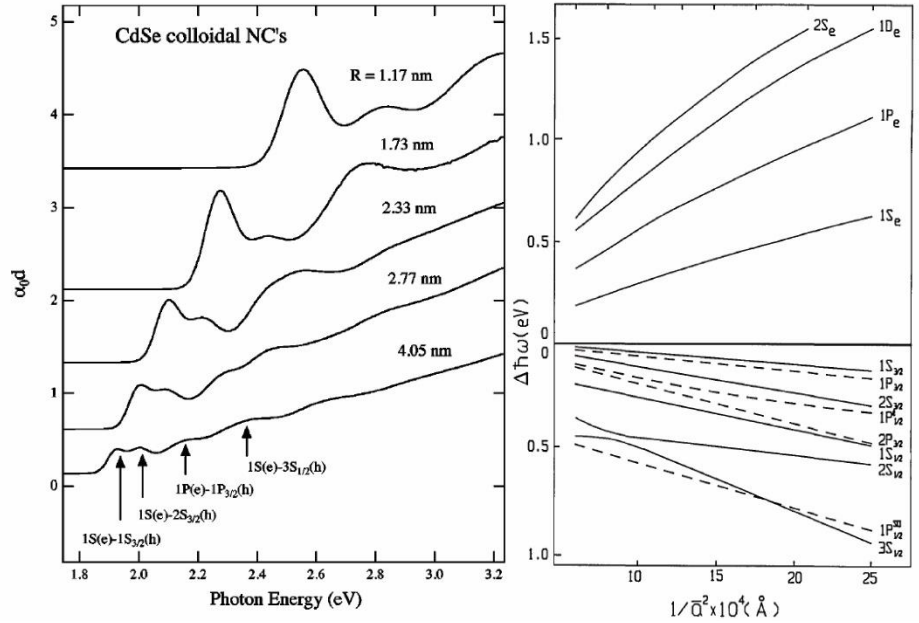


Figure 5: Size dependent absorption spectra from a series of strongly confined CdSe quantum dots. The lowest energy transitions are labeled (left). Size dependent energy levels of the lowest electron and holes stats as a function of particle size (right). (Reprinted in part with permission from Zuoli He, Wenxiu Que. The Electronic Structure of Semiconductor Nanocrystals. *Annu. Rev. Mater. Sci*, **2000**, 30, 475-521. Copyright 2000 by Annual Reviews.)⁶²

The study of size dependent absorption and emission in quantum dots is an important tool which directly probes changes to the underlying electronic structure. For CdSe where the lowest interband absorption is in the visible region, the effects of quantum confinement are easily studied with linear and non-linear spectroscopy. Figure 5 shows a series of absorption spectra and the size dependent electron-hole levels for strongly confined CdSe quantum dots. The fact that the interband absorption is in the visible does not inherently make spectroscopic studies easier, it is merely a practical matter that visible spectroscopies are easier to handle and more developed compared to UV and nIR/IR.⁶⁴

Comparison of the absorption spectra and assigned transitions reveals the absence of interband transitions between electron and hole states with S and P character. Strictly speaking,

these transitions are not forbidden do the strong s-d mixing of valence and conduction band states, yet they still have vanishingly small oscillator strengths.⁶⁵ It is however possible to observe these transitions via nonlinear optical techniques or modification of oscillator strength via external stimulus. The two photon absorption oscillator strength follows more complicated selection rules than the single photon absorption, and strong resonances at formally dark transitions can be excited. In the two photon PLE from CdSe quantum dots, the strongest transition is to the $1S_{3/2}$ - $1P_{3/2}$ excitation which has nearly zero oscillator strength in the linear absorption.⁶⁶ The presence of electric or magnetic fields can also be used to turn on formally forbidden transitions. For example, electric fields formed via an internal dipole moment or by the application of an external field, serves to break the symmetry in the quantum dot and perturb the electron and hole wavefunctions, which in turn leads to adjusted oscillator strength of all transitions. The broken symmetry in wurtzite structure CdSe quantum dots act to turn on dipole forbidden transitions, as is observed in the two photon PLE spectra where the lowest energy exciton is still observed even though it has a zero classical oscillator strength.⁶⁷ Another commonly studied case where the dipole forbidden transitions can be observed is in PbS quantum dots. From this point of view, PbS quantum dots are arguably more interesting in that the formally dark transitions can be observed even in the single photon absorption spectrum.⁶⁸ In the PbS system, the symmetry of the crystal structure results in a different set of optical selection rules compared with CdSe. In contrast to CdSe, there is no s-d mixing and the parity of the wavefunction remains a good quantum number. As a result, the parity selection rule which is dropped in CdSe remains in PbSe. It is common however to observe the parity forbidden transitions even in the single photon absorption spectra.⁶⁸ Currently there is no single accepted explanation for this, however it is believed that inherent asymmetry in the low dimensional quantum dots results in a breaking of this selection rule.⁶⁹

Interestingly the amplitude of this dipole transition can be increased in the presence of an electric field, as is observed when high energy charge carriers generate a transient dipole moment which results the increase in oscillator strength for this transition.⁷⁰

1.3.3 Doped Semiconductor Nanomaterials

Another pathway to introduce new optical and electronic properties is quantum dots is the intentional doping of atoms and defects into the lattice. Dopants can range from electronically inert such as Mn^{2+} to donor/acceptors such as Cu^+ , which can ionize and provide electrons or holes to the system.⁷¹ These dopants can introduce various carrier and energy relaxation pathways including charge and energy transfer. For example, in Cu^+ doped CdSe, photoexcited holes can transfer to Cu, after which electrons recombine with Cu^{2+} yielding long lived ($> \mu\text{s}$) PL which is strongly red-shifted and broadened from the exciton.⁷² In Mn^{2+} doped QD excitons to Mn energy transfer to the Mn ligand field state competes with carrier recombination, yielding dual color emitting particles with long lifetimes.⁷¹ In chapter VIII we will discuss the exciton to Mn energy transfer in doped CsPbCl_3 nanoparticles and the competition between energy transfer and carrier trapping dynamics.

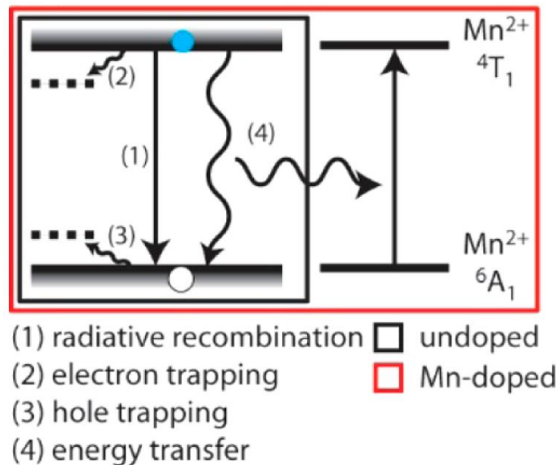


Figure 6: Schematic energy level diagram of undoped and Mn doped CsPbCl₃ nanoparticles. with the conduction and valence band, trap states, and Mn ligand field transitions. Note the energy scale is not correct as the absolute energy levels are unknown. (Reprinted in part with permission from Daniel Rossi, David Parobek, Yitong Dong, and Dong Hee Son. Dynamics of Exciton-Mn Energy Transfer in Mn-Doped CsPbCl₃ Perovskite Nanocrystals. *J. Phys. Chem. C*, **2017**, 121(32), 17143-17149. Copyright 2017 by the American Chemical Society.)⁷³

In Mn-doped II-VI quantum dots, Mn ions are doped at metal center and is coordinated with four S or Se atoms. The electronic structure of Mn²⁺ in this system is well described with ligand-field theory. For the free Mn²⁺, the ground state with 5 d-electrons is 6-fold degenerate in the high spin configuration. When the tetrahedral ligand field is applied, the ground state remains symmetric (⁶A₁) and the first excited state splits into (⁴T₁, ⁴T₂, and degenerate ⁴A₁/⁴E) making the lowest energy transition ⁴T₁ – ⁶A₁. A schematic of the lowest energy ligand field transition relative to the CdSe conduction band is seen in figure 6. It is critical to note that 1) this transition requires the flip of a spin making it optically forbidden and 2) the energy absolute energy levels of the Mn dopant are not sensitive to the particle size, and depend only on the local lattice coordination chemistry.

The ${}^4T_1 - {}^6A_1$ transition requires a spin flip meaning it is a forbidden transition with nearly zero oscillator strength, explaining the lack of Mn absorption in the UV-Vis. Regardless, strong Mn emission, up to 95% quantum yield, can be observed from Mn doped CdSe nanoparticles when excited above the particles band edge. Following photo-excitation, the exciton energy is transferred to the Mn via Dexter energy transfer, a process that is not restricted by the spin flip.⁷⁴ The slow Mn emission is observed due to the partial breaking of the optical selection rules due to spin orbit coupling and Mn-Mn exchange interactions.⁷¹ While the localized nature of the excited Mn makes the PL insensitive to quantum confinement effects, the efficiency of forward and back energy transfer can be tuned with the band edge, as the absolute energy of the electron and hole energy levels becomes similar in to the Mn^{2+} .

Mn doped CdSe and CdS quantum dots have found a number of unique applications. The long lifetime of the Mn excited state has been used in as a long lived energy reservoir, and in various magneto-optic experiments. In Mn doped CdS/ZnS core shell quantum dots, following the first energy transfer, the lifetime of the excited Mn is longer than the optical cycle of the exciton even under low intensity, meaning it is possible to excite both Mn and an exciton in the same particle. In the double excited particles, back energy transfer of the Mn to the excited exciton produces hot electrons. The hot electrons produced with this method had enough kinetic energy to be ejected into the vacuum under zero bias.⁷⁶

1.3.4 Carrier Relaxation in Quantum Dots

In the past few decades the advancement of both material preparation and time domain measurements, including fast gated cameras and ultrafast spectroscopy systems, have allowed the detailed study of carrier dynamics in confined semiconductors. A particularly interesting question is how the effects of discretization of the band edge states manifest changes to the relaxation

dynamics in confined semiconductor systems. While the time domain PL measurements have been utilized to study the radiative relaxation processes such as nanoparticle blinking, long lived dark states, and multicarrier emissions, we will focus on ultrafast time resolved absorption measurements. Ultrafast absorption measurements take advantage of high power pulsed lasers, with pulse widths as short as 100s of attoseconds, to resolve carrier dynamics on an ultrafast (typically sub ps) timescale. While there are numerous ultrafast experiments which can be used to probe many nonlinear optical processes, pump-probe transient absorption is the most commonly used to study the relaxation dynamics in semiconductors.

In the typical pump probe experiment, a high-power pump pulse is used to excite a sample and a low power probe is used to examine some optical property of the excited state. In the pump probe setup, the time domain is recovered by introducing a path length difference between the pump and probe, which introduces a delay time, and the modulation of the probe as a function of delay time is measured. Utilizing high accuracy translation stages, delay times to ~ 0.5 fs can be introduced, and down to 10s of attoseconds with more sophisticated techniques. Short pulsed lasers are particularly useful for these experiments as their high power allows for a variety of nonlinear frequency mixing techniques, such as parametric down-conversion, to access nearly any combination of pump and probe wavelength. The time resolution of these experiments (< 100 fs is easily attainable) makes it possible to resolve dynamic processes not observed in other methods such as fast charge/energy transfer and hot carrier cooling.

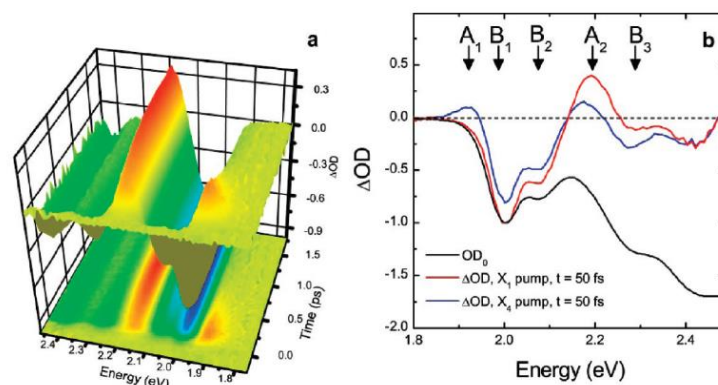


Figure 7: Color contour plot of the pump probe data from CdSe quantum dots (left). Early time bleach signal from the same sample overlaid on the absorption spectra demonstrating the bleach features and corresponding absorption features (right). (Reprinted in part with permission Patanjali Kambhampati. Unraveling the Structure and Dynamics of Excitons in Semiconductor Quantum Dots. *Acc. Chem. Res.*, **2011**, 44(1), 1-13. Copyright 2016 by Elsevier.)⁷⁷

Figure 7 (left) shows a 2D plot of the visible transient absorption signal from CdSe quantum dots, the y axis corresponds to the pump probe delay time, the x axis the probe wavelength, and the z axis the change in absorption due to the pump, ΔOD .⁷⁷ One of the difficulties in analyzing transient absorption data is understanding the origin of the signal. The transient absorption spectra is typically composed negative and positive signals corresponding to bleached absorption features, stimulated emission, and induced absorptions, as well as more complex signals such as spectral shifting from carrier-carrier interactions. Pump probe data overlaid on onto the absorption spectra of CdSe in figure 7 (right) shows clearly that the bleach features overlap with the electron-hole absorption features, typically called a state filling bleach resulting from the change in occupancy of the electron-hole states at that energy. Extracting information from the time dependent dynamics however can be tricky, as both excited electrons and holes can induce a change in absorption, making knowledge of the detailed electronic structure critical. Typically, the

degeneracy of the band edge will provide the most useful information for understanding the time dependent dynamics. For example, in CdSe, the band edge electron and hole degeneracy are two and six respectively. After excitation the total occupation of the electron state is $1/2$ and the hole $1/6$, making the electron the dynamics the dominant feature. In this picture, the band edge dynamics can be used as a measure of the electron recovery, and any perturbation which removes or adds electrons will be reflected in the dynamics of the band edge signal, while perturbations resulting in changes to hole populations are not observed.

Recently, a significant effort has focused on the spectroscopic characterization of CsPbX₃ nanoparticles.^{60, 78-79} While there are a number studies focusing on the dynamics using PL and transient absorption, the lack of high quality samples has made the vast majority of studies prone to significant error. Recently, improved synthetic methods have made available highly uniform, confined samples, which we will use to study the effects of quantum confinement in CsPbBr₃. This is a topic of particular interest, as the effects of confinement in CsPbX₃ quantum dots are unstudied, and the few papers reporting on the dynamics of carrier relaxation and confinement effects have misrepresented the spectroscopic signatures.^{60, 80} Furthermore, the lack of detailed electronic structure calculation has made analysis of spectroscopic data difficult.

Some of the more recent studies have rectified these problems using high quality samples synthesized from more mature procedures, studying single particles, and one of the most recent paper produced similar calculations used to characterize CdSe quantum dots.⁸¹⁻⁸² Regardless there is a need to reexamine much of this work with more quality materials. Recently our lab has developed protocol for the synthesis of both high quality doped and undoped CsPbCl₃, as well as strongly confined CsPbBr₃, giving us the opportunity to study the size dependent properties of impurity free, monodispersed samples in more detail.

In chapter VII and VIII we will use transient absorption spectroscopy to study the dynamics of carrier relaxation in Mn doped CsPbCl₃ and confined CsPbBr₃ nanoparticles and quantum dots. Comparing the exciton relaxation dynamics in Mn doped and undoped CsPbCl₃ we will extract the exciton to Mn energy transfer time. In the CsPbCl₃ the energy transfer time is about twice as long as in II-IV quantum dots, however this is not surprising considering the relatively small comparative Bohr radius. We will also describe the surface reconstruction during the Mn doping process leading to improved exciton quantum yield in the doped particles, an unusual observation and Mn energy transfer typically quenches exciton emission. We will also provide the first systematic transient absorption study on highly uniform size controlled CsPbBr₃ quantum dots. We have observed the turning on of a formally forbidden transition in the presence of excited electron-hole pair, a phenomena not typically seen in semiconductor quantum dots. Such an observation suggests some form of symmetry breaking in the excited state, likely the electron-hole pair form a dipole as opposed to the common diffuse exciton. We will discuss this phenomena in the context of a dipole mediated by polaron formation, a commonly discussed phenomena in CsPbX₃ materials.

CHAPTER II

EXPERIMENTAL DETAILS^{*,†,‡}

2.1 Transient Absorption Measurements

Transient absorption experiments were measured in the pump-probe setup. For all experiments pump wavelengths of either 790 or 395 nm were used. The fundamental 790nm, 75 fs pulses were obtained at 3KHz repetition rate from an amplified Ti:Sapphire laser (KM Labs). 395nm pump pulses were obtained via frequency doubling in a 300 μm -thick β -BBO crystal. Pump powers were controlled with a half wave plat – polarizer. Several μJ of the 790 nm beam was focused onto a translating CaF_2 window to generate a stable supercontinuum, which was used as the probe beam. The wavelength for the probe was selected via either a prism pair and spatial filter, or a monochromator. A portion of the probe was sampled and used as a reference to improve the signal to noise ratio. ΔOD was recovered taking the ratio of every other pulse as the pump is chopped at 1.5 kHz. The typical noise levels were between 10^{-5} and 10^{-4} ΔOD . Transient absorption spectra were collected with the same laser setup, however the full probe and reference spectra were

* Reprinted in part with permission from Daniel Rossi, Jae Hyo-Han, Dongwon Yoo, Yitong Dong, Yerok Park, Jinwoo Cheon, Dong Hee Son. Photoinduced Separation of Strongly Interacting 2-D Layered TiS_2 Nanodiscs. *J. Phys. Chem. C*, **2014**, 118(23), 12568-12573. Copyright 2014 by the American Chemical Society.

† Reprinted in part with permission from Daniel Rossi, Luis E. Camacho-Forero, Guadalupe Ramos-Sanchez, Jae Hyo Han, Jinwoo Cheon, Perla Balbuena and Dong Hee Son. Anisotropic Electron-Phonon Coupling in Colloidal Layered TiS_2 Nanodiscs Observed Via Coherent Acoustic Phonon. *J. Phys. Chem. C*, **2015**, 119(13), 7436-7442. Copyright 2015 by the American Chemical Society.

‡ Reprinted in part with permission from Daniel Rossi, David Parobek, Yitong Dong, and Dong Hee Son. Dynamics of Exciton-Mn Energy Transfer in Mn-Doped CsPbCl_3 Perovskite Nanocrystals. *J. Phys. Chem. C*, **2017**, 121(32), 17143-17149. Copyright 2017 by the American Chemical Society.

monitored using ocean optics STS spectrometers. In this experiment, ΔOD was obtained by measuring hundreds of pulses while block and unblocking the pump. For the near-degenerate pump and probe wavelengths, the polarization of the pump was set perpendicular to the probe polarization in combination with a polarizer placed in front of the detector to avoid intense pump scattering. The nanocrystal samples dispersed in cyclohexane were continuously circulated in a 2 mm-pathlength flowing cell to avoid any potential photodamage of the sample.

2.2 Synthesis of TMDC Nanoparticles

TMDC nanodiscs were synthesized by our collaborators from Dr. Cheons group at the Yonsei university in South Korea. Details of the synthesis are outlined in a number of publications.^{24, 26, 83} The typical synthesis follows a hot injection methods, where CS₂ is injected into a solution of metal chloride (MX₄) in oleylamine at 300 °C. Typical synthesis are The size of the nanodiscs were controlled by adjusting the concentration of the precursors. X-ray diffraction (XRD) patterns of TiS₂ nanodiscs were obtained on a Bruker-AXS D8 powder diffractometer with Cu- α X-ray source. Transmission electron micrograph (TEM) were obtained with FEI Tecnai G2 F20 FE-TEM operating at 200 kV. The molar extinction coefficient of TiS₂ nanodiscs used to estimate the photoexcitation density was obtained from the particle size measured from TEM and concentration of Ti ions from the elemental analysis. The elemental analysis was performed employing inductively coupled plasma mass spectrometry (Perkin-Elmer DRCII ICP-MS) using commercial ICP standard solution for Ti ions (Fluka).

2.3 Synthesis of CsPbBr₃ Quantum Dots

Synthesis of CsPbBr₃ quantum dots is can be found in a recently accepted publications from our group. The precursor solution of Pb and Br was prepared by dissolving PbBr₂ (75 mg), CoBr₂ (250 mg) in a mixture of ODE (5 mL), OA (2 mL) and OAm (2 mL) in a 25-mL three necked round bottomed flask under N₂ atmosphere at 120 °C for 1 min. Then the temperature was raised to 180 °C followed by a swift injection of 0.4 mL Cs-oleate precursor. The reaction was quenched with an ice bath after ~10 s. Once the reaction was cooled to room temperature, the QD solution was centrifuged at 3500 rpm for 10 min to remove the unreacted salt. ~8 mL of acetone was directly added into the supernatant to precipitate the QD followed by centrifuging at 3500 rpm for 3 mins. The precipitants were collected and dissolved in ~1 mL of hexane.

2.4 Synthesis of Mn-Doped CsPbCl₃ Nanoparticles

The synthesis of undoped and Mn-doped CsPbCl₃ nanocrystals were performed following the procedures we recently developed in our group.⁸⁴ For the synthesis of the undoped samples, PbCl₂ (0.0654 g), OAm (0.8 mL), OA (0.8 mL), and ODE (5 mL) were added to a 25-mL 3 neck round bottom flask. For the Mn-doped samples, PbCl₂ (0.0584 g), MnCl₂·(H₂O)₄ (0.0615 g), Oam (0.8 mL), OA (0.8 mL), and ODE (5 mL) were added to a 25-mL 3 neck round bottom flask. Both solutions were evacuated and refilled with nitrogen three times followed by heating to 120 °C for 30 minutes then to 165 °C and 200 °C for 10 minutes each. At 200 °C, additional OA (0.8 mL) and Oam (0.8 mL) were injected to solubilize the solution. Then 0.4 mL of the Cs-oleate solution was swiftly injected followed by rapid quenching after 1 minute of reaction time. The synthesized nanocrystals were collected by precipitating with acetone followed by centrifugation and resuspension in hexanes. The perovskite NCs were further cleaned through additional precipitation with ethyl acetate followed by suspending the collected NCs in hexanes.

CHAPTER III

PHOTOINDUCED SEPARATION OF STRONGLY INTERACTING 2-D LAYERED TiS₂ NANODISCS IN SOLUTION*

3.1 Introduction

Atomically thin 2-D layered transition metal dichalcogenide (TMDC) nanostructures are attracting much attention due to their material properties that are sensitive to the number of the layers and the strength of their interlayer interaction.^{12, 85-87} Often these materials are synthesized via exfoliation from the bulk or using CVD methods, which produced single and few-layer thin flakes enabling detailed studies of the thickness dependent material properties of TMDC.^{85, 88-90} Recently, solution-phase synthesis methods have been developed for several TMDC materials, enabling the production of uniform ensembles of colloidal TMDC nanodiscs with controlled thickness and lateral area simultaneously.⁹¹ Colloidal 2-D layered TMDC nanodiscs with controllable thickness and area provide a unique opportunity to explore the material properties correlated with both variation of interlayer interaction and intralayer spatial confinement that are expected to be highly anisotropic.⁸⁵

Optical absorption has frequently been used to correlate the electronic structure with the dimensions or morphology of the colloidal nanoparticles, provided that the size and shape distributions are narrow and the particles are well separated within the solution.^{37, 92} In typical colloidal solutions of inorganic nanoparticles, surface-bound ligands or surface ions provide the

* Reprinted in part with permission from Daniel Rossi, Jae Hyo-Han, Dongwon Yoo, Yitong Dong, Yerok Park, Jinwoo Cheon, Dong Hee Son. Photoinduced Separation of Strongly Interacting 2-D Layered TiS₂ Nanodiscs. *J. Phys. Chem. C*, **2014**, 118(23), 12568-12573. Copyright 2014 by the American Chemical Society.

colloidal stability, keeping the particles separated from each other. Ordered assemblies or aggregates of the interacting particles can also form within the solution depending on the factors that determine the balance between interparticle cohesive energy and particle solvation, such as surface passivation, solvent polarity and etc. Interparticle interactions and the formation of the assemblies of interacting particles is an important issue, since the electronic, optical and transport properties of the particles can change significantly via electronic coupling.^{36, 38-39, 93-94} Colloidal 2-D layered TMDC nanodiscs have large flat basal planes and the possible interparticle contact area that affects interparticle cohesive energy and electronic coupling is much larger than in 0-D and 1-D structures of the same volume. Therefore, the formation of interacting assembly of particles is more facile than in 0-D and 1-D structures and its effect on the optical and electronic properties can also be more significant.^{13, 95} The alteration of the optical properties due to interparticle electronic coupling can pose a challenge in exploring the unique dimensionally anisotropic properties of transition metal dichalcogenide nanostructures using colloidal nanoparticles with well-controlled lateral and transverse dimensions.

In this study, we show that the vertically stacked assemblies of TiS₂ nanodiscs present in the colloidal solution due to the strong interparticle interaction via basal planes can be readily separated into individual non-interacting nanodiscs via pulsed photoexcitation. Interband photoexcitation of TiS₂ nanodiscs with pulsed laser light creates dense charge carriers that transiently modify the charge distribution within the nanodiscs. The change in charge distribution in TiS₂ nanodiscs during the lifetime of the charge carriers is considered to nonthermally weaken the interparticle cohesive energy and facilitate the solvation of each nanodisc by the solvent molecules as illustrated in Figure 8. Since the basal planes of TiS₂ are polar, photoinduced separation was particularly efficient in polar solvent media. The capability to optically modify the

interparticle interaction and prepare non-interacting colloidal TMDC nanoparticles in solution will be important in exploring their properties correlated with lateral and transverse dimensions without contamination from the strong interparticle coupling.

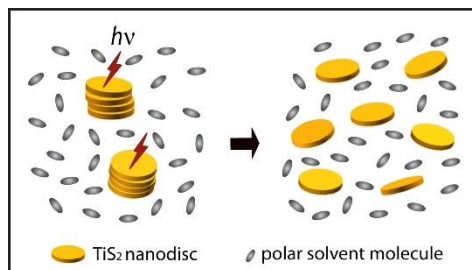


Figure 8: Separation of strongly interacting colloidal 2-D layered TiS₂ nanodiscs via photoinduced weakening of interparticle cohesive energy that facilitates the solvation of each nanodisc.

3.2 Results and Discussion

The photoinduced separation of the assemblies of the strongly interacting TiS₂ nanodiscs and the consequent changes in the optical properties were studied from the measurements of the optical extinction spectra, dynamic light scattering (DLS), X-ray diffraction patterns. Transmission electron micrographs of the colloidal TiS₂ nanodiscs before and after the photoexcitation were obtained to examine the morphology of the assemblies and individual nanodiscs. The effects of ultrasonication, commonly used to disperse the interacting nanoparticles, on the optical extinction and DLS are also contrasted with those of the photoexcitation.

Figure 9a,b show the effects of photoexcitation and ultrasonication on the optical extinction spectra of colloidal TiS₂ nanodiscs of two different sizes ($d=50$ and 150 nm) dispersed in deoxygenated chloroform. Blue and green curves are the spectra of the as-synthesized TiS₂ samples with 1 hr and 10 hrs of ultrasonication respectively. Red curves are from the samples after 1hr of ultrasonication and additional 10 mins of pulsed photoexcitation at 800 nm ($1.4\text{W}/\text{cm}^2$, $\sim 100\text{fs}$, 3kHz repetition rate). The broad peaks in the visible and near infrared region are attributed to the higher-energy interband transitions above the bulk bandgap of roughly 0.1 eV.^{88,96-97} Both nanodiscs samples exhibit qualitatively similar spectral features. On the other hand, the peaks occur at the shorter wavelengths in the smaller nanodiscs, which may reflect the confinement in lateral or (and) transverse dimensions. Figure 9c,d are the effective hydrodynamic diameter distributions corresponding to Figure 9a,b, estimated from the dynamic light scattering (DLS) measurements. With increasing ultrasonication time and with photoexcitation, the distribution of hydrodynamic diameter shifts to the smaller values. In this study, we will interpret DLS data rather qualitatively, since the data was analyzed with a model assuming the spherical particle shape that is limited in describing the behavior of the disc-shaped particles. It is however important to note

that the average dimensions of a single disc not change after irradiation. From TEM measurements after laser irradiation, the average diameter of the $d=150$ nm nanodiscs was 150.87 ± 16.9 nm, and the average thickness was 8.95 ± 1.55 nm.

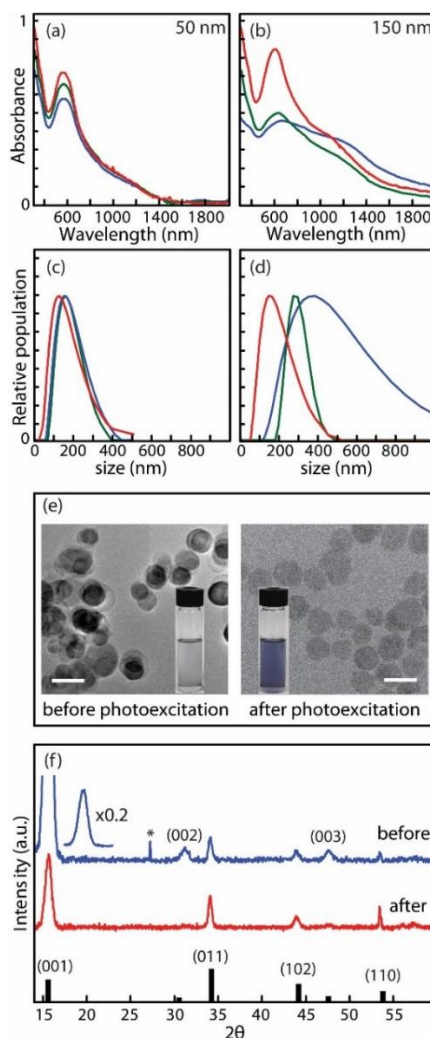


Figure 9: (a),(b) Extinction spectra and (c),(d) effective hydrodynamic diameter distributions of the colloidal TiS₂ nanodiscs of two different sizes after ultrasonication or photoexcitation. (Blue) 1 hr ultrasonication, (Green) 10 hrs ultrasonication, (Red) 1 hr ultrasonication and 10 mins of pulsed photoexcitation at 800 nm. $d=50$ nm for (a), (c) and $d=150$ nm for (b), (d). (e) TEM image of $d=150$ nm TiS₂ sample before and after 30 mins of photoexcitation. Scale bar is 200 nm (f) XRD patterns of $d=150$ nm TiS₂ nanodiscs before and after 30 mins of photoexcitation. The vertical bars represent the standard XRD pattern of bulk TiS₂ (ICSD #: 000-015-0853). * is noise.

An important feature observed in Figure 9a-d are that the optical extinction spectra of the colloidal TiS₂ nanodiscs vary with the size of the assembly of the interacting nanodiscs. In $d=150$ nm sample, the peak near 600 nm, assigned to the interband transition from right below the Fermi level to the band in Σ M direction,⁹⁷ blueshifts with a significant increase in the intensity as the hydrodynamic diameter decreases. The blueshift in the extinction spectra with decreasing size of the nanodiscs assembly may be interpreted as the decreasing extent of the interparticle electronic coupling that widens the gap between the bands.^{90, 98} In $d=50$ nm sample, spectral change in the extinction spectra by the ultrasonication and photoexcitation is less pronounced than in $d=150$ nm sample while the trend is similar. The relatively weak effect of the photoexcitation and ultrasonication in $d=50$ nm nanodiscs is likely due to the smaller interparticle cohesive energy resulting in less extent of the assembly formation than in the nanodiscs with the larger diameter. Smaller interparticle cohesive energy in the $d=50$ nm sample results in a pre-laser irradiated sample with an absorption spectra representative of individual colloidal nanodiscs, whereas laser irradiation is required to obtain such an absorption spectra for $d=150$ nm particles. As such, the pre-irradiated $d=50$ nm absorption spectra appears similar to the post-irradiated $d=150$ nm absorption spectra. The tendency to form the assemblies of the interacting particles in the chemically synthesized TiS₂ nanodiscs can be understood from the relatively poor passivation of the flat basal planes during the synthesis. In 2-D layered TMDC nanodiscs, the basal planes are composed of chalcogens with no dangling bonds, whereas the atoms at the edges are not fully coordinated. Therefore, oleylamine used as the surfactant will bind preferentially to the edge atoms during the synthesis and leave the basal planes exposed for more facile interparticle interaction and the formation of vertically stacked assemblies along the c -axis as shown in Figure 9e.⁹⁹⁻¹⁰⁰

Another noteworthy observation in Figure 9 is that the photoexcitation is much more efficient in separating the assemblies of $d=150$ nm TiS_2 nanodiscs than ultrasonication. In fact, nearly complete separation of the assemblies into individual TiS_2 nanodiscs could be achieved after tens of mins of photoexcitation as will be discussed later, whereas ultrasonication can only reduce the size of the assemblies even after 10 hrs. TEM images in Figure 9e show that the vertically stacked assemblies of TiS_2 nanodiscs present in the sample before the photoexcitation are well separated after 30 mins of photoexcitation. The resulting changes in the optical extinctions spectra is clearly visible in the photographs of the sample before and after the photoexcitation shown in Figure 9e. XRD patterns in Figure 9f also indicate that the lattice structure of TiS_2 nanodiscs remains the same after the photoexcitation. On the other hand, (001), (002) and (003) diffraction peaks attenuated significantly after the photoexcitation, consistent with the removal of the stacking along the c -axis. No sign of photoinduced structural degradation or change in diameter and thickness of the nanodiscs was observed in TEM images, when the deoxygenated solvents were used to prevent the photooxidation. However, partial photooxidation of TiS_2 to TiO_2 can occur in the presence of the dissolved oxygen in solvent and the resulting $\text{TiS}_2/\text{TiO}_2$ heterostructures are readily identified in TEM and XRD as shown in reference 173.^{91, 101}

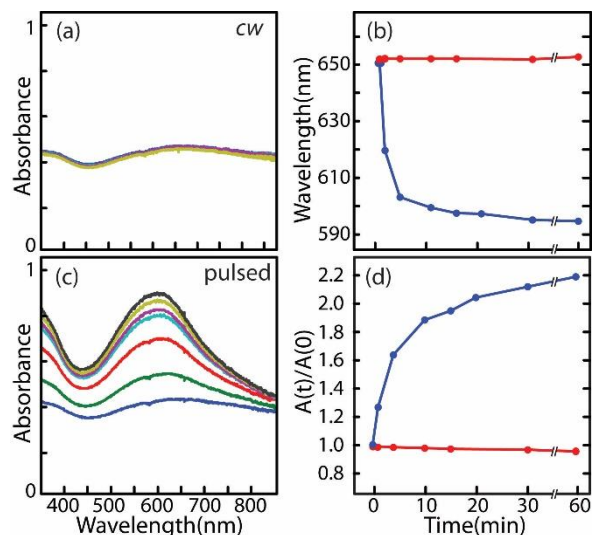


Figure 10: (a), (c) The time-variation of the absorption spectra of $d=150\text{nm}$ TiS_2 nanodiscs in chloroform under (a) *cw* and (c) pulsed laser irradiation condition. (b) Time-dependence of the peak position under *cw* (red) and pulsed (blue) laser irradiation. (d) Time-dependence of the peak intensity, $A(t)$, normalized to the initial intensity, $A(0)$, under *cw* (red) and pulsed (blue) laser irradiation.

The data in Figure 9 indicate that the photoexcitation can separate the strongly interacting TiS_2 nanodiscs, which may be more generally applicable in other layered colloidal transition metal dichalcogenide nanodiscs if the same mechanism is in operation. In order to gain an insight into the mechanism of the photoinduced separation of the strongly interacting TiS_2 nanodiscs, several comparative analyses were made under varying photoexcitation conditions and in solvents with different polarities. Figure 10a,c show the effect of *cw* and pulsed photoexcitation on the extinction spectrum of $d=150\text{ nm}$ TiS_2 nanodiscs dispersed in deoxygenated chloroform as a function of photoexcitation time. Both *cw* and pulsed laser beams at 800 nm had the same average intensity of $\sim 1.4\text{ W/cm}^2$. The variations of the peak position and intensity are plotted in Figure 10b,d. A blueshift and an increase in intensity of the interband absorption peak were observed only with the pulsed excitation, whereas *cw* excitation had no effect. Furthermore, the spectral blueshift and

increase of the intensity saturated in ~10 and ~30 mins respectively, with negligible additional change up to 120 mins of continued photoexcitation. Considering that the TEM image of the TiS₂ nanodiscs after 30 mins with pulsed photoexcitation shown in Figure 9e has mostly the isolated nanodiscs, the saturation of the blueshift and intensity of the peak can be interpreted as the completion of the separation of the interacting nanodiscs.

While it is intriguing that only the pulsed excitation is capable of dispersing the assembly of interacting TiS₂ nanodiscs and induces a large spectral change, it provides a useful insight into the possible mechanisms of the photoinduced separation. We ruled out direct heating of the lattice by the absorbed photons as the possible cause of the photoinduced separation of the nanodiscs. The upper limit of the local lattice heating in each nanodisc, assuming no heat dissipation to the solvent, was only $\Delta T=20$ °C under the pulsed excitation condition based on the extinction coefficient of the nanodisc and the fluence of the excitation light. (see reference 173) Actual local lattice heating should be significantly lower than this estimate due to the rapid heat dissipation from the lattice to the solvent. Steady-state heating of the entire colloidal solution at 40 °C (20 °C higher than the ambient temperature) had no effect on the optical spectra and dispersion of TiS₂ nanodiscs, ruling out the local lattice heating as the driving force for the photoinduced separation. We also ruled out potential involvement of two-photon process, since *cw* excitation at 405 nm with comparable intensity did not have any effect on the extinction spectrum.

Photoinduced separation of the interacting nanodiscs only by the pulsed excitation may be explained by the relatively high *instantaneous* excitation density (2.4×10^4 /particle in $d=150$ TiS₂, see reference 173) from each pulsed excitation in contrast to the low *steady-state* excitation density (7.3×10^{-2} /ns·particle in $d=150$ nm TiS₂) from *cw* excitation. The interband excitation shifts charge distribution from S to Ti and potential trapping of the charge carriers will accumulate localized

charges at the trapping site, such as the surface of the nanodiscs, during their lifetime of a few to tens of ns.¹⁰¹⁻¹⁰² Therefore, the pulsed excitation will transiently modify the charge distribution in TiS₂ nanodiscs, whose magnitude increases with the *instantaneous* excitation density. If the transient modification of charge distribution is sufficiently large and capable of weakening the interparticle cohesive force, each laser pulse can provide an additional driving force favoring the solvation of the individual nanodiscs by the surrounding solvent molecules. Since the typical organic solvent molecules with diffusion coefficient of $\sim 10^{-9}$ m²/s can self-diffuse ~ 10 nm in tens of ns, solvent molecules will have sufficient time to intervene between the nanodiscs taking advantage of the weakened cohesive force. The above hypothesis is also corroborated by the slower rate of spectral change observed from the photoexcitation with longer laser pulses (0.1-1 ns) of the same average intensity that produces the lower instantaneous excitation density due to the charge carrier relaxation during the period of pulse width.

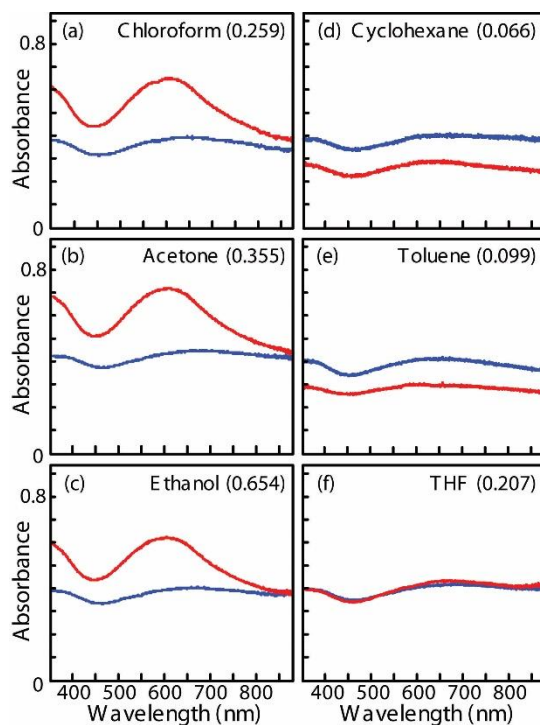


Figure 11: The effect of solvent polarity on laser-induced changes in the absorption spectra of $d=150$ nm TiS_2 nanodiscs. Blue and red curves are before and after 5 min of pulsed laser irradiation respectively. The relative solvent polarity with respect to water is indicated in each panel.

To further test the hypothesis of the photoinduced separation via the facilitated solvation of TiS_2 nanodiscs, we compared the efficiency of the photoinduced separation of the nanodisc assemblies in solvents of varying polarities. Figure 11 compares the optical extinction spectra of $d=150$ nm TiS_2 nanodiscs before and after the pulsed photoexcitation for 5 mins in each solvent. Interestingly, the spectral change was observed only in relatively polar solvents. In nonpolar solvents, such as cyclohexane and toluene, no spectral shift was observed even when the sample was photoexcited much longer. The decrease of the intensity after the photoexcitation in cyclohexane and toluene is due to the deposition of TiS_2 nanodiscs on the surface of cuvette, not the degradation of the nanodiscs. The above observation indicates that photoinduced solvation of

each TiS₂ nanodisc is preferred by the polar solvents, which is consistent with polar nature of the exposed basal planes composed of S atoms. Unfavorable solvation of the polar surface with nonpolar solvents will explain the inability of cyclohexane and toluene to separate the interacting particles. The photoexcited TiS₂ nanodiscs solutions in polar solvents retains the extinction spectra of the separated nanodiscs over a week. On the other hand, reformation of the interacting assembly can also be induced by changing the solvent polarity. Figure 12 compares the extinction spectrum of the photoexcited TiS₂ nanodisc in deoxygenated chloroform with that obtained 20 hours after replacing the solvent with cyclohexane by precipitation and resuspension of the nanodiscs. After the resuspension of the photoexcited TiS₂ nanodiscs in cyclohexane, the peak in the extinction spectra shifted to the longer wavelength indicating the formation of the assembled structure.

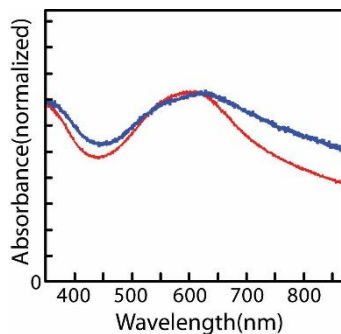


Figure 12: Reformation of the assembly of interacting $d=150$ nm TiS₂ nanodiscs by changing the solvent polarity. Red: photoexcited sample in deoxygenated chloroform. Blue: 20 hrs after the resuspension of the photoexcited TiS₂ nanodiscs in cyclohexane. The spectra are normalized to the peak intensities.

3.3 Conclusion

In summary, we showed that the optical absorption of colloidal solutions of 2-D layered TiS_2 nanodiscs of controlled diameter and thickness is strongly affected by the assemblies of strongly interacting nanodiscs present within the solution. This poses a significant challenge in studying the electronic structure of the layered transition metal dichalcogenide nanoparticles correlated with the lateral and transverse dimensions. However, efficient separation of the strongly interacting nanodiscs into non-interacting particles can be achieved by using the pulsed photoexcitation in polar solvent. The pulsed photoexcitation is considered to weaken the interparticle cohesive force and facilitate the solvation of individual particles by the solvent molecules transient modification of the charge distribution in the nanodiscs. The ability to optically modify the interparticle interaction will be useful not only for the reliable optical characterization of the colloidal layered transition metal dichalcogenide nanoparticles but also for controlling the assembly of the interacting TMDC nanoparticles with light.

3.4 Experimental Details

3.4.1 Photoinduced Separation of Nanodiscs

Photoinduced separation of the assembly of TiS₂ nanodiscs was studied using *cw* and pulsed laser light at 800 nm produced from Ti:Sapphire oscillator and amplifier (KMLabs) respectively, which are resonant with a higher-energy interband transition in TiS₂ above the band gap. The colloidal TiS₂ nanodisc solution (3ml) dispersed in thoroughly deoxygenated solvent was constantly stirred during the photoexcitation in a quartz cuvette. The average intensities of both *cw* and pulsed laser light at 800 nm were kept at 1.4W/cm². The pulse width and the repetition rate of the pulsed laser light was ~100 fs and 3kHz respectively. 405 nm *cw* diode laser (CrystaLaser) was also used to examine the wavelength dependence of the photoinduced separation of TiS₂ nanodiscs. The extinction spectra of TiS₂ nanodisc solutions were taken with Hitachi U-4100 UV/Vis/NIR spectrophotometer or CCD-based UV-Vis spectrometer from Ocean optics (USB4000). Dynamic light scattering (DLS) from the colloidal TiS₂ nanodisc solution was measured to examine the change in the effective hydrodynamic diameter of the particles due to photoexcitation and ultrasonication. For this purpose, a DLS system (Brookhaven Instruments Co.) equipped with a digital autocorrelator was used in conjunction with Ar ion laser (514.5 nm) as the light source. Since the distribution of the hydrodynamic diameter was estimated using the model assuming the spherical shape of particles, the values of the hydrodynamic diameter do not accurately represent the diameter or thickness of TiS₂ nanodisc and should be interpreted on qualitative bases.

CHAPTER IV

ORIENTATIONAL CONTROL OF COLLOIDAL 2D LAYERED TRANSITION METAL DICHALCOGENIDE NANODISCS VIA UNUSUAL ELECTROKINETIC RESPONSE*

4.1 Introduction

Single and few-layer transition metal dichalcogenide (TMDC) materials are attracting much attention due to their unique optical, electronic and transport properties arising from the 2-dimensional confinement within the layer combined with variable interlayer interaction.⁸⁵⁻⁸⁶ The tunable optical and electronic properties *via* control of the number of layers makes the single and few layer TMDCs particularly attractive for various optoelectronic applications.¹⁰³⁻¹⁰⁷ So far, the majority of atomically thin TMDC nanostructures have been created *via* either chemical vapor deposition (CVD) or exfoliation from the bulk. While these methods are capable of achieving fine control over the material thickness and have enabled the discovery of new properties of atomically thin TMDCs, they also have limitations in scaling up the synthesis and controlling the lateral dimension.⁸⁸⁻⁸⁹

More recently, solution phase synthetic methods capable of producing colloidal TMDC nanodiscs dispersed in liquid media with simultaneous control of both the thickness and lateral dimension have been developed.²⁴ These colloidal TMDC nanoparticles offer the unique opportunity to explore the multi-dimensional dependence of the TMDC properties, which has been

* Reprinted in part with permission from Daniel Rossi, Jae Hyo Han, Wonil Jung, Jinwoo Cheon, and Dong Hee Son. Orientational Control of Colloidal 2D-Layered Transition Metal Dichalcogenide Nanodiscs. *ACS Nano*, **2015**, 9(8), 8037-8043. Copyright 2015 by the American Chemical Society.

difficult to address with sheets and flakes from CVD and exfoliation methods. For example, one can utilize a variety of methods for manipulating the movement and assembling behavior of colloidal particles to create structures with higher order and controlled orientation. For TMDC nanodiscs with strongly anisotropic optical and transport properties, the capability to control their orientation will be particularly useful to exploit their anisotropic material properties.¹⁰⁸⁻¹⁰⁹

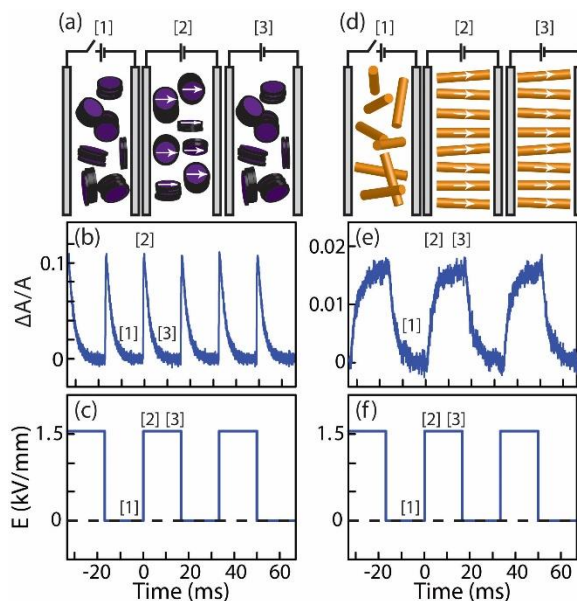


Figure 13: (a,d) Illustration of the random and oriented states of the colloidal nanoparticles under the square wave electric field for (a) TiS₂ nanodiscs and (d) CdS nanorods. [1],[2],[3] indicates low, step edge and high state of the electric field respectively. (b,e) Electrooptic response of (b) TiS₂ nanodiscs in cyclohexane and (e) CdS nanorods in tetradecane to the square wave electric field shown in (c) and (f) respectively. $\Delta A/A$ is the fractional change in the absorbance measured with linearly polarized light representing the presence of the orientational order.

One strategy to achieve orientational control is to apply an external electric or magnetic field which creates an anisotropic potential energy landscape allowing particle alignment through the interaction between the particles' magnetic/electric dipole and the applied field.^{30, 33} For instance, the alignment of semiconducting and metallic rods to a preferential direction has been

achieved *via* interaction of the electric field with the permanent dipole or anisotropic induced dipole.^{31-33, 110} For the group of layered TMDC materials possessing inversion symmetry, one would generally anticipate a relatively weak permanent dipole, which is less desirable for electric field-induced control of the orientation. On the other hand, the anisotropic 2D crystal structure may produce a large anisotropy of the induced dipole, which can potentially be utilized to align the TMDC nanodiscs even in the absence of a sufficiently large permanent dipole. Contrary to our expectation, we observed the complete absence of orientational order in several different colloidal TMDC nanodiscs under \sim kV/mm DC electric fields which can readily align 1-dimensional CdS nanorods with permanent dipoles. This suggests that neither the permanent dipole nor the anisotropic induced dipole of these nanodiscs is sufficiently large to create an orientational order in response to the applied DC electric field. However, the unexpected transient alignment of the colloidal TMDC nanodiscs created by the time-variation of the electric field, such as at the step edges of the square wave field, was observed as shown in Figure 13 (a,b,c). This behavior is in distinct contrast to the typical response of the anisotropic colloidal nanoparticles to the electric field, such as in CdS nanorods shown in Figure 13 (d, e, f), where the sustaining orientational order is created during the field-on period and randomizes *via* rotational relaxation during the field-off period.

In this study, we investigated the unusual transient electrokinetic response of the colloidal TMDC nanodiscs using linear dichroism to probe the orientational order under various time-varying electric fields. We also showed that near-steady state orientational order can be obtained from high frequency AC fields, despite the lack of usual interactions between the nanoparticle dipole and the DC electric field giving rise to the typical electric field-induced ordering of colloidal nanoparticles. The capability to create a sustaining orientational order, even in the absence of

sufficiently a strong permanent dipole or anisotropic induced dipole, opens a new alternative route to control the orientation of the colloidal TMDC nanodiscs. Utilizing the near-steady state orientational order created under the AC field, we demonstrate the capability to control the surface orientation of the TMDC nanodiscs deposited on a solid substrate and measured the orientation-dependent optical spectra of the surface-deposited samples. The observation made in this study adds a valuable strategy to control the orientation of the colloidal TMDC nanocrystals, allowing the exploration of their highly anisotropic properties.

4.2 Results and Discussion

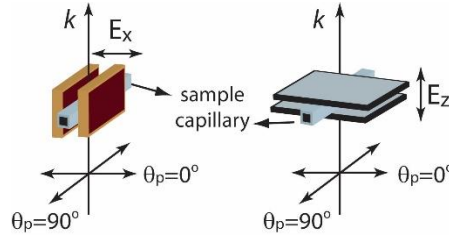


Figure 14: Electrode configurations for the electric field perpendicular (E_x) and parallel (E_z) to the light propagation direction (k). The glass sample capillary was sandwiched between the two electrodes. The polarization of light (θ_p) is defined with respect to the direction of E_x field.

In this study, the electric field-induced orientation of three different colloidal layered TMDC nanodisc (TiS_2 , WSe_2 and ZrS_2) samples were investigated by measuring the electrooptic response probing the linear dichroism of the interband transition.^{97, 111} Since the interband transition in various TMDC materials is considered to be strongly in-plane polarized, linear dichroism can readily detect changes in orientational order. Figure 14 shows two different configurations of the parallel electrodes, which were used to apply a spatially homogenous electric field perpendicular (E_x) and parallel (E_z) to the propagation direction (k) of the light. The polarization angle (θ_p) of light, controlled by a polarizer, was defined with respect to the direction of the E_x field. The details of the measurement and sample preparation are described in the Methods section. Since the electrooptic responses from all three samples are similar, we focus our discussion on TiS_2 nanodiscs, which have the more uniform size distribution and stronger absorption in the visible spectral range for ease of measurement. The electrooptic response from the other two nanodisc samples can be found in reference 35.

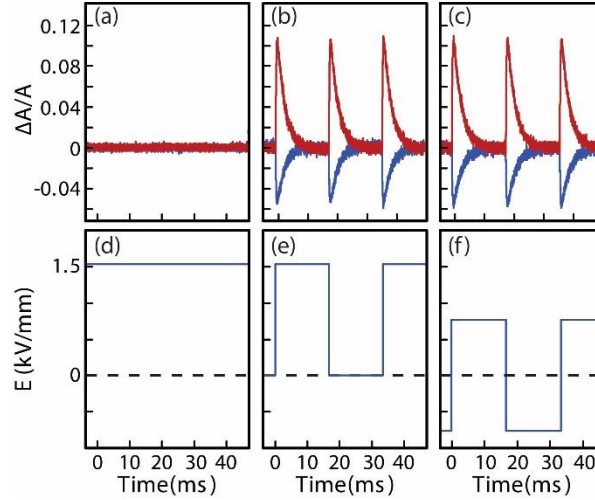


Figure 15: $\Delta A/A$ of TiS_2 nanodisc under (a) DC and (b,c) square wave E_x electric field. Polarization angle of light is $\theta_p=0^\circ$ (red) and $\theta_p=90^\circ$ (blue). (d,e,f) Time variation of the DC and square wave electric field corresponding to panels (a,b,c) respectively.

Figure 15 (a, b, c) shows the fractional changes in the absorption ($\Delta A/A$) from TiS_2 nanodiscs dispersed in cyclohexane under the DC and square wave E_x electric fields relative to the no-field condition. The red and blue curves were obtained with $\theta_p=0^\circ$ and 90° polarization, respectively. The electric field time-profiles corresponding to each data are shown in Figure 15 (d, e, f). Under the DC electric field (Figure 15a), there is no steady-state change in the absorption spectra for either polarization, indicating the absence of any orientational order. In contrast, a strong linear dichroism is observed at both the rising and falling edge of the applied square wave field, as shown in Figure 15 (b, c). Interestingly, the dichroism at the field edges decays on a few ms time scale even when the field is sustained. Furthermore, the comparisons shown in Figure 15 (b, c) indicate that the magnitude of the dichroism is independent of the DC field offset and dependent only on the step height (ΔE) at the field edges, as discussed in detail below. While the typical electric field-induced dichroism in colloidal particles reflects the orientational order, the

origin of the transient dichroism observed in TiS₂ nanodiscs should be more carefully examined considering its unusual behavior. When the dichroism reflects the orientational order, it should exhibit a well-defined dependence on the relative direction of the light polarization with respect to the direction of preferred particle orientation.³⁴ This is because the absorption (A) of the spheroids depends on the angle (γ) between the light polarization and the major axis of the spheroid as $A = A_{\parallel} \cos^2 \gamma + A_{\perp} \sin^2 \gamma$, where A_{\parallel} and A_{\perp} are the absorption parallel and perpendicular to the major axis, respectively.¹¹²

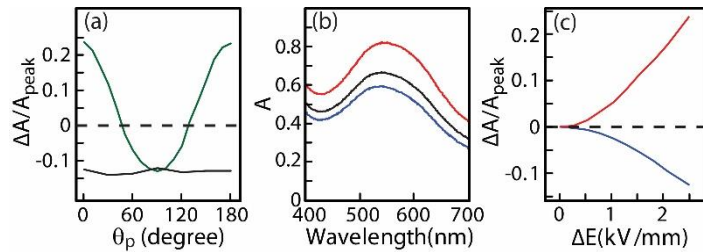


Figure 16: (a) Polarization angle (θ_p) dependence of $\Delta A/A_{\text{peak}}$ under the square wave E_x (green) and E_z (black) electric field. $\Delta A/A_{\text{peak}}$ is the peak value of the fractional change in the absorbance from the square wave electric field. (b) The absorption spectra of TiS₂ nanodiscs under square wave E_x field with $\Delta E = 2.5$ kV/mm for $\theta_p = 0^\circ$ (red) and $\theta_p = 90^\circ$ (blue) polarization. Black curve is the isotropic absorption spectrum taken without electric field. (c) ΔE dependence of $\Delta A/A_{\text{peak}}$ under square wave E_x field for $\theta_p = 0^\circ$ (red) and $\theta_p = 90^\circ$ (blue) polarization.

In order to confirm that the observed dichroism in TiS₂ nanodiscs reflects the orientational order, $\Delta A/A$ was measured as a function of the polarization angle under both E_x and E_z electric field. Figure 16a shows the peak value of the fractional change in the absorbance ($\Delta A/A_{\text{peak}}$) from TiS₂ nanodiscs as a function of the polarization angle (θ_p) under square wave E_x (green) and E_z (black) electric fields. For both electric fields, the step height at the field edge (ΔE) was ~ 2.5 kV/mm. $\Delta A/A_{\text{peak}}$ under the E_x electric field can be fit to $a \cos^2 \theta_p + b$ and the ratio of $\Delta A/A_{\text{peak}}$ at

$\theta_p=0^\circ$ and 90° is $-(2:1)$. $\Delta A/A_{\text{peak}}$ is zero near the magic angle ($\theta_p=54.7^\circ$) where the absorption is equivalent to that of the randomly oriented nanodiscs. Under the E_z electric field, $\Delta A/A_{\text{peak}}$ is independent of the polarization angle and its magnitude is close to $\Delta A/A_{\text{peak}}$ at $\theta_p=90^\circ$ under E_x electric field. The $\cos^2\theta_p$ dependence of $\Delta A/A_{\text{peak}}$ under the E_x electric field is indicative of optically anisotropic particles with orientational order. This indicates that the observed dichroism of the TiS_2 nanodiscs originates from the electric field-induced alignment, despite its unusual transient nature and independence on the fields DC amplitude. Since the absorption is strongly in-plane polarized, the positive and negative sign of $\Delta A/A_{\text{peak}}$ for $\theta_p=0^\circ$ and 90° polarization under the E_x field in Figure 16a indicates that the TiS_2 nanodiscs align with the in-plane axis parallel to the applied electric field, as illustrated in Figure 13a.^{97, 106, 113} Taking advantage of the transient orientational order created at the edges of the square wave field, we were also able to obtain the anisotropic absorption spectra in the visible spectral range using a pulsed light source synchronized to the edges of the square wave electric field. Figure 16b compares the anisotropic absorption spectra taken at $\theta_p=0^\circ$ (red) and 90° (blue) under the E_x square wave field with $\Delta E = \sim 2.5$ kV/mm. The isotropic absorption spectrum (black) taken in the absence of the field is also shown. The lineshapes of the two spectra at $\theta_p=0^\circ$ and 90° are similar, which is consistent with the dominant contribution from the in-plane transitions to the overall absorption of TiS_2 nanodiscs. On the other hand the spectrum for $\theta_p=90^\circ$ is slightly blue-shifted with respect to $\theta_p=0^\circ$ as will be further discussed later.

As shown in Figure 15, the magnitude of the dichroism from the transient orientational order depends only on the step height (ΔE) at the edges of the square wave field, not on the absolute amplitude of the DC field. To examine the correlation between ΔE and the magnitude of the

transient orientational order, $\Delta A/A_{\text{peak}}$ was measured as a function of ΔE under the E_x square wave field for $\theta_p=0^\circ$ (red) and 90° (blue) light polarizations (Figure 16c). The magnitude of $|\Delta A/A_{\text{peak}}|$ increases with increasing ΔE and the dependence is superlinear at relatively small values of ΔE for both light polarizations. Interestingly, the dependence of $\Delta A/A_{\text{peak}}$ on ΔE in TiS_2 nanodiscs is similar to typical E-dependence of the electrooptic response from colloidal particles with permanent dipole or anisotropic induced dipoles.^{34, 110, 114} This observation indicates that the change in field amplitude (ΔE) is the key parameter that determines the magnitude of the electric field-induced orientational order in colloidal TiS_2 nanodiscs. To examine the effect of varying the field sweep rate (dE/dt) for a given ΔE on the orientational order, $\Delta A/A$ was measured under trapezoidal E_x electric fields of varying slopes at the rising and falling edges for $\theta_p=0^\circ$ polarization, as shown in Figure 17a. For each trapezoidal field shown in Figure 17b, $\Delta A/A$ increases continuously during the entire period of the time-varying electric field at both the rising and falling edges of the field. On the other hand, with decreasing field sweep rate (dE/dt) at the edges of the trapezoidal field, the peak of $\Delta A/A$ also decreases. This reflects the strong competition between the rise and decay of the orientational order, where the dynamics of the rise of the orientational order varies with dE/dt while that of decay is determined by the orientational relaxation of the nanodiscs.

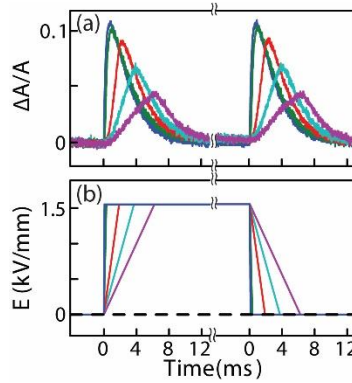


Figure 17: (a) $\Delta A/A$ of TiS_2 nanodiscs measured with $\theta_p=0^\circ$ polarization under trapezoidal E_x fields with varying slopes at the edges, (b) Time-profile of the applied E_x electric field.

The absence of dichroism under the DC electric field in TiS_2 nanodiscs studied here indicates that neither the permanent dipole nor the anisotropy of the induced dipole is sufficiently large to create an orientational order against thermal randomization. Instead, a transient orientational order created by the time-varying electric field is required to explain the observations. One possible explanation is the alignment of the nanodiscs by a transient magnetic field induced by the time-varying electric field. However, this possibility is carefully ruled out since TiS_2 nanodiscs are diamagnetic according to SQUID measurement, which can be found in reference 35. One may also suspect the creation of a transient magnetic field by the current generated in the nanodiscs if there are sufficient free electrons available, which may result in the transient rotational response. We ruled out this possibility as well since the same transient orientational order was observed not only in low-bandgap semiconducting or semimetallic TiS_2 but also in semiconducting WSe_2 and ZrS_2 , with much higher bandgaps, having negligible free electron density in conduction band. When electrolytes are present in the solvent, an ionic double layer created at the interface between the material and solvent can create torques and forces in response to an electric field, such as electro-rotation and electro-osmotic effect.¹¹⁵⁻¹¹⁷ In some cases, the ionic double layer

introduces transient features in the electrokinetic response of the particles in aqueous solution.¹¹⁴,¹¹⁸ However, such possibility is also ruled out since there are no electrolytes or ionizable molecules present in the solvent medium used in this study, furthermore the sample showed negligible charging current which would be present in the case of ionic double layer formation. The potential influence from spatial gradients in the electric field which may exist near the corners of the sample capillary is also ruled out from the comparison of the electrooptic response measured in sample capillaries of different sizes. In addition, the 'normal' electric field-induced dichroism of CdS nanorods observed under the identical experimental setup, as shown in Figure 13d-f, further supports that the transient electrokinetic response of TiS₂ nanodiscs is a unique material property of the colloidal TMDC nanodiscs studied here.

One possible explanation for the transient orientational order is the time-varying anisotropy of the induced dipole originating from the anisotropic dielectric relaxation under a time-varying electric field. Because of the large difference in the intralayer (covalent) and interlayer (van der Waals) bonding character, the relaxation rate of the interfacial polarization (Maxwell-Wagner-Sillars polarization) that depends on the dielectric function and conductivity of the particle and surrounding medium may be significantly distinct in different directions.¹¹⁹⁻¹²¹ The anisotropic relaxation rate of this interfacial polarization may create a 'time-varying' anisotropy of the induced dipole at the step edges of the field. If the anisotropy of the induced dipole is the largest at the field edges and continues to decay afterwards, transient orientational order can be created. However, the mechanism for the creation of the transient orientational order by the 'time-variation' of the electric field, not the DC amplitude of the field, is still not well-understood. Further studies will be necessary to gain a better understanding of the microscopic origin of the observed phenomena, which is beyond the scope of this study.

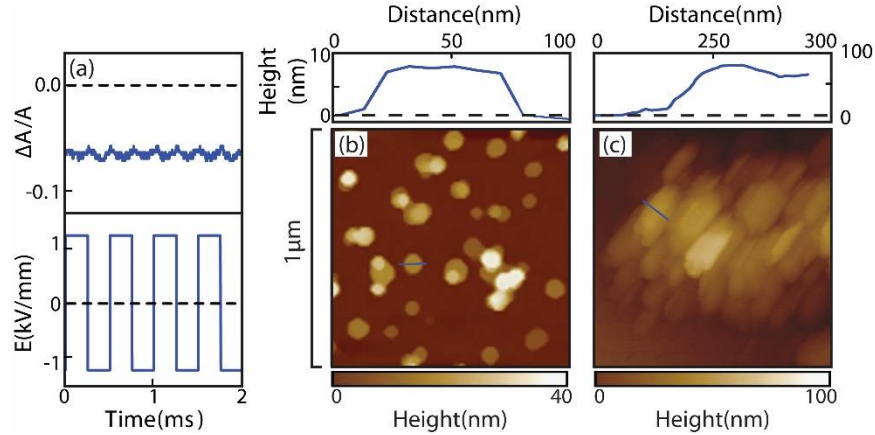


Figure 18: (a) $\Delta A/A$ under E_z square wave electric field at 2 kHz showing the near-steady state orientational order. (b, c) AFM images of TiS_2 nanodiscs deposited on the microscope cover slip in the absence (b) and the presence (c) of the 2kHz square wave E_z field. The average diameter and thickness of the nanodiscs are 60 nm and 7 nm respectively.

Nevertheless, the observed unusual transient orientational order created by the time-varying electric field in this study offers a unique insight into the new strategy for controlling the orientation of the colloidal TMDC nanoparticles that are not responsive to the DC electric field. The large disparity in the rise and decay time scales of the orientational order under the square wave field suggests that a near-steady state orientational order may be obtained by applying an AC square wave electric field at frequencies higher than the decay rate of the orientational order. Figure 18a shows the electrooptic response ($\Delta A/A$) from TiS_2 nanodiscs under the E_z square wave field at 2kHz, indicating that the sustaining orientational order can be obtained despite the absence of the response to DC field. To demonstrate the utility of the near-steady state orientational order in creating the TMDC nanostructures with controlled orientation, we compared the surface orientation of TiS_2 nanodiscs on a glass substrate deposited *via* drop-casting with and without kHz square wave electric field. Figure 18b shows the AFM image of TiS_2 nanodiscs on a glass substrate deposited in the absence of the applied electric field. Due to the large surface area of the basal

planes of TiS_2 nanodiscs interacting with the substrate, the nanodiscs prefer to lie flat on the surface as either individual or stacked discs. The line profile measured across a chosen nanodisc well represents the average diameter ($\sim 60\text{nm}$) and thickness ($\sim 7\text{ nm}$) of the nanodiscs. The statistics of the measured diameter and thickness can be found in the reference 35. On the other hand, application of the AC square wave field at 2kHz perpendicular to the substrate produces near-steady state orientational order and facilitates the nanodiscs to proceed to the vertical surface orientation during the deposition as shown in Figure 18c. The height of the structure estimated from the line profile is similar to the diameter of the nanodiscs, consistent with the vertical orientation of the nanodiscs. Meanwhile, the lateral dimensions of the nanodisc assembly are significantly larger than the height and thickness of a single nanodisc. This is due to the formation of assemblies of vertically-oriented nanodiscs extended in both directions on the surface of the substrate.

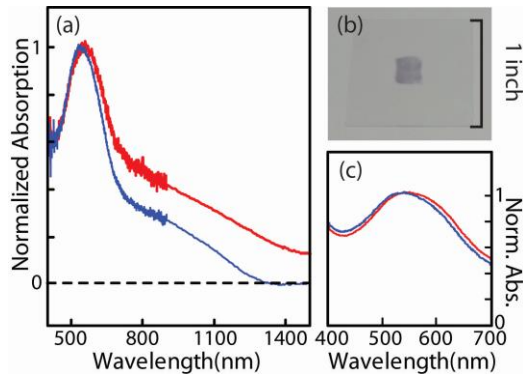


Figure 19: (a) Normalized absorption spectra of the surface-deposited samples, where TiS_2 nanodiscs were deposited on the microscope coverslip with (blue) and without (red) the applied AC square wave electric field. (b) Photograph of the microscope coverslip with the deposited TiS_2 nanodiscs. (c) Normalized comparison of the solution-phase absorption spectra for $\theta_p=0^\circ$ (red) and $\theta_p=90^\circ$ (blue) under E_x field originally shown in Figure 16b.

To examine whether the anisotropic material properties from the orientation-controlled TiS₂ films can be obtained on a macroscopic scale, we measured the absorption spectra of TiS₂ films deposited with and without an AC square wave field over a large area. Figure 19a compares the normalized absorption spectra of the two TiS₂ film samples deposited on the microscope coverslip with (blue) and without (red) AC square wave field measured over the area of *ca.* 5x5 mm². Figure 19b shows the photograph of the sample substrate used for the absorption measurement. In Figure 19a, the film deposited with the external electric field exhibits a significantly reduced near-infrared absorption at >700 nm compared to the film deposited without the field. This difference was reproducibly observed over multiple trials of sample preparation and measurement. The decrease in the near infrared absorption is consistent with the reduction of the in-plane component of the optical transition in the film containing TiS₂ nanodiscs standing perpendicular to the surface compared to the case where TiS₂ nanodiscs are lying flat.^{42,97} A small shift of the absorption peak in the visible spectral region in Figure 19a is also observed in the normalized comparison of the solution-phase absorption spectra for $\theta_p=0^\circ$ and $\theta_p=90^\circ$ under the E_x field shown in Figure 19c. Since the solution-phase spectra for $\theta_p=0^\circ$ and $\theta_p=90^\circ$ probe more in-plane and out-of-plane optical transition component respectively than the spectrum of the randomly orientated nanodiscs, the direction of the peak shift observed in film samples is consistent with that in solution phase. Considering that other colloidal TMDC nanodiscs (WSe₂ and ZrS₂) exhibit similar transient electrokinetic response as TiS₂, the same method can be applicable to a wide range of TMDC materials that will be particularly useful in studying their anisotropic material properties, such as the anisotropic optical and interfacial charge transfer properties.

4.3 Conclusion

In summary, we observed the unusual electric field-induced alignment of colloidal TMDC nanodiscs, where the orientational order was created only transiently by the time-variation of the electric field, while no orientational order can be established by the DC electric field. The linear dichroism signal probing the orientational order under the square wave field is equivalent to performing an edge detection of the electric field and its magnitude is dependent on the step height at the field edges, but on the amplitude of the field. This contrasts to the typical response of anisotropic colloidal nanocrystals to the electric field, where the permanent dipole or anisotropic induced dipole results in a sustaining orientational order under the DC field. We conjecture that the anisotropic dielectric relation in the highly anisotropic TMDC nanodiscs may create a time-varying anisotropy of the induced dipole, resulting in the transient rotational order. Nevertheless, a near-steady state orientational order could be created using an AC square wave field at frequencies higher than the orientational relaxation rate of the nanodiscs. We also showed that the near-steady state orientational order from the AC field can be utilized to control the surface orientation of the TMDC nanodiscs deposited on a solid substrate and exhibit orientation-dependent optical properties. The ability to control the orientation of the TMDC nanodiscs demonstrated in this study will be highly valuable in exploring the anisotropic material properties of the colloidal 2D layered TMDC nanocrystals.

4.4 Experimental Details

4.4.1 Measurement of Electrooptic Response

The linear dichroism of the colloidal TMDC nanodiscs resulting from the electric field-induced orientation was measured using a 10X microscope and a linearly polarized light source. The detailed construction of the experimental setup is shown in detail in reference 35. Copper plates and ITO-coated glass plates separated by 1.3 mm were used as the electrodes providing E_x and E_z field respectively as shown in Figure 14. A high-voltage amplifier (Trek 2220) or high-voltage pulse generator (DEI GRX) in combination with a function generator provided the DC or square wave voltage to the electrodes. A rectangular glass capillary with the inner dimension of 0.5 mm \times 0.5 mm (VitroCom) containing the sample solution was placed between the two electrodes. Linearly polarized light in 400-700 nm range was obtained from tungsten-halogen or pulsed xenon lamp using a thin film polarizer. The polarization angle (θ_p) of the light is defined with respect to the direction of the E_x field. A 10X microscope objective and a tube lens were used to measure the intensity of the transmitted light from the mid-section of the capillary within 0.15 mm diameter circular area using an iris placed at the focal plane of the image. Time-dependent absorption intensity and spectrum of the sample were measured with PMT and CCD spectrometer respectively.

4.4.2 Preparation of Orientation-Controlled TiS₂ Nanodisc Films

Films of TiS₂ nanodiscs deposited on the microscope cover slips were prepared using the TiS₂ nanodiscs solution described above. A drop of TiS₂ nanodisc solution was sandwiched between the two microscope cover slips cleaned *via* UV-ozone treatment. To confine the solution between the top and bottom cover slips and avoid drying of the solution during the deposition, a glass spacer with a 5 \times 5 mm² square well was inserted between the two cover slips. The cover slips

were placed between the two copper electrodes providing the square wave electric field perpendicular to the surface of the substrate for 1 hr. The cover slips were removed from the electrode, separated, and rinsed with chloroform and allowed to dry. AFM (Dimension Icon) was used in tapping mode to image the surface morphology of TiS_2 nanodiscs. The film exhibiting the flat surface orientation of TiS_2 nanodiscs was prepared with the method outlined above in the absence of the electric field. The film exhibiting the vertical surface orientation of TiS_2 nanodiscs was prepared under ~ 1.5 kV/mm square wave field at 2kHz. The visible and near infrared absorption spectra of the nanodisc films deposited on the microscope cover slip were obtained using the spectrometer equipped with Si and InGaAs detectors covering visible and near infrared spectral range respectively.

CHAPTER V

ANISOTROPIC ELECTRON-PHONON COUPLING IN COLLOIDAL LAYERED TiS_2 NANODISCS OBSERVED VIA COHERENT ACOUSTIC PHONON*

5.1 Introduction

Atomically thin layered transition metal dichalcogenides (TMDC) are attracting much interest due to their unique material properties arising from 2-dimensional structure providing in-plane confinement for the electrons and holes.⁸⁵⁻⁸⁷ Much effort has been made recently to explore various optical,^{12-13, 122} vibrational,^{6-7, 9, 123} and transport properties¹²⁴⁻¹²⁵ of TMDC materials varying with the layer thickness. Another important aspect of the properties of the layered TMDC materials is strong anisotropy. Because of the large difference in the intralayer and interlayer bonding character, the layered TMDC is expected to show anisotropic material properties. For instance, interband optical transitions in many semiconducting layered TMDC materials are considered strongly polarized in-plane.^{97, 106} The anisotropic lattice potential also introduces the anisotropy to the structure of phonon and the properties associated with it such as the thermal conductivity.^{7-8, 126-128} The strong anisotropy of the electronic structure and lattice potential in layered TMDC materials may also result in the anisotropic coupling between the electronic and lattice degrees of freedom. Since the electron-phonon coupling plays a crucial role in determining

* Reprinted in part with permission from Daniel Rossi, Luis E. Camacho-Forero, Guadalupe Ramos-Sanchez, Jae Hyo Han, Jinwoo Cheon, Perla Balbuena and Dong Hee Son. Anisotropic Electron-Phonon Coupling in Colloidal Layered TiS_2 Nanodiscs Observed Via Coherent Acoustic Phonon. *J. Phys. Chem. C*, **2015**, 119(13), 7436-7442. Copyright 2015 by the American Chemical Society.

various optical and transport properties, understanding its anisotropy is important to fully exploit unique properties of atomically thin layered TMDC materials.

Here, we report the observation of the preferential coupling of the interband optical transition with the intralayer coherent acoustic phonon mode over the interlayer mode in colloidal solutions of TiS_2 nanodiscs excited by fs laser pulses. The transient absorption signal from the diameter- and thickness-controlled TiS_2 nanodiscs exhibited an oscillatory feature, which is attributed to the modulation of the interband absorption peak by the intralayer breathing mode, while the signature of the interlayer mode was not observed. Considering the earlier studies reporting the dependence of the optical properties on the interlayer spacing¹²⁹⁻¹³⁰ and the observation of the interlayer breathing mode in Raman spectra of substrate-supported thin flakes of other layered TMDC (e.g., MoS_2),¹³¹ the apparent absence of the signature of the interlayer acoustic phonon in colloidal TiS_2 nanodiscs may seem unusual. In order to gain an insight into the anisotropic coupling of the interband optical transition and coherent lattice motion in colloidal TiS_2 nanodiscs, we performed DFT calculations of the band structure and the dielectric functions at varying lateral and transverse lattice parameters. The calculations indicate that the interband optical transition in visible spectral range is mainly polarized in-plane and the shift of the absorption peak is more sensitive to the variation of the in-plane than out-of-plane lattice parameter. This result is consistent with the observed oscillation of the absorption peak only by the intralayer breathing mode of the coherent acoustic phonon. The present study provides a useful insight into the anisotropic coupling of the coherent lattice motion and the interband transition in nanoscale TMDC materials, particularly those with simultaneous lateral and transverse spatial confinement.

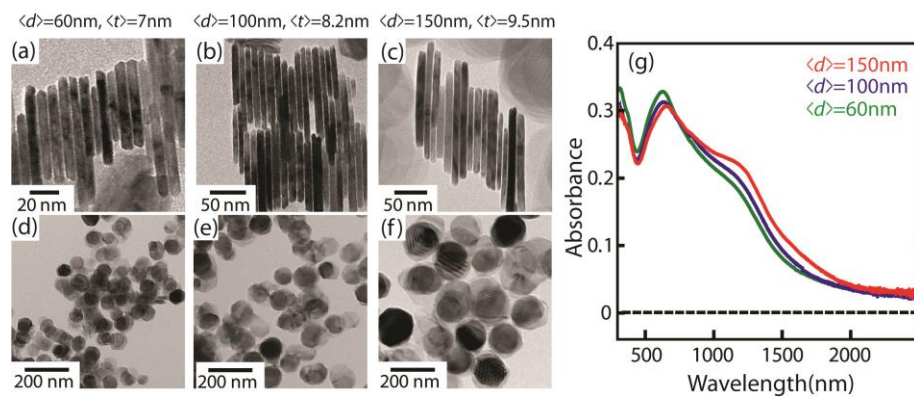


Figure 20: (a-f) TEM images and (g) optical absorption spectra of colloidal TiS_2 nanodiscs of different sizes.

5.2 Results and Discussion

We chose TiS_2 nanodiscs as the model system of the colloidal TMDC nanoparticles in this study because of the relatively well-developed synthesis method for controlling both the diameter and thickness.²⁴ Controlling the diameter and thickness of the nanodiscs is important in time-domain measurement of the size-dependent, low-frequency coherent acoustic phonon modes, which are not readily observable in the frequency-domain measurements. The different dimensional dependence of the interlayer and intralayer acoustic phonon frequency allows facile identification of the mode coupled to the optical transition from the time-domain measurement. TEM images and optical absorption spectra of the colloidal TiS_2 nanodisc samples with different diameter and thickness used in this study are shown in Figure 20. The average diameter ($\langle d \rangle$) and thickness ($\langle t \rangle$) of the TiS_2 nanodiscs are shown in each panel. The broad absorption in the visible and near-infrared region is from the higher-energy interband transition above the bandgap and exhibits a small red-shift with increasing size of the nanodiscs, which may reflect the spatial confinement effect as well as the interparticle interaction. The absorption peak near 600 nm was chosen to investigate the coupling of the optical transition with acoustic phonon in this study through the measurement of transient absorption.

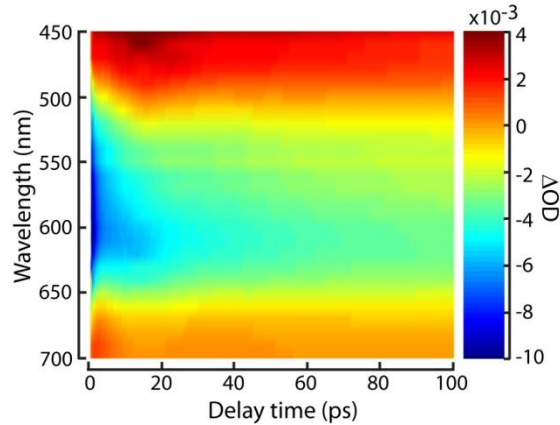


Figure 21: Color contour plot of the transient absorption spectra of colloidal TiS₂ nanodiscs.

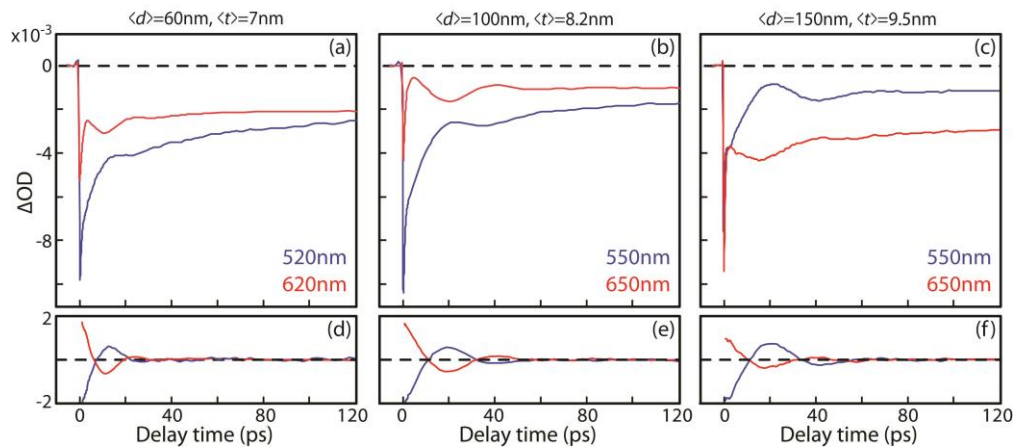


Figure 22: (a-c) Transient absorption data at two different probe wavelengths on the opposite sides of the absorption peak near 600 nm. The average diameter and thickness of the nanodiscs and the probe wavelengths are indicated in each panel. (d-f) The oscillatory component of the transient absorption signal extracted from the fitting of the data.

Figure 21 shows the color contour plot of the transient absorption spectra of one colloidal TiS₂ nanodiscs sample ($\langle d \rangle = 100 \text{ nm}$, $\langle t \rangle = 8.2 \text{ nm}$), obtained with 800 nm pump and visible probe in 450-700 nm range. The transient absorption spectra exhibit the initial bleach of the absorption centered at $\sim 600 \text{ nm}$, followed by the recovery of the bleach and the appearance of the induced absorption at both wings of the peak at early delay times. The recovery of the bleach occurs on

multiple timescales: a few ps and hundreds of ps or longer. These features are analogous to what has been observed in thin flakes of MoS₂ and reflect the relaxation of the photoexcited charge carriers and broadening of the absorption peak after the photoexcitation.^{95, 132} The other two TiS₂ nanodisc samples exhibit qualitatively similar features, while the details of the dynamics are different. Figure 22a-c show the transient absorption data of TiS₂ nanodiscs of different sizes at two chosen probe wavelengths corresponding to the left and right sides of the main absorption peak near 600 nm shown in Figure 20g. All the transient absorption data exhibit the two major features: the recovery of the bleach and the oscillatory feature superimposed on the bleach recovery. Here, we will focus on the oscillatory component of the signal that reflects the coherent lattice motion coupled to the electronic transition and will not discuss the bleach recovery component. The oscillatory features isolated from the transient absorption data are shown in Figure 22d-f. The isolated oscillatory signal is essentially a single exponentially decaying cosine function and exhibits a phase difference of nearly π at the two probe wavelengths on the opposite sides of the peak. This indicates that the energy of the absorption peak is modulated by a single dominant phonon mode coupled to the probed optical transition. Rapid dephasing of the oscillation can be ascribed to the combination of the distribution of the particle sizes and the damping of the vibration by the surrounding environment. The period of the oscillation extracted from the fitting of the transient absorption data as the sum of the multiexponential function and an exponentially decaying cosine function are summarized in Table 1.

$\langle d \rangle$ (nm)	60	100	150
$\langle t \rangle$ (nm)	7	8.2	9.5
τ_{exp} (ps)	23	40	42
τ_{intra} (ps)	18.4	30.5	46
τ_{inter} (ps)	5.8	7.0	8.1

Table 1: Experimental (τ_{exp}) and calculated periods for intralayer (τ_{intra}) and interlayer (τ_{inter}) coherent acoustic phonon of TiS₂ nanodiscs of different average diameter $\langle d \rangle$ and thickness $\langle t \rangle$.

The modulation of the optical transition energy by coherent acoustic phonon has been previously observed in many other colloidal nanostructures including semiconductor quantum dots, plasmonic metal nanoparticles and carbon nanotubes.¹³³⁻¹³⁵ Coherent phonons from the ultrashort optical excitation are usually created via displacive or (and) resonance impulsive stimulated Raman mechanism depending on the nature of the optical transition and the characteristics of the light pulse.¹³⁶⁻¹³⁷ In highly absorbing materials, impulsive heating of the lattice can also excite coherent acoustic phonon. The coherent lattice motion can in turn periodically modify the electronic structure, which is often detected as the modulation of various optical properties such as optical transition energy or intensity. The most distinct difference of the layered TiS₂ nanodiscs from the previously studied semiconductor quantum dots and plasmonic metal nanocrystals is the strongly anisotropic electronic and lattice structure, which can potentially introduce the stronger anisotropy in electron-phonon coupling. In metals with high lattice symmetry, such as gold with cubic lattice structure, both the radial and extensional breathing modes were observed to modulate the energy of the localized surface plasmon in the transient absorption signal of the nanorods upon ultrashort pulsed optical excitation of the plasmon.¹³⁸⁻¹³⁹ This indicates that the coupling of plasmon and lattice motions in metal nanorods is not selective

even when the morphology is anisotropic. In semiconductor nanocrystals, electron-phonon coupling is reported to be more anisotropic in morphologically anisotropic structures such as CdSe nanorod or CdSe platelets.¹⁴⁰⁻¹⁴² In CdSe nanorods, mainly the radial breathing mode of the acoustic phonon along the short axis was observed to modulate the exciton absorption peak.¹⁴¹

In TiS₂ nanodiscs studied here, we observed the signature of a single dominant acoustic phonon mode in the transient absorption signal at the spectral region of interband transition. In order to determine which mode is mainly responsible for the observed modulation of the interband transition energy, the dependence of the oscillation period on the dimension of the nanodiscs was calculated using a simple continuum model. For the coherent acoustic phonons in nanostructures, their periods are reasonably well predicted using the bulk material parameters such as the elastic constants and density for a known shape and size. The period of intralayer breathing mode of TiS₂ nanodisc was estimated using the following equation that models the radial breathing mode of a circular disc assuming the intralayer and interlayer modes are separated.¹⁴³

$$\tau_{\text{intra}} = \frac{2\pi R}{\lambda} \sqrt{\frac{\rho(1-\sigma^2)}{E}}$$

Here, R is the radius, E is Young's modulus, ρ is mass density, σ is Poisson's ratio and λ is a constant that depends on the order of radial breathing mode. The period of the interlayer acoustic phonon was calculated using the following equation based on the coupled oscillator model, which has been recently applied to model the interlayer breathing mode of the thin flakes of MoS₂ observed in Raman study.⁸

$$\tau_{\text{inter}} = \left(\sqrt{\frac{K}{2\mu\pi^2} \left(1 - \cos\left(\frac{\pi}{N}\right) \right)} \right)^{-1}$$

Here, K is the spring constant per unit area, μ is the mass per unit area and N is the number of layers. The periods of intralayer and interlayer breathing modes calculated from these equations are summarized in Table 1. The values of all the parameters used in this calculation are in reference 42.

Comparison of the oscillation periods in Table 1 indicates that the interband absorption peak of TiS₂ nanodiscs is modulated by the intralayer mode rather than interlayer mode since τ_{exp} is much closer to τ_{intra} than to τ_{inter} . While there is a difference between τ_{exp} and the calculated τ_{intra} , likely due to the distribution of nanodisc diameter, variation of the shape and the effect of the surrounding medium, the assignment to the intralayer mode can be reliably made. The observation of only the intralayer mode in this study can be interpreted as the result of one or both of the followings: (i) preferential excitation of the intralayer acoustic phonon during the fs optical excitation, (ii) higher sensitivity of the interband absorption peak to in-plane than out-of-plane lattice motion. However, the absence of the signature of the interlayer mode may seem somewhat unusual considering the earlier observation of the effect of varying interlayer spacing on the optical properties in other related layered TMDC materials.¹²⁹⁻¹³⁰ In the case of exfoliated MoS₂ sheets with large lateral dimension ($\sim 10\mu\text{m}$) supported on a substrate, Raman study observed the interlayer breathing mode, suggesting the possibility of exciting the interlayer breathing mode in colloidal TiS₂ nanodiscs.¹³¹ In addition, coherent phonon modulating the pump-probe absorption or reflection intensity in exfoliated MoS₂ sheets was also reported, which was attributed to the out-of-plane standing stress wave or interlayer shear and breathing mode.¹⁴⁴⁻¹⁴⁵ However, these studies in the large-area exfoliated MoS₂ sheets did not observe the signature of the intralayer breathing mode, in contrast to the colloidal TiS₂ nanodiscs in this study, perhaps due to the large and irregular lateral dimension of the sheets. Unlike in exfoliated sheets, colloidal TiS₂ nanodiscs have

sufficiently small and controlled lateral and transverse dimensions, which allows the detection of both intralayer and interlayer coherent acoustic phonon, if they are sufficiently coupled to the probed optical transition.

In order to obtain a further insight into the anisotropic coupling between the interband optical transition and coherent acoustic phonon observed in TiS₂ nanodiscs, optical anisotropy and the anisotropic dependence of the optical absorption spectra on the lattice parameters were examined from electronic structure calculation. For this purpose, density functional theory (DFT) calculations of the electronic band structure and dielectric functions were performed on the bulk TiS₂ with varying in-plane and out-of-plane strains that model the lattice motions from the intralayer and interlayer coherent acoustic phonon. While the calculations on the bulk TiS₂ structure do not describe the spatial confinement effect on the electronic structure of the TiS₂ nanodiscs, they still capture the key features of the optical anisotropy and the anisotropic dependence of the optical absorption spectra on the lattice strain. The details of the calculations are described in the experimental section.

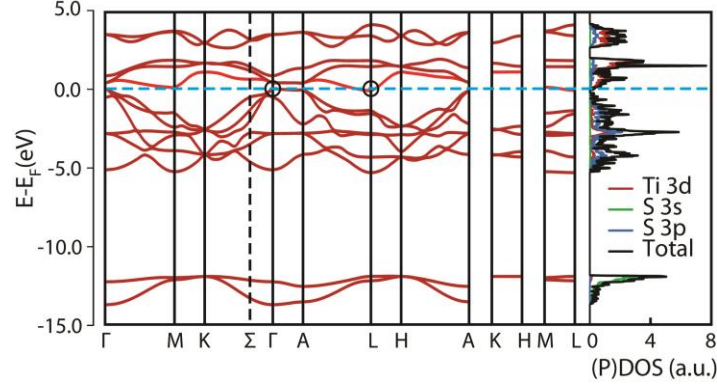


Figure 23: Electronic band structure along high-symmetry directions (left) and DOS (right) of TiS_2 at optimized lattice parameter (strain-free system). Dashed blue line stands for the Fermi-level, which is set to be 0 eV. Black circles indicate points in the reciprocal lattice at which the indirect overlap is shown. The vertical dashed line indicates a point between K- and Γ -point (Σ -point), where the VBM is located for expansions above 0.1 \AA (See reference 42)

We first calculated the electronic band structures of the strain-free TiS_2 . Figure 23 shows the calculated band structure, and total and partial density of states (DOS) of the strain-free bulk TiS_2 . Analysis of DOS shows two bands between -13.6 and -11.8 eV that are composed mainly of S 3s states. Between -5.3 and -0.2 eV below the Fermi level (E_F), there are six bands that are mostly occupied by S 3p states, while five bands can be recognized above E_F , where Ti 3d orbitals are mainly present. The valence and conduction bands are essentially occupied by hybridized orbitals of Ti 3d and S 3p. A small indirect overlap of 0.09 eV is found between the valence band maximum (VBM) at the Γ -point and the conduction band minimum (CBM) at the L-point in the reciprocal lattice, which is in agreement with previous reports.^{102, 146-147} According to this calculation, TiS_2 exhibits a non-zero DOS at E_F , nevertheless, this DOS is small indicating that this material behaves as a semi-metal, although semiconductor states for this material have been found as well.^{148,149} Electronic band structures of TiS_2 with in-plane (Δa) and out-of-plane (Δc) strain in the range between -0.2 \AA and 0.3 \AA are compiled in reference 42. When in-plane strain was applied, the metal-

like behavior strengthened as the compression increased, while the opening of an indirect bandgap enhancing the semiconductor-like behavior was observed with increasing tensile strain. On the other hand, the electronic band structure was significantly less sensitive to the out-of-plane strain than to the in-plane strain, revealing the anisotropic dependence of the electronic structure on the lattice strain.

The complex dielectric functions ($\epsilon_1 + i\epsilon_2$) were also calculated for the strain-free and strained TiS₂. The components of the complex dielectric spectra parallel (ϵ_{\parallel}) and perpendicular (ϵ_{\perp}) to the *c*-axis of TiS₂ in 0-3 eV energy range are summarized in reference 42. For the strain-free system, ϵ_{\parallel} and ϵ_{\perp} show a large difference in their intensities and the imaginary part of ϵ_{\perp} ($\epsilon_{2\perp}$) is dominant in the dielectric spectra and mainly responsible for the observed optical transition in the visible and near infrared region. The calculated dielectric functions were used to compute the imaginary part of the refractive index (*k*) representing the optical absorption intensity using the equation $k^2 = \frac{1}{2}(\sqrt{\epsilon_1^2 + \epsilon_2^2} - \epsilon_1)$.

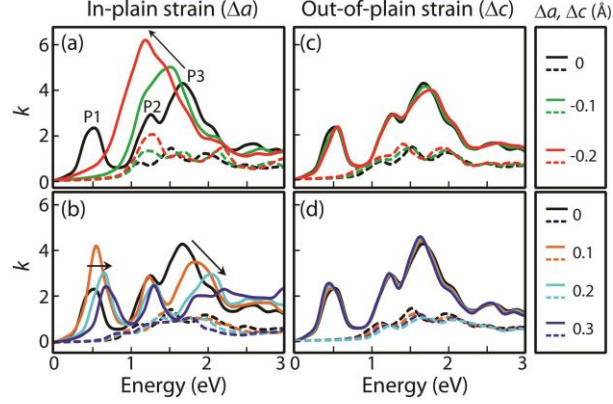


Figure 24: Imaginary part of refractive index (k) under varying degrees of lattice strain. k_{\perp} and k_{\parallel} are shown as solid and dashed lines respectively. (a,b) In-plane compressive and tensile strain respectively. Arrows indicate the direction of the peak shift of with increasing strain. (c,d) Out-of-plane compressive and tensile strain respectively. Δa and Δc are relative to the strain-free lattice parameters of $a=3.410 \text{ \AA}$ and $c=6.064 \text{ \AA}$ respectively.

Figure 24a,b show the components of k perpendicular (k_{\perp} , solid lines) and parallel (k_{\parallel} , dashed lines) to the c -axis of TiS_2 with in-plane compressive and tensile strain respectively. Figure 24c,d show the same quantities in TiS_2 with out-of-plane strain. For comparison, k_{\perp} and k_{\parallel} of the strain-free TiS_2 are also shown in each panel (Black curves). In strain-free TiS_2 , k_{\perp} is significantly larger than k_{\parallel} reflecting the dominant contribution of the in-plane polarization component in the optical absorption spectra as expected from the dielectric spectra discussed above. Since k_{\perp} has the major contribution to the absorption spectra, we will focus on k_{\perp} in discussing the effect of the lattice strain on the optical properties unless stated otherwise. In strain-free structure, three major peaks are present in k_{\perp} at 0.55, 1.24 and 1.66 eV, each indicated as **P1**, **P2** and **P3** respectively. For in-plane compressive strain (Figure 24a), **P3** that carries the largest intensity is significantly *red-shifted* as the strain increases. Besides, the three major peaks merge into one peak with a higher intensity with increasing lattice compression. For in-plane tensile strain (Figure 24b), **P1** and **P3** are *blue-shifted* as the lattice expansion increases, whereas no clear trend

is observed in **P2**. It is also noted that the intensity of **P3** become weaker with increasing in-plane tensile strain. In contrast to the cases of in-plane strain, out-of-plane strain leads to insignificant variations of the peak position and intensity for both k_{\perp} and k_{\parallel} (Figure 24c,d). This result suggests that the optical absorption spectrum is more significantly affected by the intralayer rather than by the interlayer mode of coherent acoustic phonon if their amplitudes are comparable.

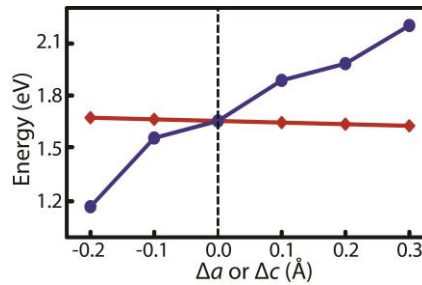


Figure 25: Dependence of the peak position of **P3** in k_{\perp} on in-plane (blue, Δa) and out-of-plane (red, Δc) lattice strain. Δa and Δc are relative to the strain-free lattice parameters of $a = 3.410 \text{ \AA}$ and $c = 6.064 \text{ \AA}$ respectively.

In order to make a more quantitative comparison of the sensitivity of the peak energy of the optical absorption to the in-plane and out-of-plane strain, we pay a particular attention to **P3** that carries the largest intensity in k_{\perp} . Figure 25 compares the peak shift of **P3** resulting from the changes in in-plane (Δa) and out-of-plane (Δc) lattice parameters from their equilibrium values. Significant peak shift is observed from in-plane strain, whereas only a slight shift is observed from out-of-plane strain, illustrating the strong anisotropy in the shift of the optical absorption peak in response to the change in the lattice parameters. The above result indicates that the intralayer mode of the coherent acoustic phonon is more likely to modulate the energy of the optical transition than the interlayer mode supporting our experimental observation.

5.3 Conclusion

We observed the preferential coupling of the interband optical transition with the intralayer coherent acoustic phonon mode over the interlayer mode in colloidal solution of TiS_2 nanodiscs, which illustrates anisotropic electron-phonon coupling in colloidal multi-layered TiS_2 nanodiscs. The transient absorption signal from the diameter and thickness-controlled TiS_2 nanodiscs exhibited an oscillatory feature, which is attributed to the modulation of the interband absorption peak energy by the intralayer breathing mode. On the other hand, the signature of the interlayer mode was not observed, while excitation of interlayer coherent phonon was previously observed in other non-colloidal exfoliated sheets of related TMDC materials. Additional insight into the anisotropic coupling of coherent phonon with interband optical transition was obtained from DFT calculations of the optical absorption spectra of TiS_2 as a function of the in-plane and out-of-plane strain. The calculations indicate that the interband optical transition has much higher sensitivity to the in-plane strain than to the out-of-plane strain, consistent with the observation of the dominant signature of intralayer acoustic phonon mode in the transient absorption.

5.4 Experimental details

5.4.1 DFT Calculations

The calculations were performed using the Vienna *ab Initio* Simulation Package (VASP),¹⁵⁰⁻¹⁵² employing the projector-augmented wave (PAW) pseudopotentials¹⁵³⁻¹⁵⁴ as provided in the VASP databases, to describe the electron-ion interactions. The *3p4s3d* and *3s3p* states of Ti and S atoms respectively were included in the pseudopotentials as the valence states. The exchange-correlation functional was treated within the Perdew-Burke-Ernzerhof generalized gradient approximations (GGA-PBE)¹⁵⁵. Spin polarization was included in all calculations. The energy cut-off for the plane-wave basis expansion was chosen to be 500 eV. A conjugate-gradient algorithm was used to relax the ions into their instantaneous ground state. A Gaussian smearing with a width of 0.02 eV was employed. For the Brillouin zone integration, a 9×9×5 Monkhorst-Pack¹⁵⁶ k-point mesh was used, whereas for density of states (DOS) calculations a 15×15×11 k-point mesh was employed. The convergence criteria for electronic self-consistent iteration and ionic relaxation were set to 10⁻⁴ and 10⁻³ eV, respectively. We are aware that DFT-GGA calculations normally lead to underestimation of the absolute band gap energy of materials. However, relative variations of the electronic properties using DFT-GGA are in accordance with other techniques that are known to yield results closer to experimental values, such as: DFT employing hybrid functional (HSE06) or Quasi-particle approximations (GW)^{126, 157-158}. In this work DFT-PBE is used to compare the dependence of electronic and optical properties with respect to variations of the lattice constants.

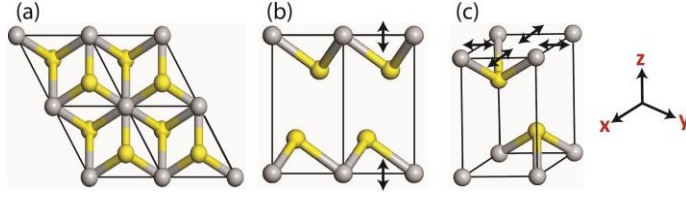


Figure 26: (a) Top and (b) side view of a portion of the TiS_2 structure. Gray and yellow spheres represent Ti and S atoms, respectively. (b,c) Arrows show the direction of the out-of-plane and in-plane strain

In this work, the experimental TiS_2 bulk structure was used as initial configuration and then relaxed allowing atomic positions, cell size, and shape to change. Subsequently, strains along both the x- and y-directions (in-plane strain, Figure 26c.) and along the z-direction (out-of-plane strain, Figure 26b) were introduced to examine the effect intralayer and interlayer coherent acoustic phonon on the optical absorption spectrum. The frequency dependent dielectric function, $\epsilon(\omega) = \epsilon_1(\omega) + i\epsilon_2(\omega)$, was computed using the independent-particle approximation as implemented within VASP.¹⁵⁹ 128 bands were used for calculation of the optical properties. Due to the hexagonal symmetry of TiS_2 , there are two independent components $\epsilon_{\parallel} = \epsilon_{zz}$ and $\epsilon_{\perp} = \epsilon_{xx} = \epsilon_{yy}$ that are parallel and perpendicular to the c-axis respectively.

CHAPTER VI

CARRIER DYNAMICS AND INTERFACIAL ELECTRON TRANSFER DYNAMICS IN TiS_2 AND $\text{TiS}_2/\text{TiO}_2$ TYPE II HETEROSTRUCTURED NANODISCS

6.1 Introduction

Heterostructured semiconductor nanocrystals with type-II heterointerface are desirable for photocatalytic and photovoltaic application due to their ability to spatially separate the photoexcited charge carriers.^{46, 160-161} The spatially separated charge carriers can facilitate redox chemistry at the particle surface and enhance photocurrent generation by suppressing the recombination of the charge carriers within the nanocrystals. Often, one component of the type-II heterostructure functions as the primary absorber of photons producing the electrons and holes and the subsequent interfacial electron transfer separates them spatially. Numerous methods have been developed to produce type-II heterostructured semiconductor nanocrystals capable of separating charge carriers effectively, such as the direct epitaxial growth of the heterostructure, chemical transformation to heterostructure via partial ion exchange, and chemical linking of the presynthesized nanocrystals.¹⁶²⁻¹⁶⁵ Among the semiconductor heterostructured nanocrystals, those containing TiO_2 have been explored extensively although TiO_2 itself is not a strong light absorber in the visible spectral region due to its high bandgap. This is because TiO_2 can readily form type-II band alignment with broad range of semiconductor materials that can harvest light in solar spectrum and support long lifetime of the separated charge carriers. For this reason, much effort has been made to create heterostructured nanocrystals of TiO_2 and light-harvesting semiconductor materials.¹⁶⁶ For an efficient interfacial charge transfer, making a direct contact between the two materials is more desirable than using the molecular linkers. However, the formation of such heterostructure is generally not a trivial task especially when the difference in the lattice parameters

between the two materials is large. The successful examples of type-II heterostructured nanocrystals making a direct contact with TiO_2 are CdSe/TiO_2 and PbS/TiO_2 heterostructured nanocrystals.^{164, 167-168} These nanocrystals showed their capability to separate the visible- or near infrared-excited charge carriers via efficient interfacial electron transfer, and demonstrated their ability to enhance the photocatalytic H_2 production and generation of photocurrent in an electrochemical cell.

In this study, we created type-II nanocrystals between TiS_2 and TiO_2 capable of separating the photoexcited charge carriers, which take advantage of very strong absorption of visible and near infrared light and facile formation of directly contacting heterointerface via controlled partial oxidation of TiS_2 nanocrystals. Compared to Cd and Pb chalcogenides nanocrystals of the same volume, TiS_2 with the 2-dimensional layered structure exhibits an order of magnitude stronger light absorption due to the band nesting also observed in many other layered transition metal chalcogenides such as MoX_2 and WX_2 ($\text{X}=\text{S}, \text{Se}$).¹⁶⁹⁻¹⁷⁰ Since both components of the heterostructure contain Ti, controlled partial oxidation of TiS_2 nanocrystals could form the heterostructure relatively straightforwardly.²⁴ Partial oxidation of TiS_2 to TiO_2 phase was achieved by chemical or photochemical process, which creates amorphous or crystalline phase of TiO_2 directly on top of TiS_2 nanodiscs. Here, we studied the effect of forming $\text{TiS}_2/\text{TiO}_2$ heterointerface on the relaxation dynamics of the photoinduced charge carriers in TiS_2 under visible and near infrared excitation conditions employing pump-probe transient absorption spectroscopy. The rapid interfacial electron transfer upon the photoexcitation was observed in both chemically and photochemically produced $\text{TiS}_2/\text{TiO}_2$ nanocrystals, each containing amorphous and crystalline (rutile) phase of TiO_2 , despite the relatively fast nonradiative relaxation in the photoexcited TiS_2 nanodiscs.

6.2 Results and Discussion

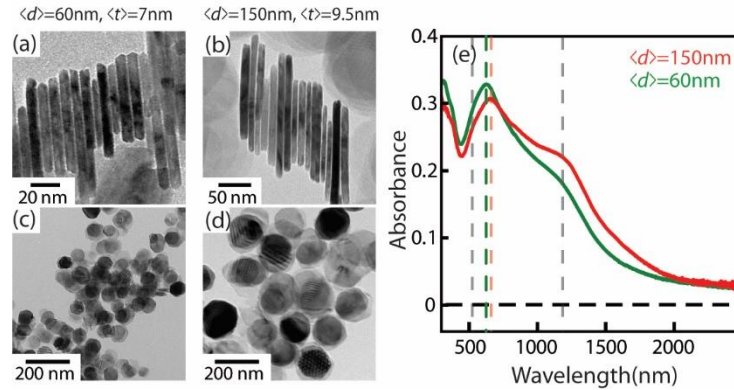


Figure 27: Side and top view TEM images of TiS₂ nanodiscs with $\langle d \rangle = 60$ nm (a,c), and $\langle d \rangle = 150$ nm (b,d). Absorption spectra of $\langle d \rangle = 60$ nm and $\langle d \rangle = 150$ nm TiS₂ nanodiscs with the relevant transitions marked as dashed vertical lines.

Figure 27 shows the absorption spectra and TEM images from $\langle d \rangle = 60$ nm and $\langle d \rangle = 150$ nm TiS₂ nanodiscs. The average thickness for each sample is listed along with the TEM images. With the decrease in particle diameter, the aspect ratio nearly doubles, making it difficult to isolate the effects of lateral confinement. Regardless the absorption spectra shows sensitivity to the size in both the position and ratio of absorption feature intensities. Three features are marked on the absorption spectra by the vertical dashed lines, one nIR (A3) and two visible interband absorptions (high energy A1 and low energy A2). A description of these transitions can be made from comparison with the electronic structure calculations in chapter III. The conduction band edge is dominated by Ti 3d orbitals with relatively weak dispersion (1 eV > bandwidth), while the valence band is a mixture of Ti 3d, and S 3s/3p orbitals with much stronger dispersion (~2.5 eV bandwidth). The A1 transition can likely be identified as direct transitions between S 3s and Ti 3d orbitals in

the Γ -A region, while A1 and A2 are likely from M-M, K-K, and L-L corresponding to transitions from a mixture of Ti 3d /S 3p to Ti 3d orbitals.

Comparison of the the absorption spectra for the two different sized TiS_2 nanodiscs, figure 27e, shows the A3 feature to be more sensitive to the change in particle size than the A1 or A2. As discussed extensively in chapter III, due to the anisotropy of the chemical bonding, the absorption spectra for layered materials, which is described by the imaginary part of the dielectric function, can be decomposed into two components k_{\perp} and k_{\parallel} corresponding to the in-plane and out-of-plane components. The A1 and A3 transition are dominated by k_{\perp} , while the A2 transition was a mixture of k_{\perp} and k_{\parallel} . From the comparison of the absorption spectra, only the A2 transition appears to show any strong dependence on the size of the nanodisc, suggesting that states with both k_{\perp} and k_{\parallel} absorption components are more sensitive to particle size.

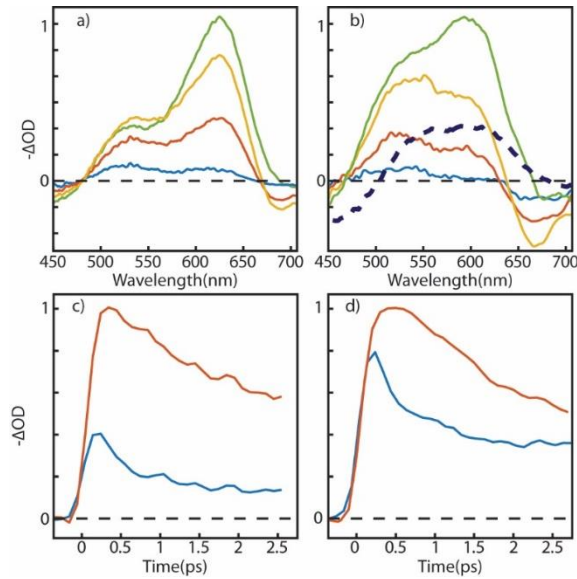


Figure 28: Short time pump probe spectra and dynamics for $\langle d \rangle = 150$ (a,c), and $\langle d \rangle = 50\text{ nm}$ (b,d) TiS_2 nanodiscs. The black dashed line represents the long time dynamic spectra taken at $\sim 2\text{ ns}$.

Considering the relative difference in diameter and thickness between the two samples are $\sim 60\%$ and $\sim 20\%$ respectively, the changes to the absorption spectra should more strongly represent features involving k_{\parallel} . This is observed in the absorption spectra as the shift and increase in relative contribution of the A1 absorption feature, while the A1 and A3 features are relatively unchanged. Pump probe spectroscopy was used to study the nature of these transitions in more detail. Figure 28 a-d show the early time spectra and dynamics for both $\langle d \rangle = 50\text{nm}$ (a,c) and $\langle d \rangle = 150\text{nm}$ (b,d) pumped with 800nm and probed in the visible. The signal is dominated by the direct one photon absorption as will be made clear later. Under 800nm excitation, the visible transitions cannot be directly populated, so bleaching of these transitions is related either to either the indirect filling of band edge states after excitation or reduced oscillator strength due from multicarrier interactions.

The bleach of interband transitions from multicarrier effects can likely be ruled out as these interactions are generally accompanied by peak shifting which is not observed here. Since the state filling of band edge states in the visible requires electron or holes to populate the states at M, K, or Γ , and since direct excitation is not possible at these points, intervalley scattering or either electrons or holes must be invoked. Intervalley scattering is a phonon activated process whereby electrons/holes can move throughout the conduction/valence band via absorption or emission of phonons, meaning the barrier between two energy minimum must not exceed the excess available carrier energy, in this case kT . Since the dispersion of the valence band is likely too large for holes to move via phonon assistance, photo-generated holes are likely localized between Γ and A. On the other hand the small dispersion of the conduction band is consistent with the thermalization of electrons across the band edge, suggesting that the short time dynamics under 800nm excitation can give information regarding the thermalization of electron populations. The timescale for the formation of A1 and A2 similar, however A1 has a rapid decay component during the A2 rise time,

perhaps suggesting the transient population of states at in the conduction band as they continue to relax to A2. The slow growth of the A2 feature may represent the buildup of carriers during the thermalization process, while the initial fast decay of A2 may reflect multicarrier recombination or charge carrier trapping processes as will be discussed in detail later. Interestingly in the long decay limit, black dashed line, the contribution from both transitions is roughly equal. The decay of these features into one peak can possibly be interpreted as the localization of electrons to a single energy state, possibly a trap state or a single band edge state.

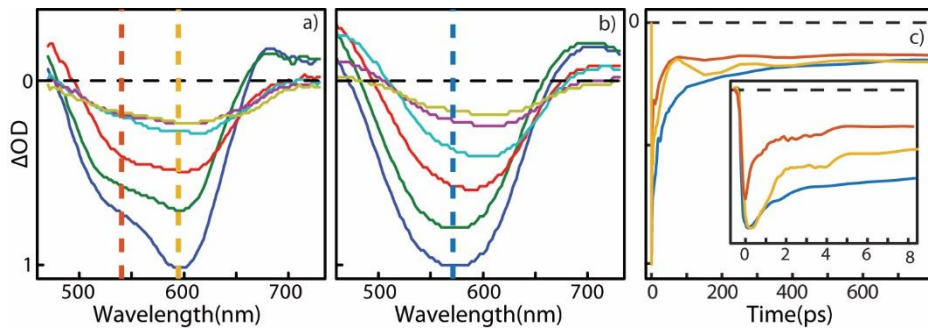


Figure 29: Comparison of bleach dynamics of 60nm TiS₂ naondiscs under 800nm (a), and 400nm (b) excitation.

Figure 29 a and b show the bleach spectra under 400nm and 800nm excitation. The two discrete peaks previously discussed as A1 and A2 are not discernable when pumped with 400nm, and only a single broad feature is observed in the visible which is dramatically broadened in short time and narrows/red-shifts as it decays. The difference in spectral shape is likely described by either the direct population (both electrons and holes) of states not accessible by 800nm pump, or the relaxation of higher energy electrons into these states, for example at the L point in the conduction band. The general features of the time dependent spectral evolution are similar under

both excitation, the bleach decay and spectral narrowing. This is common behavior in bulk systems where excitation density is high and strong many body interactions can severely broaden the spectra in the early time dynamics. Regardless of the exact nature of the bleach under 400nm excitation, holes will still likely localize between Γ and A and the state filling induced bleach of the visible transition will require electron populations at the conduction band edge. Using this interpretation, we are confident that under both excitation conditions the dynamics in the visible represent electron populations.

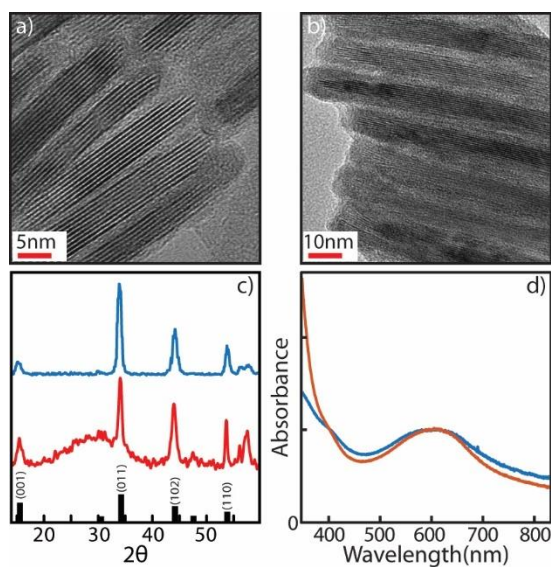


Figure 30: (a,b) TEM images of (a) TiS_2 nanodiscs and (b) $\text{TiS}_2/\text{TiO}_2$ heterostructured nanodiscs produced from partial chemical oxidation of TiS_2 nanodiscs. (c) X-ray diffraction patterns of TiS_2 (blue) and $\text{TiS}_2/\text{TiO}_2$ (red) nanodiscs. (d) Absorption spectra of TiS_2 (blue) and $\text{TiS}_2/\text{TiO}_2$ (red) nanodiscs.

Fig. 30a,b shows TEM images of TiS_2 nanodiscs and $\text{TiS}_2/\text{TiO}_2$ heterostructured nanodisc created from partial chemical oxidation of TiS_2 nanodiscs. The chemical oxidation converts the outer part of TiS_2 nanodiscs to amorphous TiO_2 surrounding the inner TiS_2 nanodisc in the

heterostructure, in contrast to the photochemical oxidation and other higher-temperature synthesis which form crystalline TiO₂. In order to have the similar size of TiS₂ component in both TiS₂ and TiS₂/TiO₂ nanodiscs (~60nm in diameter and ~7 nm in thickness), slightly larger TiS₂ nanodiscs were used to obtain TiS₂/TiO₂ nanodiscs via partial oxidation. Fig. 1c compares the X-ray diffraction patterns of TiS₂ and TiS₂/TiO₂ nanodiscs, where the broad peak centered at 2θ=30° is attributed to the amorphous TiO₂. The optical absorption spectra of TiS₂ and TiS₂/TiO₂ nanodisc compared in Fig. 1d show the relative increase of the absorption at <400nm after the partial oxidation, capturing the tail of the TiO₂ band edge absorption. On the other hand, the location of the absorption peak near 600 nm, which depends on the size of TiS₂ component, are similar in both TiS₂ and TiS₂/TiO₂ nanodiscs supporting the similar size of TiS₂ component in both samples. The broad absorption peak centered at 600 nm is attributed to the multiple direct interband transitions which we previously described in great detail.¹⁷¹ As discussed above, we believe the relaxation dynamics of the visible transitions mainly represent the population of electrons, making it possible to use these interband transitions to study electron transfer dynamics. In addition to the strong direct interband absorption in the visible region, the absorption from TiS₂ extends to near IR region, which is attributed to smaller direct and indirect bandgap of TiS₂.¹⁷² The approximate absorption cross section at 600 nm calculated from the volume of the nanodisc obtained from the TEM images and concentration of the particles from the elemental analysis is 3.03 x 10⁸ for TiS₂ nanodiscs shown in Fig. 1a, which is nearly an order of magnitude larger than II-VI quantum dots when compared at the same volume.¹⁷³ While the initially formed amorphous TiO₂ can be converted to the crystalline form upon thermal annealing in solution phase, in order to maintain better colloidal stability we did not anneal the nanodiscs and examined the interfacial electron transfer from TiS₂ to amorphous TiO₂. Although the conduction band edge of amorphous TiO₂ is

between that of rutile and anatase TiO₂, amorphous TiO₂ is typically not used for photocatalytic systems due to the faster charge carrier recombination rates relative to crystalline TiO₂.¹⁷⁴ However, this is not an issue in systems such as ours where the electron and hole are spatially separated. For example, amorphous TiO₂ was recently used to enhance electron transfer in dye sensitized solar cells by acting as an electron accepting material.¹⁷⁵

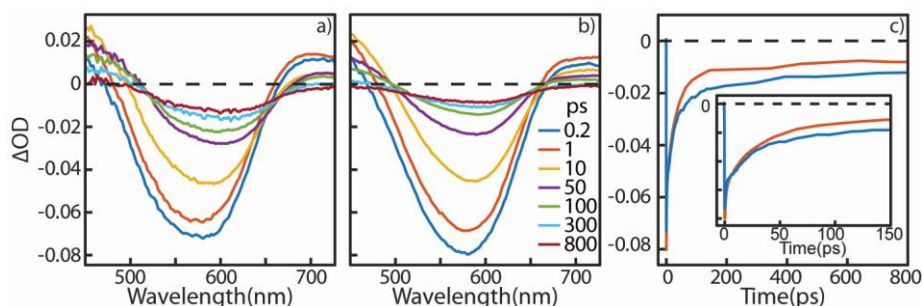


Figure 31: (a,b) Transient absorption spectra for 60nm TiS₂ nanodiscs (a), and TiS₂/TiO₂ heterostructure nanodiscs (b) excited at 400 nm. (c) Transient absorption probed at the peak of bleach (580 nm) for TiS₂ nanodiscs (blue) and TiS₂/TiO₂ heterostructure nanodiscs (red) Pump probe relaxation dynamics probed for 60nm (blue) and TiS₂/TiO₂ heterostructure nanodiscs (red) excited at 400 nm and probed at the wavelength of maximum bleach (~580nm).

Pump λ	Sample	τ_1 (ps)	τ_2 (ps)	τ_3 (ps)	a_1	a_2	a_3
400nm	TiS ₂	1.3	43.7	5000	-0.27	-0.53	-0.21
	TiS ₂ /TiO ₂	1.23	37.5	5000	-0.31	-0.60	-0.11
800nm	TiS ₂	1.25	36.0	5000	-0.49	-0.31	-0.20
	TiS ₂ /TiO ₂	1.02	37.5	5000	-0.77	-0.33	-0.05

Table 2: Multi-exponential fit parameters of transient absorption data probed at the peak of the bleach. The time constant for the slow recovery component (τ_3) was fixed at 5ns.

Fig. 31 a,b show the transient absorption spectra of TiS₂ nanodiscs and chemically oxidized TiS₂/TiO₂ nanodiscs respectively in visible spectral region under 400 nm excitation. Both spectra show strong bleach of the interband absorption near 600 nm after the excitation that recovers on multiple time scales, otherwise the general properties of the bleach dynamics under 400nm excitation were discussed above.¹⁷⁶ Fig. 31c compares the transient absorption data of TiS₂ (blue) and TiS₂/TiO₂ (red) nanodiscs at the peak wavelength of the bleach (580 nm). The overall dynamic features reflected in the transient absorption data are qualitative similar, exhibiting the initial rapid recovery of the bleach in ~40 ps followed by much slower phase of the recovery on >ns time scale. Table 2 summarizes the multi-exponential fit of the transient absorption kinetics at the peak wavelength of the bleach. Since the slow component of the bleach recovery occurs much more slowly than the time window of the measurement (~1ns), its time constant (τ_3) was fixed at 5ns in the fitting. The time constants for the fast recovery component (τ_1 and τ_2) are slightly shorter for TiS₂/TiO₂ compared to TiS₂ alone. A more significant difference is observed in the amplitude of the slow recovery component (a_3), where TiS₂/TiO₂ exhibits the smaller amplitude. The slow recovery of the bleach occurring on ns time scale in many semiconductor nanocrystals has been often interpreted as the result of the trapping of the charge carriers slowing down their recombination.¹⁷⁷⁻¹⁷⁸ The interpretation that the bleach of the visible interband transition monitors the population of electrons at the band edge would suggest that rapid decay corresponds to the electron trapping, while the slower decay corresponds to the slow relaxation of electrons due to trapped holes. As the dynamics are rather complex and still not fully understood, we are hesitant to interpret any changes to the timescale as a results of electron transfer dynamics. However, under the assumption that the oxidation does not appreciably affect the total population of trapped charge

carriers, the decreased amplitude of a_3 in TiS₂/TiO₂ compared to TiS₂ indicates the decrease band edge electron population, likely via interfacial electron transfer from TiS₂ to TiO₂.

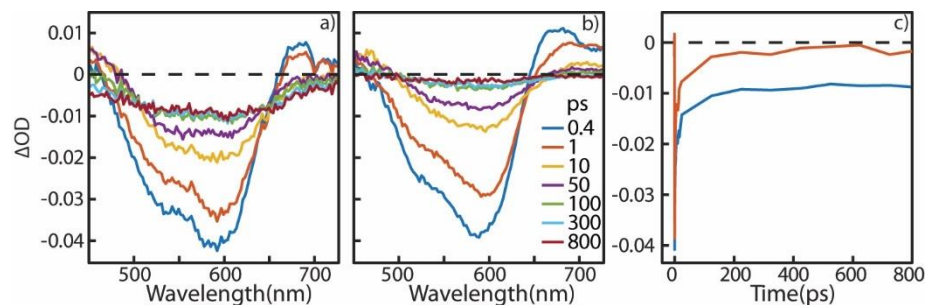


Figure 32: (a,b) Transient absorption spectra for 60nm TiS₂ nanodiscs (a), and TiS₂/TiO₂ heterostructure nanodiscs (b) excited at 800 nm. (c) Transient absorption probed at the peak of bleach (580 nm) for TiS₂ nanodiscs (blue) and TiS₂/TiO₂ heterostructure nanodiscs (red)

As mentioned earlier, strong and broad light absorption from UV to near IR spectral regions is one of the potential benefits of 2-dimensional layered TiS₂ nanodiscs as the light harvesting material. For such broad absorption to be useful for photoinduced chemical processes in TiS₂/TiO₂ heterostructured nanodiscs, electrons produced from the absorption of the near IR photons should also be able to transfer across the heterointerface. To examine such possibility, the transient absorption spectra of TiS₂ and TiS₂/TiO₂ nanodiscs under 800 nm excitation were compared. Fig. 32 a,b show the transient absorption spectra of TiS₂ and TiS₂/TiO₂ nanodiscs in visible spectral region that exhibit the bleach and recovery of the interband absorption near 600 nm under 800 nm excitation. Fig. 32c compares the transient absorption data at the peak wavelength of the bleach (580 nm). The multi-exponential fit of the data is also shown in Table 2. As discussed above the spectral shape are different between the 400nm and 800nm pump probe data, however the dynamics are qualitatively similar: rapid recovery in ~40 ps and slow recovery on >ns time scale.

The amplitude of the slow bleach recovery component (a_3) is smaller in TiS₂/TiO₂ than in TiS₂ nanodiscs, same as under 400 nm excitation. We take this to mean that the interfacial electron transfer from TiS₂ to TiO₂ can occur with both 400 and 800 nm excitations, suggesting the possibility of harvesting near IR photons to create the charge carriers that can take advantage of the type-II heterointerface to induce the photochemical process.

If one takes the amplitude $a_{3\text{TiS}_2}/a_{3\text{hs}}$ (hs refers to heterostructure) as the relative population of electrons transferred to TiO₂ under a given excitation condition, it is interesting that the electron transfer is more efficient under 800nm pump. This result could suggest that 400nm and 800nm excitation produce different populations of electrons, some of which are more useful for electron transfer. As mentioned above, the major differences in the bleach spectra can be explained by the population of different states under 400nm or 800nm excitation. Further evidence of this can be extracted from the timescales of relaxation. Under 800nm the two observed bleach feature relax on different time scales, in fact it appears that the high energy bleach feeds into the low energy bleach, a commonly observed phenomena in other systems probing the filling of band edge states. Under 400nm only a single peak appears, at a position in between the two peaks observed in the 800nm data, possibly a distinct transition. While the short time dynamics are different, it is difficult to extract meaning from them as under 400nm excitation electrons are excited into high energy conduction band levels and relaxation mechanisms exist that do not in the 800nm pump data. Interestingly the long time dynamics are identical as observed in figure 29c, which is expected as it represents slow recombination of electrons due to trapped holes. Were the occupied states under both excitation conditions equal with respect to electron transfer rates the ratio $a_{3\text{TiS}_2}/a_{3\text{hs}}$ would be similar, however $a_{3\text{TiS}_2}/a_{3\text{hs}}$ is roughly twice larger under 800nm excitation. This could potentially be related to the strong anisotropy of the structure promoting electron transfer from states polarized

more strongly out of plain than in plain, however this is only speculation. Regardless this does suggest that a third transition which was difficult to identify in the absorption spectra exists which will be important for future study of the TiS_2 nanodisc.

6.3 Conclusion

We monitored the relaxation dynamics in TiS_2 and $\text{TiS}_2/\text{TiO}_2$ heterostructure nanodiscs to characterize the TiS_2 to TiO_2 electron transfer. Semiconductor/ TiO_2 heterostructures are commonly studied for applications such as visible light drive H_2 production, and TiS_2 is a highly efficient visible/nIR light absorber with an absorption cross-section two orders of magnitude larger than other semiconductors commonly used in such heterostructures. The TiS_2 nanodiscs in this study could be partial oxidized to form $\text{TiS}_2/\text{TiO}_2$ heterostructures via chemical oxidation forming TiS_2 nanodiscs with an outer shell of TiO_2 . Using transient absorption, we observed a strong bleach of the visible interband electronic transitions under both 400nm and 800nm excitation for both TiS_2 and $\text{TiS}_2/\text{TiO}_2$ nanodiscs. We observed the faster relaxation of the interband transitions for in the heterostructure nanodiscs which we attribute to TiS_2 to TiO_2 electron transfer. Furthermore the signature of electron transfer was observed under both 400nm and 800nm excitation indicating the possibility to use visible and nIR excitation to achieve charge separation.

CHAPTER VII

EXCITON INDUCED TURNING ON OF DARK STATES IN CsPbBr₃ QUANTUM DOTS

7.1 Introduction

Semiconducting lead halide perovskite nanomaterial with intense photoluminescence (PL), facile chemical tuning of PL energy, and long carrier diffusion lengths are extensively studied as next generation materials for photonic and photovoltaic applications.¹⁷⁹ In particular, all inorganic colloidal nanocrystals of cesium lead halide (CsPbX₃) have attracted much attention as a potentially superior source of photons and charge carriers in various applications. Due to the challenges related to the synthesis of CsPbX₃ QDs with sufficient control of size and morphology in the strongly confined regime, most research has focused on large sized CsPbX₃ exhibiting only weak confinement effects.¹⁷⁹ For this reason, the photophysical properties expected from the confined exciton which can differ significantly from the non-confined counterpart remain unstudied. As the confinement of exciton is known to introduce unique properties resulting from the stronger interactions between exciton and other degrees of freedom on the surface and within the QD volume this topic which merits investigation.⁶⁰

Recently, the synthesis of strongly confined CsPbX₃ QDs with high ensemble uniformity of the size and morphology was achieved, removing one of the obstacles in the exploration of the properties of confined exciton in CsPbX₃ QDs. Taking advantage this synthetic progress, we observed strong and well-defined exciton-induced absorption peak in transient absorption spectra of CsPbBr₃ QDs located between the two lowest exciton transitions QDs that we ascribed to the formally forbidden exciton transition. The decay of the exciton-induced absorption shows the identical dynamics to the recovery of the bandedge exciton bleach in the QDs, while its buildup is slower than the buildup of the bandedge exciton bleach. In addition, such dynamic spectral feature

becomes less distinct and muted in the larger non-confined CsPbBr₃ nanocrystals, suggesting that the confinement-enhancement in giving the oscillator strength to the forbidden transition. Generally, absorption from the formally forbidden transition in QDs requires the perturbation, such as the symmetry breaking, sufficiently large to relax the optical selection rule. However, the majority of the colloidal QDs do not exhibit the strong exciton-induced absorption from the formally forbidden transition. While the increase of the intensity of the forbidden transition due to symmetry breaking by exciton or hot carriers was reported in PbS and PbSe QDs, its magnitude was relatively weak or short-lived.^{70, 180} We conjecture that strong coupling of charge carriers with lattice in lead halide perovskites that are known to readily form the polarons may create transient symmetry breaking in the QDs responsible for the unusually strong exciton-induced absorption in CsPbBr₃ QDs.

7.2 Results and Discussion

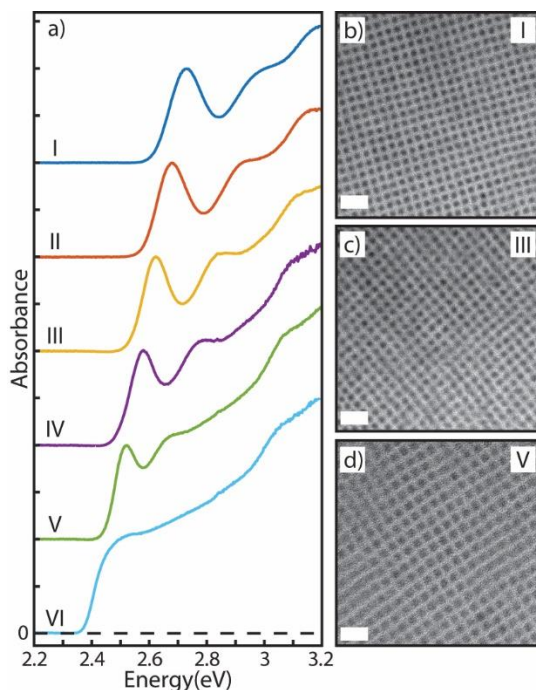


Figure 33: (a) Absorption spectra from CsPbBr₃ quantum dots with decreasing size. b-d) TEM images from samples I, III, and V, scale bars are 20nm.

Figure 33 shows a series of absorption spectra from ($L = 3.7\text{nm}$ to $L > 10\text{nm}$) CsPbBr₃ quantum dots, as well as TEM images from three representative samples spanning the size range studied. Samples I-V were prepared with recently refined synthetic protocol providing more monodispersed samples with better size control, while sample VI was prepared using the standard synthetic conditions for CsPbBr₃ nanoparticles. The broad featureless absorption spectra from sample VI is consistent with most recent works on CsPbBr₃ nanoparticles, and is indicative of the poorly monodispersed samples observed in the corresponding TEM image. The absorption spectra from samples I-V show distinct band edge exciton features, as well as higher energy exciton peaks, which blueshift with decreasing particle size from the exciton confinement. Compared with

confined samples obtained via size selective precipitation, the sharp exciton features are more well defined due to high monodispersity achieved with the refined synthesis, typically producing size distributions of less than $\pm 5\%$. The energy of the first two exciton absorption features (E_1 and E_2) from samples I-V and the band edge absorption from the VI are listed in table I.

eV	I	II	III	IV	V	VI
E_1	2.73	2.68	2.62	2.57	2.51	2.43
E_2	3.00	2.95	2.86	2.79	2.67	---
E_{IA}	2.88	2.83	2.76	2.71	2.60	---

Table 3: Energy of the first two exciton absorption features (E_1 and E_2) extracted from fitting of absorption spectra in figure 1, as well as the induced absorption energy (E_{IA}) extracted from the 10ps transient absorption spectra figure 2 (f-j red curves).

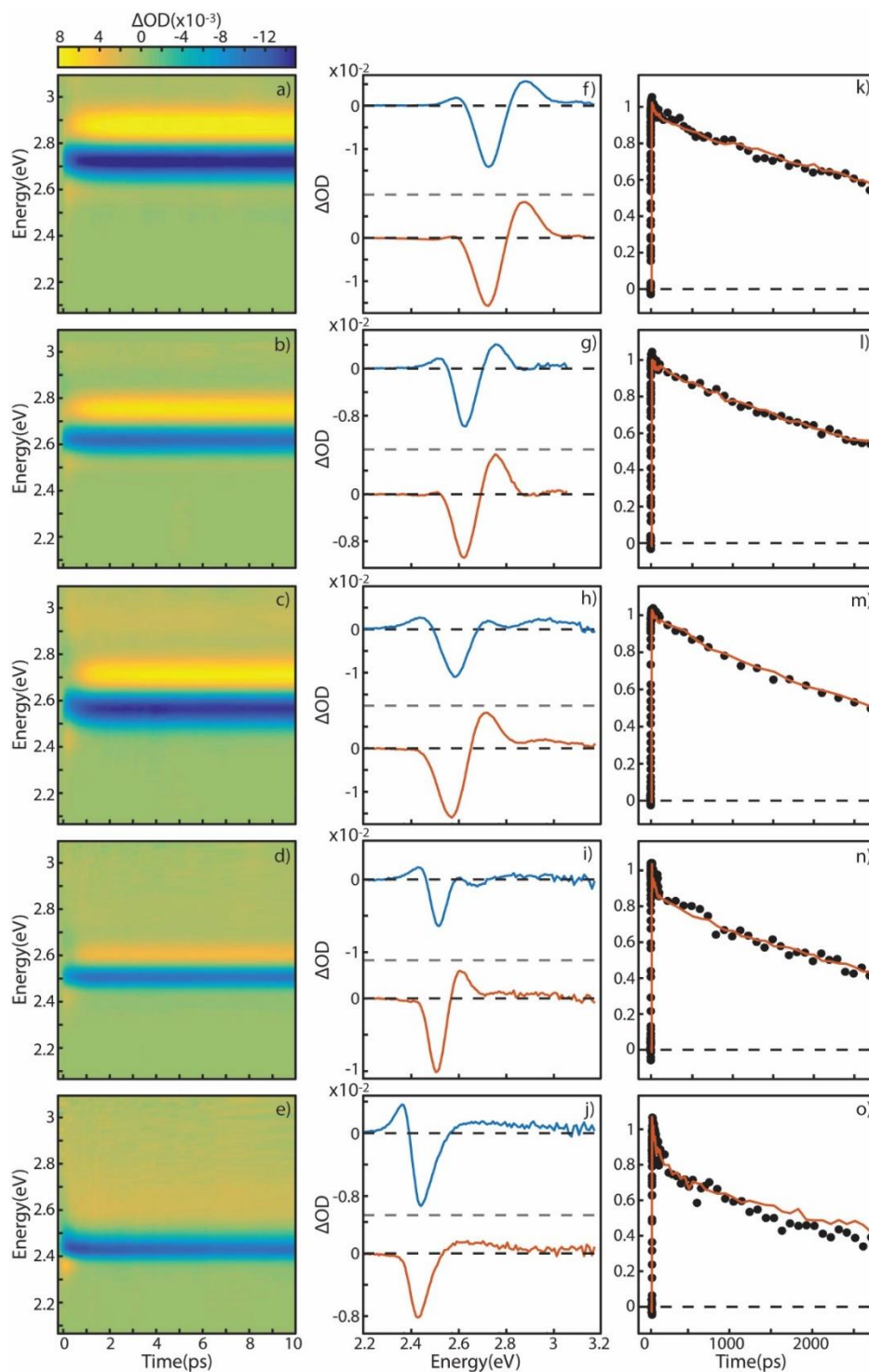


Figure 34: (a-e) Time resolved transient absorption spectra from samples (I, III, IV, V, VI) after excitation at 3.14 eV. (f-j) Slices at 200 fs and 10 ps (blue and red curves) taken from the corresponding spectra a-e. (k-o) decay dynamics from the bleach (red line) and IA signal (black circles) from the corresponding spectra a-e.

Figure 34 summarizes the size dependent transient absorption dynamics in the CsPbBr₃ quantum dots. The time resolved transient absorption spectra in the first ten picoseconds for samples (I, III, IV, V, VI) after 3.14 eV excitation are shown figure 2(a-e). The details of the transient absorption spectra are more easily observed in the spectra selected at 200fs and 10ps, blue and red curves figure 34(f-j). Excitation with 3.14 eV pump excites both electrons and holes above the E₁ transition with excess kinetic energy. In the first 500fs before hot-carrier relaxation, a derivative like feature is observed in the pump probe spectra resulting from the shifting of optical transitions in the presence of excited charge carriers. This feature has been observed before in large CsPbBr₃ nanoparticles being described as either the biexciton induced absorption feature or the transient stark effect. In the CsPbBr₃ QD we suspect this feature results from the transient stark effect as will be discussed in more detail later. As the hot electrons/holes relax to the band edge, the redshifted IA disappears and a state filling bleach signal develops at E₁ for each sized QD. The lack of state filling bleach at E₂ is consistent with the effective mass calculations which suggest that the E₁ and E₂ transitions result from two distinct sets of electron-hole states which are not strongly coupled. The most intriguing feature of the TA spectra is the strong IA observed on the high energy side of the bleach signal, resulting from the exciton induced turning on of a dipole forbidden transition. This formally forbidden transition involves electron-hole states with the same parity, has energy between E₁ and E₂ (E_{ia} table I).

The normalized decay of the IA and bleach features are overlaid in figure 34(k-o) for the respective size nanoparticle, displaying nearly identical decay dynamics. The rise and decay times for both the bleach and IA ($\tau_{\text{bl-decay}}$, $\tau_{\text{bl-rise}}$, $\tau_{\text{IA-decay}}$, $\tau_{\text{IA-rise}}$ $\tau_{\text{bl-decay}}$) for each sample are listed in table II. In CsPbBr₃ where the electron and hole have nearly identical effective mass ($m_e=0.134m_0$ $m_h=0.128m_0$), the state filling bleach signal represents a mixture of both electron and hole

dynamics probing the band edge exciton relaxation.¹⁸¹ The IA signal does not probe directly the band edge exciton population, however the identical decay dynamics suggests that the IA is modulated with the band edge exciton population, in other words the forbidden transition is turned on in the presence of band edge exciton.

In semiconductor quantum dots, there are a number of examples of high energy induced absorption features including biexcitons from higher lying exciton states, interband-absorption from photo-induced free carriers, and also the turning on of formally forbidden optical transitions. Biexcitons from higher energy exciton transitions are seen in the transient absorption spectra in other QD systems such as CdSe, however since the biexciton results in shifted optical transitions the IA should always be accompanied by an associated bleach signal. Recently this was proposed as the origin of the higher energy IA in the CsPbBr₃ nanoparticles, however without the associated bleach signal, the IA cannot be the result of biexciton.¹⁸¹ High energy intraband absorption is also unlikely as intraband absorption features tend to be broad, featureless, and at lower energies than the band gap. The observed IA has a well defined gaussian shape suggesting that it comes from an interband transition, furthermore the excess energy resulting from an intraband absorption at this energy would likely be enough to photo-ionize the nanoparticles. The induced absorption from free carriers has been discussed in perovskite thin films, however, considering the larger binding energy typical of the confined semiconductors, the existence of free carriers in CsPbBr₃ quantum dots is unlikely.

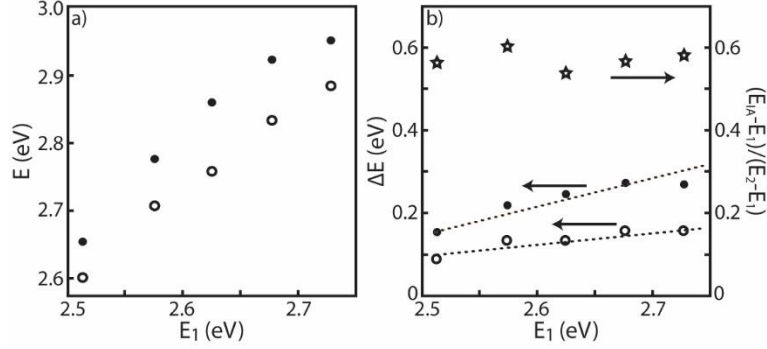


Figure 35: (a) Shift of E_{IA} and E_1 (open and closed circle) with particle size. a) Shift of $E_{IA}-E_1$, E_2-E_1 , (open and closed circles), and the ratio $\frac{E_2-E_{IA}}{E_2-E_1}$ (stars) as a function of the first exciton energy. The first exciton energy is taken as a placeholder for the size of the particle.

The size depending shifting of absorption features observed in both the steady state and time resolved absorption is dictated by the confinement induced changes to the electron and hole energy level. Figure 35a shows the size dependent shift of E_{IA} and E_2 (open and closed circles) and the energy of these transitions predicted using the four-band effective mass model (EMA). The lowest exciton transition E_1 involves the $j=1/2$ $\pi=-1$ electron and $j=1/2$ $\pi=1$ hole states, where j is the orbital angular momentum of the envelope function and π is the wavefunction parity. The E_2 transition is a mixture of four transitions with the strongest contribution from the $j=3/2$ $\pi=1$ electron and $j=3/2$ $\pi=-1$ hole states. The selection rules dictating these transitions require a change in parity between the electron and hole states which explains absence of the absorption between the $j=1/2$ and $j=3/2$ states, which match the E_{IA} transition observed in the transient absorption. In figure 3b, the ratio $(E_2-E_{IA})/(E_2-E_1) \approx 0.5$ and is shown to be nearly independent of the particle size, which is predicted from the EMA calculation where the conduction and valence band energy level spectra are symmetric, further the assignment of E_{IA} to the parity forbidden transition.¹⁸²

ps	I	II	III	IV	V	VI
$\tau_{\text{bl-decay}}$	5600	5400	4500	4000	4000	3400
$\tau_{\text{bl-rise}}$	0.59	0.51	0.65	0.59	0.35	0.2
$\tau_{\text{ia-decay}}$	5400	5200	4300	4000	4000	3100
$\tau_{\text{ia-rise}}$	0.85	0.75	0.82	0.7	0.42	0.2

Table 4: Fitting parameters of normalized transient absorption data to $-\sum a_i \cdot \exp(t/\tau_i)$ for E_{IA} and E_1 rise and decay times.

The observation of forbidden transitions in the steady state and time resolved absorption can be explained as the transfer of oscillator strength to due to a symmetry breaking perturbation. This has been observed in a number of materials typically involving the formation of a dipole moment, either inherent to the material, transiently generated in the excited state, or through external perturbation such as an applied electric field. Symmetry breaking perturbations act to distort the electron-hole wavefunctions resulting in redistributed oscillator strengths of allowed transitions, as well as inducing non-zero oscillator strengths of the forbidden transitions. For example in both CdSe, PbS, and PbSe quantum dots, internal dipole moments formed in the confined structures allow formally dark transitions to be observed. In the case of PbS quantum dots, the presence of localized hot charge carriers provides further oscillator strength to the forbidden transitions via a transient internal electric field, which is observed as an IA feature in the first ps of the transient absorption.⁷⁰ In the case of CsPbBr₃ quantum dots, the cubic lattice with inversion symmetry likely has a small or zero permanent dipole and the forbidden transition is only observed in the excited QD, suggesting that similar to the PbS, the perturbation is only observed in the excited state.

The exciton induced turning on of forbidden transition requires the symmetry breaking in the excited QD, which we suspect is the result of polaron formation. Polaron formation has been discussed both theoretically and experimentally in perovskite films and nanomaterials. Polarons form as the lattice deforms in the presence of a charge carrier, and the length of the deformation is critical as it dictates the extent of carrier localization. Small polarons form when carriers become highly localized to a few unit cells, whereas large polarons are formed when carriers become delocalized over many unit cells. While there is agreement in the fact that polarons form in perovskites, the exact nature and spatial extent is debated. When comparing recent studies on CsPbBr₃ perovskites, there are a range of results suggesting the existence of both electron and hole polarons that form over a range of length scales from a single unit cell to over 10 nm.

There are numerous scenarios in which polaron formation could induce a dipole moment. While it is impossible in our work to distinguish between individual electron or hole polaron or simultaneous electron/hole polarons, the information is not required to discuss the mechanism of dipole formation. In the case of simultaneous electron/hole polaron formation, both electron and hole would form spatially separated polarons, resulting in the formation of an internal electric field, similar to the case of the localized hot carriers in the PbS quantum dots. Alternatively, if either one or both polaron forms, the large and potentially asymmetric structural distortion could induce a significant deformation of the electronic structure or the formation of a dipole moment in the lattice. In either case relaxation of the optical selection rules could be expected.

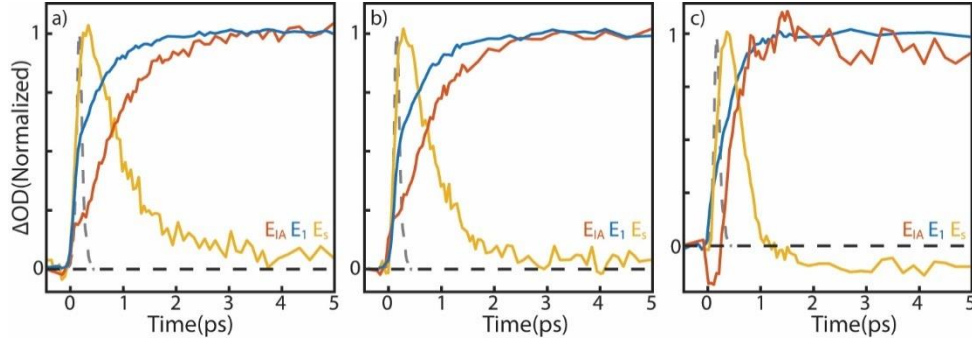


Figure 36: First five picoseconds showing the rise time of the bleach and both induced absorption signals from samples I, IV, and VI.

The effects of polaron on the relaxation dynamics in bulk CsPbBr₃ have been studied in the transient absorption as well as transient optical Kerr effect (TROKE) measurements. In the TROKE measurements, band edge excitation probes the coupling of the photoexcited charge carriers to the lattice, revealing polaron formation times (~ 700 fs). In TA spectra, the decay of the low energy induced absorption (E_S) also monitors the polaron formation. In both thin films and nanoparticles, E_S has been described as the redshift resulting from the transient stark effect in the presence of hot charge carriers. The transient stark effect results from an internal electric field typically in the presence of hot charge carriers. In the bulk CsPbBr₃ the polaron formation which effectively screens the charge carriers reduces the internal electric field, therefore, after polaron formation the stark effect should disappear as well as E_S . As such we take the decay time of E_S to monitor the polaron formation time. Figure 36 show the first five picoseconds of the bleach (E_I) and both induced absorption signals (E_{IA} , E_S) from sample I, IV, and VI, and the IRF for the instrument obtained via cross-correlation on a BBO. We observe nearly identical decay dynamics in of the E_S signal to the rise time of the E_{IA} signal which suggests that the turning on the forbidden transition is linked with the formation of the polaron. The polaron formation time extracted from

this analysis is between 700 and 800 fs which is consistent with other measurements on the polaron formation time in CsPbBr₃. Interestingly there is only a weak size dependence of the polaron formation time on the particle size, except for the larger particles where quantum confinement is negligible and the polaron formation dynamics may be different. It is worthwhile to note that the E₁ rise time, typically taken as a measure of the carrier cooling time, is faster than both the E_S decay time and the E_{1A} rise time. This is consistent with previous measurements which have also suggested that carrier cooling is much faster than the polaron formation. Similar to the polaron formation times, the E₁ rise time shows only a weak size dependence and the rise time is faster for larger particles. This result is inconsistent with other QD systems such as CdSe where, for a fixed excitation energy, smaller particles showed faster carrier cooling. However considering the differences between the transient absorption signals in these two systems, it is not unlikely that they behave differently.

7.3 Conclusion

We have observed the exciton induced turning on of forbidden transitions in CsPbBr₃ quantum dots, observed as the strong induced absorption feature in the transient absorption spectra. Through effective mass calculation we have identified this as the transition between parity forbidden states involving the electron and hole states from the two lowest exciton transitions. We suspect the turning on of this transition is mediated by the formation of a polaron, resulting in the broken symmetry and likely the formation of a dipole moment, known to have a strong effect on the optical selection rules. Using transient absorption, we extracted the polaron formation times in the various sized quantum dots, showing little size dependence except for in the larger particles where the polaron formation is more rapid.

CHAPTER VIII

DYNAMICS OF EXCITON-TO- Mn ENERGY TRANSFER IN Mn-DOPED CsPbCl₃ PEROVSKITE NANOCRYSTALS*

8.1 Introduction

Semiconducting cesium lead halide (CsPbX₃) perovskite nanocrystals have demonstrated superb photoluminescence (PL) and charge carrier transport properties that often outperform those of usual metal chalcogenide semiconductor nanocrystals.^{55, 59, 183-184} The generally high PL quantum yield (QY) and facile chemical or photochemical post-synthesis anion exchange that can fine-tune the bandgap make CsPbX₃ nanocrystals a promising alternative to II-VI and IV-VI semiconductor nanocrystals in various photonic and photovoltaic applications.^{58-59, 185} Recently, doping of paramagnetic Mn²⁺ ions, known to introduce new optical, magnetic, and charge carrier transfer properties in various semiconductor nanocrystals via exciton-dopant exchange coupling,¹⁸⁶ have been performed successfully in a few CsPbX₃ nanocrystals. For instance, Mn-doped CsPbCl₃ and CsPb(Cl/Br)₃ nanocrystals of cube or platelet shapes were synthesized, which showed Mn PL resulting from the energy transfer from exciton to Mn²⁺ ion^{84, 187-189} similar to the well-known cases of Mn-doped II-VI semiconductor nanocrystals. The observation of Mn PL in Mn-doped CsPbX₃ nanocrystals indicates that unique properties resulting from the coupling of exciton and dopant in magnetically doped semiconductor nanocrystals¹⁹⁰⁻¹⁹¹ may also be obtained in CsPbX₃ nanocrystal hosts. Since the strength of exchange coupling between exciton and dopant

* Reprinted in part with permission from Daniel Rossi, David Parobek, Yitong Dong, and Dong Hee Son. Dynamics of Exciton-Mn Energy Transfer in Mn-Doped CsPbCl₃ Perovskite Nanocrystals. *J. Phys. Chem. C*, **2017**, 121(32), 17143-17149. Copyright 2017 by the American Chemical Society.

is determined by the wavefunction overlap between exciton and d electrons of the dopant, it depends strongly on chemical and structural details of the doped nanocrystal.^{75, 186} If quantum confinement is imposed on the exciton of the host nanocrystals, the exchange coupling can be further altered by the host size and the spatial distribution of dopant within the nanocrystal. The effect of quantum confinement on enhancing exciton-Mn exchange coupling has been well demonstrated in II-VI quantum dots as the enhanced magneto-optic properties or exciton-Mn energy transfer rate.^{75, 192-193}

To further explore the properties originating from exciton-dopant exchange coupling in the newly accessible CsPbX₃ nanocrystal host, information on its strength relative to other existing doped nanocrystal systems will be informative. Using recently developed procedures for Mn-doping in CsPbX₃ with X=Cl and mixed Cl/Br, a comparative study between of the exchange coupling with other existing Mn-doped semiconductor nanocrystals will provide insight into the strength of exchange coupling in this new family of host nanocrystals. To this end, we measured exciton-to-Mn energy transfer time (τ_{ET}) in CsPbCl₃ nanocrystals, which can provide a means to estimate the relative strength of exciton-dopant coupling in CsPbCl₃ nanocrystals. Here, we compared τ_{ET} in Mn-doped CsPbCl₃ nanocrystals with that of Mn-doped CdS/ZnS core/shell quantum dots, where detailed measurement of τ_{ET} correlated with structural variation of the nanocrystals has already been performed. While comparison of τ_{ET} in these two systems reveals weaker exciton-Mn exchange coupling in CsPbCl₃ nanocrystals, it is not far behind doped CdS/ZnS. Considering the structural differences between the systems, the exchange coupling in CsPbCl₃ can potentially be enhanced through structural tuning of the size and dopant concentration. With further progress in the synthesis of Mn-doped CsPbX₃ nanocrystals, one

should be able to take full advantage of the superior properties of CsPbX₃ nanocrystals for hosting the magnetic dopants.

8.2 Results and Discussion

Among the currently available Mn-doped CsPbX₃ nanocrystals, we chose Mn-doped CsPbCl₃ nanocrystals of cube shape, although CsPbCl₃ host is considered to have more defects responsible for the lower QY of exciton PL compared with the mixed Cl and Br composition.⁸⁴ This is because CsPbCl₃ and Mn-doped CsPbCl₃ nanocrystals can be prepared with closely matching absorption spectra and sizes, which is important for the reliable measurement of the energy transfer time from the comparative analysis of the transient absorption data. Mn-doped CsPbCl₃ nanocrystals synthesized here using the procedure we recently developed is considered to have Mn²⁺ occupying Pb²⁺ site with relatively homogenous environment.⁸⁴ Figure 37a and b show the TEM images of undoped and Mn-doped CsPbCl₃ nanocrystals respectively. The average size of both nanocrystal samples are ~10 nm. The absorption and PL spectra of both samples are shown in Figure 37c and d respectively. The illustration of the crystal structure, where Mn²⁺ ions substitute Pb²⁺ sites, together with the photographs of the emission from doped and undoped samples is shown in Figure 37e. The doping concentration of Mn²⁺ ions determined from inductive-coupled plasma (ICP) mass spectrometry is ~0.4 % relative to Pb²⁺ ions in the lattice. The structural characterization of this material was more extensively performed in our earlier work (ref. 8), which also sheds some light on doping structure. Single exponential decay of Mn PL lifetime and the well-defined EPR spectra of Mn, representative of *d5* high-spin under a cubic ligand field, suggest a relatively homogenous and well-defined doping environment, strongly supporting doping in the nanocrystal interior. It is possible that Mn is close to the surface and not exposed to the exterior, however in such a case, we would have seen heterogeneous dynamics from Mn PL which is absent in our experimental data (reference 73). Furthermore, even if Mn is close the surface they are likely fully coordinated by Cl⁻ considering the highly Cl⁻ rich synthetic

conditions. In such a case, there would be little difference between the surface Mn and those buried deep inside, especially when the lattice symmetry and nanocrystal morphology are close to cubic. X-ray diffraction (XRD) patterns of both undoped and Mn-doped CsPbCl₃ nanocrystals are shown in Figure 37f. Nearly identical XRD patterns between the two samples indicate negligible effect of Mn-doping on the crystal lattice. At this relatively low doping concentration, the effect of Mn²⁺ ions on the band structure of the host nanocrystals is insignificant as seen from the nearly identical absorption spectra in Figure 37c. Mn-doped CsPbCl₃ nanocrystals exhibit exciton PL centered at 400 nm and Mn PL centered at 600 nm resulting from exciton-to-Mn energy transfer. Interestingly, exciton PL in Mn-doped CsPbCl₃ nanocrystals is stronger than in undoped nanocrystals contrary to the expectation. This is considered due to the relatively high density of charge carrier-trapping defects in CsPbCl₃ nanocrystals compared to CsPbBr₃ and CsPbI₃, which is may have been partially removed by the doping procedure as will be discussed in detail later. The potentially higher defect (or trap) density is also responsible for the significantly lower exciton PL QY of CsPbCl₃ nanocrystals compared to CsPbBr₃ and CsPbI₃ nanocrystals.

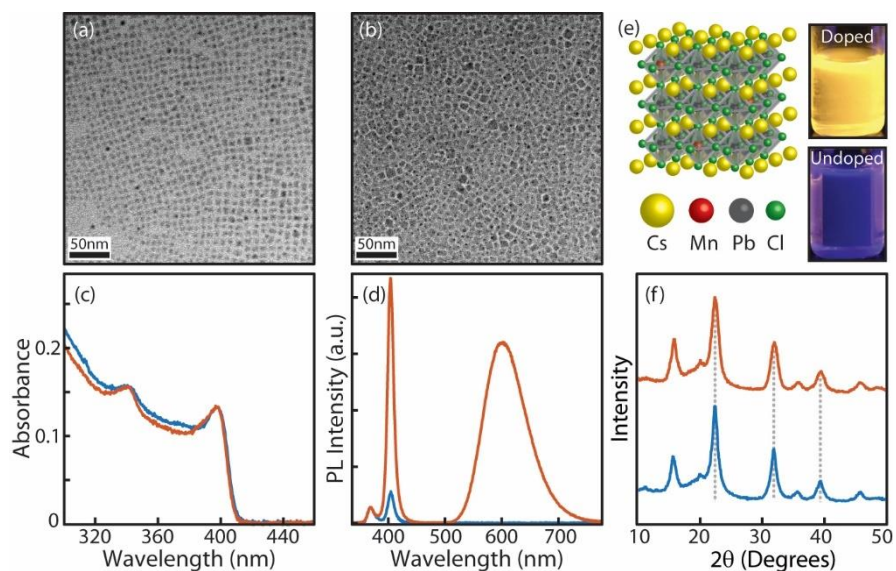


Figure 37. (a,b) TEM images of undoped (a) and Mn-doped (b) CsPbCl₃ nanocrystals. (c,d) Absorption and PL spectra of undoped (blue) and Mn-doped (red) CsPbCl₃ nanocrystals respectively. Small peak at ~370 nm in the PL spectra is from the excitation light. (e) Illustration of the crystal structure of Mn-doped CsPbCl₃ and the photographs of PL from Mn-doped and undoped CsPbCl₃ nanocrystal solutions. (f) XRD patterns from undoped (blue) and Mn-doped (red) CsPbCl₃ nanocrystals.

The exciton-to-Mn energy transfer time (τ_{ET}) in CsPbCl₃ nanocrystals was measured from the comparative analysis of the exciton relaxation dynamics in Mn-doped and undoped nanocrystals via pump-probe transient absorption spectroscopy monitoring the dynamics of exciton relaxation. Figure 38a shows the major dynamic processes in undoped (black box) and Mn-doped (red box) nanocrystals. In this scheme, doping of Mn²⁺ ions in the host nanocrystal introduces an additional pathway for the depletion of exciton, i.e., the energy transfer from exciton to Mn²⁺ ions. Therefore, the difference in the exciton relaxation dynamics in Mn-doped and undoped CsPbCl₃ nanocrystals carries information on the dynamics of the energy transfer. A similar comparative kinetic analysis made recently for Mn-doped CdS/ZnS quantum dots proved

that reliable energy transfer time can be obtained when the dopant functions as the energy acceptor not as the charge carrier acceptor.⁷⁵

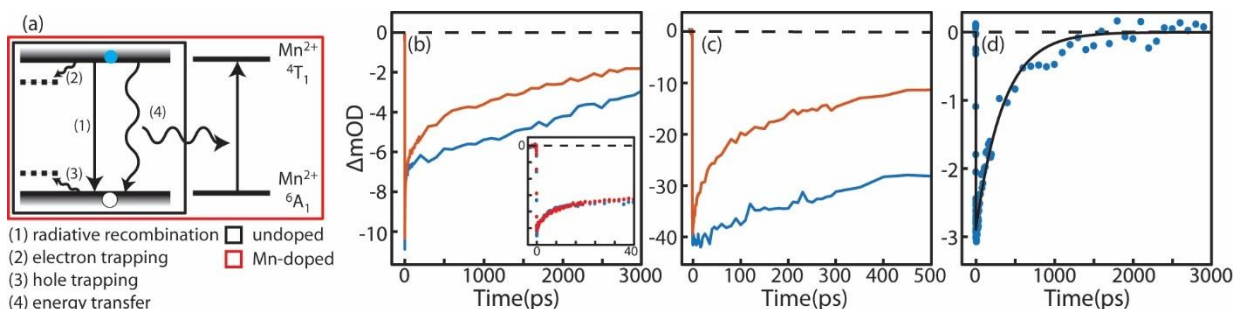


Figure 38. (a) The competing dynamic processes in undoped and Mn-doped perovskite nanocrystals. (b) Transient absorption data of undoped (blue) and Mn-doped (red) CsPbCl₃ nanocrystals with 395 nm pump and 400 nm probe. (c) Transient absorption data of undoped (blue) and Mn-doped (red) CdS/ZnS core/shell quantum dots. Data from Reference 14 are replotted. (d) The difference between the two transient absorption data in (b) taken after normalizing to the ns recovery component. See the text.

Here, transient absorption of the nanocrystals were obtained with 395 nm pump and 400 nm probe near the peak of the exciton absorption, where the dynamics of bleach recovery reflects primarily the dynamics of electron population with partial contribution from the hole dynamics.¹⁹⁴ Figure 38b compares the transient absorption data obtained from undoped (blue) and Mn-doped (red) CsPbCl₃ nanocrystals under the identical experimental conditions including the sample concentration and pump intensity. Pump intensity was kept low to avoid Auger relaxation of multiple excitons, which was ascertained by confirming the absence of the pump intensity dependent dynamics. The inset of Figure 38b shows the early time dynamics during the first 40 ps for both Mn-doped and undoped CsPbCl₃ nanocrystals, where the initial rapid recovery occurring on 5-7 ps is more clearly discernible.

The recovery of the bleach in undoped CsPbCl₃ nanocrystals shows two distinct components with very different time scales. The time constants obtained from multiexponential fit of the transient absorption data are $\tau_1=4.8$ ps and $\tau_2=3.7$ ns for the fast and slow recovery component respectively as summarized in Table 3. The fast recovery component (τ_1) is attributed to the subpopulation of CsPbCl₃ nanocrystals that undergo rapid electron trapping at the defects that may be from the Cl vacancy known to function as the electron trap.¹⁹⁵⁻¹⁹⁶ A large relative amplitude of τ_1 component (a_1) is consistent with typically much lower QY of exciton PL from CsPbCl₃ (1-10%)⁵⁹ compared to CsPbBr₃ and CsPbI₃ nanocrystals (50-90%), where the rapid bleach recovery attributed to electron trapping is absent in the transient absorption data.^{195, 197} The possibly more prominent halide vacancy in CsPbCl₃ than in other halide perovskites is also consistent with the large increase of the PL following a post-synthesis procedure that partially removes the Cl vacancy, which will be discussed later in detail. The rapid electron trapping occurring on several ps time scale in CsPbCl₃ nanocrystals suppresses exciton-to-Mn energy transfer, since the localization of electron wavefunction at the trap sites should reduce the exciton-Mn exchange coupling which mediates the energy transfer.¹⁹⁸ For this reason, the dynamics of this subpopulation of CsPbCl₃ nanocrystals are not affected by the energy transfer occurring on hundreds of ps as will become clearer later in the discussion.

The ns recovery component (τ_2) in the transient absorption of CsPbCl₃ nanocrystals accounts for the remaining subpopulation that undergoes the combination of radiative and other slower nonradiative recombination of exciton without having rapid electron trapping. It is worth mentioning that τ_2 of CsPbCl₃ nanocrystals is similar to the bleach recovery of CsPbBr₃ nanocrystals (~4.5 ns) probed at the peak of exciton absorption from recent study, which do not

exhibit ps bleach recovery dynamics.^{194, 199} This suggests that the exciton relaxation in the subpopulation of CsPbCl₃ nanocrystals represented by τ_2 is similar to that of CsPbBr₃ nanocrystals. It is this subpopulation of CsPbCl₃ nanocrystals, whose dynamics are modified when the energy transfer pathway opens by Mn doping as can be seen in Figure 38b.

Sample	a_1	a_2	a_3	τ_1 (ps)	τ_2 (ns)	τ_3 (ps)
CsPbCl ₃	0.34±0.03	0.66±0.02	---	4.8±1.1	3.7±0.4	---
Mn-doped CsPbCl ₃	0.33±0.02	0.4±0.02	0.27±0.02	6.6±1	3.9±0.5	380±20

Table 5: Fitting parameters of normalized transient absorption data to $-\sum a_i \exp(t/\tau_i)$.

Unlike in undoped CsPbCl₃ nanocrystals, the recovery of the bleach in Mn-doped CsPbCl₃ nanocrystals has three different time components. The fast ($\tau_1=6.6$ ps) and slow ($\tau_2=3.9$ ns) recovery components with the similar time constants to those of undoped CsPbCl₃ nanocrystals have the same origin as the undoped nanocrystals. Since the subpopulation that undergoes rapid electron trapping (τ_1) is not affected by the energy transfer, the relative amplitude (a_i) of τ_1 component is similar between undoped and doped nanocrystals. Therefore, we can ignore τ_1 component in the bleach recovery in the comparative analysis of exciton relaxation dynamics to extract the energy transfer time. In contrast, τ_2 component of the bleach recovery in undoped CsPbCl₃ nanocrystals branches into two components with the time constants of τ_2 and τ_3 in Mn-doped CsPbCl₃ nanocrystals, while keeping τ_2 nearly the same between the doped and undoped nanocrystals. It is notable that the difference in the bleach recovery dynamics between Mn-doped and undoped CsPbCl₃ nanocrystals resembles that of Mn-doped CdS/ZnS quantum dots from our

earlier study⁸⁴ reproduced in Figure 38c, if τ_1 component is ignored. Although the time scales of the bleach recovery are different in CsPbCl₃ and CdS/ZnS, the appearance of the additional recovery component (τ_3) upon Mn doping and insensitivity of τ_2 on doping are the common features in both systems. The similar change of the dynamics upon Mn doping in Figure 38b and c also indicates that the two materials have similar competitive kinetic schemes, where the two competing processes result in the branching of the nanocrystal population taking different relaxation paths. The new component with $\tau_3=380$ ps in Mn-doped CsPbCl₃ nanocrystals represents exciton-to-Mn energy transfer and its relative amplitude ($a_3=0.27$) is interpreted as the relative population of the nanocrystals that undergo the energy transfer. The remaining fraction of the population ($a_2=0.4$), which has nearly the same time constant τ_2 as in undoped CsPbCl₃ nanocrystals, is the subpopulation that does not undergo the energy transfer. Figure 38d shows more clearly the dynamics of the energy transfer, which has been isolated by taking the difference between the two transient absorption data shown in Figure 38b after normalizing them to the τ_2 component. As in the case of Mn-doped CdS/ZnS quantum dots, the population relaxing with time constant τ_2 in undoped CsPbCl₃ nanocrystals splits into two sub-populations after doping, one that undergoes the energy transfer and the other that does not. Since the charge carrier trapping suppresses the energy transfer by reducing the exciton-Mn exchange coupling, these two sub-populations represent the competition between the energy transfer and the additional charge carrier trapping pathway different from that represented by τ_1 .

In contrast to the rapid electron trapping that appears as the initial ps recovery of the bleach (τ_1) in transient absorption data, the charge carrier trapping competing with the energy transfer should be much slower. Taking $a_3/a_2 = 0.27/0.4$ as the branching ratio between the energy transfer

($\tau_3=380$ ps) and competing charge carrier trapping following the analysis scheme in Ref. 14, the time scale of the charge carrier trapping (τ_{trap}) from $a_3/a_2 = \tau_{\text{trap}}/\tau_3$ is ~ 260 ps. Considering that the full recovery of the bleach reflecting primarily the electron dynamics takes ~ 4 ns and that τ_{trap} is not clearly visible in the bleach recovery dynamics, trapping of hole rather than electron is more likely to compete with the energy transfer process.

Taking $a_3=0.27$ as the fraction of the Mn-doped nanocrystal population undergoing the energy transfer, the QY of Mn PL (Φ_{Mn}) should be expressed as $\Phi_{\text{Mn}} = a_3 \times \phi_{\text{Mn}}$, where ϕ_{Mn} is the QY of radiative relaxation of the excited ligand field state of Mn^{2+} ion. Although ϕ_{Mn} is not known in CsPbCl_3 nanocrystal host, we estimate its upper limit to be ~ 0.6 from the ratio of Mn PL lifetime of Mn-doped CsPbCl_3 nanocrystals in this study (1.1 ± 0.02 ms, Figure S1 in reference 73) and the longest Mn PL lifetime reported so far (1.75 ms) in the samples with the lower doping concentration ($< 0.2\%$) reported recently.⁸⁴ Considering that ϕ_{Mn} approached 1 in Mn-doped CdS/ZnS quantum dots at low doping concentration in the earlier study, ϕ_{Mn} of 0.6 estimated above should not be far from its true value. The measured QY of Mn PL from Mn-doped CsPbCl_3 nanocrystals studied here is 14%, which is close to what is predicted (16%) from $\Phi_{\text{Mn}} = a_3 \times \phi_{\text{Mn}}$ using the estimated upper limit value of $\phi_{\text{Mn}}=0.6$ and $a_3=0.27$.

As mentioned earlier, the exciton PL in Mn-doped CsPbCl_3 nanocrystals (QY=3.4%) is stronger than in undoped nanocrystals (QY $< 1\%$) contrary to the expectation. This seemingly contradicting observation may result from the relatively high density of defects (Cl vacancy) in CsPbCl_3 nanocrystals, which can be different between doped and undoped nanocrystals due to the difference in the synthesis condition, i.e., absence vs presence of large amount of MnCl_2 in the reaction mixture. In fact, we recently observed a large increase of the weak exciton PL of the

freshly synthesized CsPbCl₃ nanocrystals after the photoinduced self-anion exchange,⁵⁸ which was considered to be due to the partial removal of the halide vacancies. The increase of the Cl/Pb ratio from 2.5 to 3.3 observed after the self-anion exchange determined from EDS is also consistent with such scenario. The effects of the photoinduced self-anion exchange of CsPbCl₃ nanocrystals on the absorption and PL spectra are shown in Figure 39a and b. A small increase in the absorption intensity of the CsPbCl₃ nanocrystal samples after the self-anion exchange can be understood as the increased density of states involved in the interband transition resulting from the increased Cl content. The QY of exciton PL increased from 0.4 % to 13% after the self-anion exchange. This result is in stark contrast to the absence of the change of the absorption intensity and much smaller increase of the PL intensity in CsPbBr₃ nanocrystals after the self-anion exchange procedure presumably due to the lower preexisting Br vacancy or (and) its weaker role as the charge carrier trap.

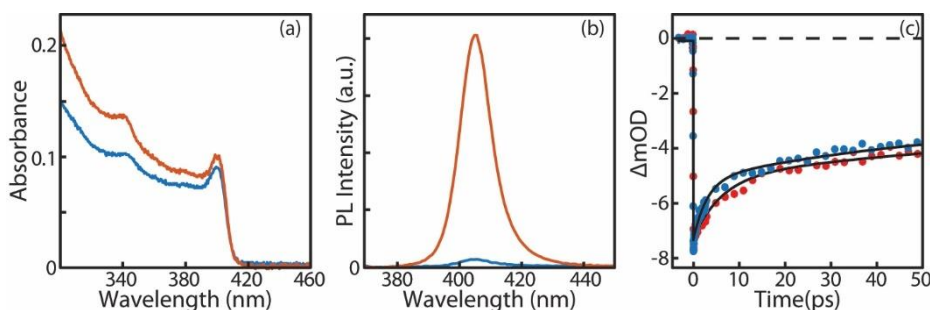


Figure 39. Comparison of (a) absorption, (b) PL emission and (c) transient absorption probed at the peak of exciton absorption between freshly synthesized (blue) and self-anion exchanged (red) CsPbCl₃ nanocrystals.

Reducing Cl vacancy also affects the early-time dynamics of the bleach recovery as shown in Figure 39c. The time constant of the fast recovery component attributed to the rapid electron trapping increased from 4.7 ps to 6.7 ps after the self-anion exchange with a small increase of the

amplitude of ns recovery component. The difference in the transient absorption, although relatively small, is consistent with the partial removal of the electron trapping defects. It is also notable that the difference in the two time constants (4.7 ± 1.1 and 6.7 ± 1.3 ps) is similar to that between τ_1 of undoped and Mn-doped CsPbCl₃ nanocrystals in Table 4. These results suggest that Mn-doping procedure may have removed some of the electron-trapping defects abundant in CsPbCl₃ nanocrystals. We anticipate such effect of Mn doping will be less pronounced in CsPbBr₃ nanocrystals having much less preexisting defects.

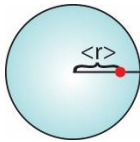
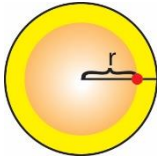
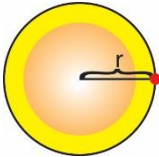
Host nanocrystal	CsPbCl ₃	CdS/ZnS core/shell	
Nanocrystal shape and size (nm) <i>l</i> : length, <i>d</i> : diameter, <i>t</i> : thickness	Cube with <i>l</i> =10±1.4	Sphere with core <i>d</i> =3.6 and shell <i>t</i> =0.6	
Volume of CsPbCl ₃ nanocrystal/Mn (nm ³)	50		
Exciton Bohr Radius (nm)	2.5	2.8	
Dopant distribution in nanocrystal	Random	Radially controlled	
(Average) Radial doping location from the center of a sphere (nm)	$\langle r \rangle = 1.7$ 	$r = 1.8$ 	$r = 2.4$ 
Energy Transfer Time, τ_{ET} (ps)	380	70	190

Table 6: Comparison of the structural parameters and the energy transfer time (τ_{ET}) of Mn-doped CsPbCl₃ nanocrystal and Mn-doped CdS/ZnS core/shell quantum dots. The data for Mn-doped CdS/ZnS quantum dot were extracted from Reference 14.

With the energy transfer time (τ_{ET}) in Mn-doped CsPbCl₃ nanocrystals, the relative strength of exciton-Mn exchange coupling in CsPbCl₃ with respect to CdS/ZnS quantum dots was examined by comparing τ_{ET} in these two materials as follows. A series of τ_{ET} values available for Mn-doped CdS/ZnS quantum dot as a function of doping concentration and radial doping location controlled during the synthesis are particularly useful for the comparison of τ_{ET} in the two different host nanocrystals.⁷⁵ The size of the host nanocrystal, exciton Bohr radius, and spatial distribution of dopant within the host nanocrystal, shown in Table 6, are important differences between the two Mn-doped nanocrystals, which makes the comparison of τ_{ET} rather complex. To make the most meaningful comparison, we first calculated the volume of Mn-doped CsPbCl₃ nanocrystals per each doped Mn²⁺ ion (50 nm³) from the measured average doping concentration (20/particle) and the average volume of the nanocrystal (1000 nm³). Assuming Mn²⁺ ions are doped randomly inside CsPbCl₃ nanocrystal and placing the center of the exciton wavefunction at the center of 50 nm³ sphere, the average doping radius from the center of the sphere was calculated to be $\langle r \rangle = 1.7$ nm (reference 73). For Mn-doped CdS/ZnS quantum dots of spherical shape, where the radial doping locations (r) were controlled via SILAR (Successive Ionic Layer Adsorption and Reaction) synthesis procedure, we chose two structures reported in Reference 14 with r close to $\langle r \rangle = 1.7$ nm in Mn-doped CsPbCl₃. τ_{ET} for these two Mn-doped CdS/ZnS quantum dots at the doping concentration of 1/particle were obtained from the linear slope of the reported doping concentration-dependent energy transfer rates.⁷⁵ In this comparison, τ_{ET} in CsPbCl₃ is 2-5 times longer than in CdS/ZnS when compared with τ_{ET} of Mn-doped CdS/ZnS quantum dots with $r = 2.4$ and 1.8 nm. This may be interpreted as weaker exciton-dopant exchange coupling in CsPbCl₃ than in CdS/ZnS nanocrystals. However, considering the differences in the parameters relevant to

quantum confinement in these two different materials, the difference in the strength of exciton-dopant exchange coupling may become less when the nanocrystals of the same sizes are compared. The currently available Mn-doped CsPbX₃ nanocrystals are limited to CsPbCl₃ and CsPb(Cl/Br)₃ with high Cl content having significantly smaller exciton Bohr radius than the size of the nanocrystals, therefore not benefiting from the enhanced exciton-dopant exchange coupling under quantum confinement. With the expansion of the host to CsPbBr₃ and CsPbI₃ having the larger Bohr exciton radius and smaller defect density than CsPbCl₃ and to the smaller nanocrystal size regime imposing quantum confinement, one should be able to gain the stronger exciton-Mn exchange coupling.

8.3 Conclusion

In conclusion, we studied the dynamics of exciton-to-Mn energy transfer in Mn-doped CsPbCl₃ nanocrystals to gain an insight into the relative strength of exciton-Mn exchange coupling via comparative analysis of the energy transfer times (τ_{ET}). Compared to Mn-doped CdS/ZnS quantum dots, Mn-doped CsPbCl₃ nanocrystals exhibit several times longer τ_{ET} , indicating weaker exciton-Mn exchange coupling partially due to the larger particle size lacking quantum confinement. The results demonstrate that with further progress in the control of the size and composition of the host to enhance the exciton-dopant exchange coupling, Mn-doped CsPbX₃ could become a promising new family of magnetically doped semiconductor nanocrystals.

8.4 Experimental Detail

8.4.1 Nanoparticle Structural and Chemical Characterization

Transmission electron microscopy (TEM) images and energy dispersive spectroscopy (EDS) data of undoped and Mn-doped CsPbCl₃ nanocrystals were obtained on a FEI Tecnai G2 F20 ST FE-TEM microscope operated at 4100 kV. EDS measurement was made to examine the effect of Mn doping and self-anion exchange on Pb/Cl ratio in CsPbCl₃ nanocrystals. X-ray diffraction (XRD) patterns of undoped and Mn-doped CsPbCl₃ nanocrystals were obtained using a Bruker-AXS GADDS MWPC diffractometer equipped with Cu K- α x-ray radiation with a multi-wire proportional counter. To determine the doping concentration in the Mn-doped CsPbCl₃ nanocrystals, the sample was digested in nitric acid and the elemental composition was determined using inductively coupled plasma mass spectrometry (ICP-MS) on a NexIon 300D mass spectrometer.

CHAPTER IX

CONCLUSIONS

9.1 Anisotropy of the Optical and Electro-Optic Properties in TMDC Nanodiscs

We have studied the optical and electro-optic properties in TMDC nanodiscs with confinement in both the lateral direction and the number of layers. The anisotropy of the TMDC structure results in unique observations including large interparticle electronic coupling, anisotropy of the induced dipole moment, the anisotropic coupling of excited charge carriers to the lattice dynamics. We also studied the relaxation and charge transfer dynamics in heterostructure TiS_2 nanodiscs, taking advantage of the large absorption crosssection in TiS_2 and the utility of TiO_2 for photocatalysis.

The optical absorption of colloidal solutions of 2-D layered TiS_2 nanodiscs with controlled diameter and thickness was strongly affected by the assembly of strongly interacting nanodiscs present within the solution. While this poses a significant challenge in studying the electronic structure of the layered TMDC nanoparticles correlated with the lateral and transverse dimensions, efficient separation of the nanodisc assemblies into non-interacting particles was achieved using pulsed photoexcitation in polar solvent. The pulsed photoexcitation is considered to weaken the interparticle cohesive force and facilitate the solvation of individual particles by the solvent molecules via transient modification of the charge distribution in the nanodiscs.

The unusual electric field-induced alignment of colloidal TMDC nanodiscs, where the orientational order was created only transiently by the time-variation of the electric field, while no orientational order can be established by the DC electric field. The linear dichroism signal probing the orientational order under the square wave field is equivalent to performing an edge detection of the electric field and its magnitude is dependent on the step height (ΔE) at the field edges, but

not on the amplitude of the field (E). This contrasts to the typical response of anisotropic colloidal nanocrystals to the electric field, where the permanent dipole or (and) anisotropic induced dipole results in a sustaining orientational order under the DC field. We conjecture that the anisotropic dielectric relaxation in the highly anisotropic TMDC nanodiscs may create a time-varying anisotropy of the induced dipole, resulting in the transient rotational order. Nevertheless, a near-steady state orientational order could be created using an AC square wave field at frequencies higher than the orientational relaxation rate of the nanodiscs. We also showed that the near-steady state orientational order from the AC field can be utilized to control the surface orientation of the TMDC nanodiscs deposited on a solid substrate and exhibit orientation-dependent optical properties.

The preferential coupling of the interband optical transition with the intralayer coherent acoustic phonon mode over the interlayer mode in colloidal solution of TiS_2 nanodiscs illustrates anisotropic electron-phonon coupling in colloidal multi-layered TiS_2 nanodiscs. The transient absorption signal from the diameter and thickness-controlled TiS_2 nanodiscs exhibited an oscillatory feature, which is attributed to the modulation of the interband absorption peak energy by the intralayer breathing mode. On the other hand, the signature of the interlayer mode was not observed, while excitation of interlayer coherent phonon was previously observed in other non-colloidal exfoliated sheets of related TMDC materials. Additional insight into the anisotropic coupling of coherent phonon with interband optical transition was obtained from DFT calculations of the optical absorption spectra of TiS_2 as a function of the in-plane and out-of-plane strain. The calculations indicate that the interband optical transition has much higher sensitivity to the in-plane

strain than to the out-of-plane strain, consistent with the observation of the dominant signature of intralayer acoustic phonon mode in the transient absorption.

The relaxation dynamics in TiS_2 and $\text{TiS}_2/\text{TiO}_2$ heterostructure nanodiscs and the effects of the number of layers and lateral confinement were studied using time resolved absorption. Semiconductor/ TiO_2 heterostructures are commonly studied for applications such as visible light driven H_2 production, and TiS_2 is a highly efficient visible/nIR light absorber with an absorption cross-section two orders of magnitude larger than other semiconductors commonly used in such heterostructures. The TiS_2 nanodiscs in this study could be partially oxidized to form $\text{TiS}_2/\text{TiO}_2$ heterostructures via chemical oxidation forming TiS_2 nanodiscs with an outer shell of TiO_2 . We observed a strong bleach of the visible interband electronic transitions under both 400nm and 800nm excitation for both the TiS_2 and $\text{TiS}_2/\text{TiO}_2$ nanodiscs, and faster relaxation of the interband transitions in the heterostructures was attributed to the TiS_2 to TiO_2 electron transfer. This signature of electron transfer was observed under both 400nm and 800nm excitation indicating the possibility to use visible and nIR excitation to achieve charge separation.

9.5 Relaxation Dynamics in CsPbBr₃ Quantum Dots and Mn-Doped CsPbCl₃ Nanoparticles

The relaxation and energy transfer dynamics in size controlled CsPbBr₃ quantum dots and Mn-doped CsPbCl₃ nanoparticles were studied with transient absorption spectroscopy. Significant interest is given to the CsPbX₃ materials for their color tunable emission and robust optical properties. Only recently has it been possible to reliably control the size of the Perovskite nanoparticles into the quantum confinement regime, making it possible to study the size dependent optical properties. Towards this, we have observed the unique turning on of forbidden optical transitions in the quantum confined CsPbBr₃ resulting from the broken symmetry of the excited state. We have also explored the exciton-Mn energy transfer dynamics in Mn doped CsPbCl₃ nanoparticles.

We have observed the exciton induced turning on of forbidden transitions in CsPbBr₃ quantum dots, where a strong induced absorption is seen in the transient absorption spectra. Effective mass calculations have identified this feature as the transition between parity forbidden states involving electron and hole states from the two lowest exciton transitions. We suspect the turning on of the forbidden transition is mediated by the formation of a polaron, resulting in the broken symmetry and the formation of a dipole moment in the excited state, known to have a strong effect on the optical selection rules. Using transient absorption, we extracted the polaron formation times in the various sized quantum dots, showing little size dependence except for in the larger particles where the polaron formation is more rapid.

In the Mn-doped CsPbCl₃ where photoexcited charge carriers can transfer their energy to dopants, the dynamics of exciton-to-Mn energy transfer in Mn-doped CsPbCl₃ nanocrystals give insight into the relative strength of exciton-Mn exchange coupling via comparative analysis of the energy transfer times (τ_{ET}). Compared to Mn-doped CdS/ZnS quantum dots, Mn-doped CsPbCl₃

nanocrystals exhibit several times longer τ_{ET} , indicating weaker exciton-Mn exchange coupling partially due to the larger particle size lacking quantum confinement. The results demonstrate that with further progress in the control of the size and composition of the host to enhance the exciton-dopant exchange coupling, Mn-doped CsPbX₃ could become a promising new family of magnetically doped semiconductor nanocrystals.

REFERENCES

1. He, Z.; Que, W., Molybdenum disulfide nanomaterials: Structures, properties, synthesis and recent progress on hydrogen evolution reaction. *Applied Materials Today*. **2016**, *3*, 23-56.
2. Li, H.; Li, Y.; Aljarb, A.; Shi, Y.; Li, L.-J., Epitaxial Growth of Two-Dimensional Layered Transition-Metal Dichalcogenides: Growth Mechanism, Controllability, and Scalability. *Chemical Reviews*. **2017**.
3. Baek, S. H.; Choi, Y.; Choi, W., Large-Area Growth of Uniform Single-Layer MoS₂ Thin Films by Chemical Vapor Deposition. *Nanoscale Research Letters*. **2015**, *10*, 388.
4. Dong, R.; Kuljanishvili, I., Review Article: Progress in fabrication of transition metal dichalcogenides heterostructure systems. *Journal of Vacuum Science & Technology B, Nanotechnology and Microelectronics: Materials, Processing, Measurement, and Phenomena*. **2017**, *35*, 030803.
5. Zhang, X.-Q.; Lin, C.-H.; Tseng, Y.-W.; Huang, K.-H.; Lee, Y.-H., Synthesis of Lateral Heterostructures of Semiconducting Atomic Layers. *Nano Letters*. **2015**, *15*, 410-415.
6. Molina-Sánchez, A.; Wirtz, L., Phonons in single-layer and few-layer MoS₂ and WS₂. *Physical Review B*. **2011**, *84*, 155413.
7. Lee, C.; Yan, H.; Brus, L. E.; Heinz, T. F.; Hone, J., et al., Anomalous Lattice Vibrations of Single- and Few-Layer MoS₂. *ACS Nano*. **2010**, *4*, 2695-2700.
8. Zhao, Y.; Luo, X.; Li, H.; Zhang, J.; Araujo, P. T., et al., Interlayer Breathing and Shear Modes in Few-Trilayer MoS₂ and WSe₂. *Nano Letters*. **2013**, *13*, 1007-1015.
9. Berkdemir, A.; Gutierrez, H. R.; Botello-Mendez, A. R.; Perea-Lopez, N.; Elias, A. L., et al., Identification of Individual and Few Layers of WS₂ Using Raman Spectroscopy. *Scientific Reports*. **2013**, *3*.
10. Lu, X.; Utama, M. I. B.; Lin, J.; Luo, X.; Zhao, Y., et al., Rapid and Nondestructive Identification of Polytypism and Stacking Sequences in Few-Layer Molybdenum Diselenide by Raman Spectroscopy. *Advanced Materials*. **2015**, *27*, 4502-4508.
11. Zhao, W.; Ghorannevis, Z.; Amara, K. K.; Pang, J. R.; Toh, M., et al., Lattice dynamics in mono- and few-layer sheets of WS₂ and WSe₂. *Nanoscale*. **2013**, *5*, 9677-9683.
12. Mak, K. F.; Lee, C.; Hone, J.; Shan, J.; Heinz, T. F., Atomically Thin MoS₂: A New Direct-Gap Semiconductor. *Physical Review Letters*. **2010**, *105*, 136805.
13. Zhao, W.; Ghorannevis, Z.; Chu, L.; Toh, M.; Kloc, C., et al., Evolution of Electronic Structure in Atomically Thin Sheets of WS₂ and WSe₂. *ACS Nano*. **2012**, *7*, 791-797.

14. Yang, D.; Sandoval, S. J.; Divigalpitiya, W. M. R.; Irwin, J. C.; Frindt, R. F., Structure of single-molecular-layer MoS₂. *Physical Review B*. **1991**, *43*, 12053-12056.
15. Mrstik, B. J.; Kaplan, R.; Reinecke, T. L.; Van Hove, M.; Tong, S. Y., Surface-structure determination of the layered compounds MoS₂ and NbSe₂ by low-energy electron diffraction. *Physical Review B*. **1977**, *15*, 897-900.
16. Cheng, Y.; Zhu, Z.; Schwingenschlogl, U., Role of interlayer coupling in ultra thin MoS₂. *RSC Advances*. **2012**, *2*, 7798-7802.
17. Coehoorn, R.; Haas, C.; Dijkstra, J.; Flipse, C. J. F.; de Groot, R. A., et al., Electronic structure of MoSe₂, MoS₂, and WSe₂. I. Band-structure calculations and photoelectron spectroscopy. *Physical Review B*. **1987**, *35*, 6195-6202.
18. Cao, T.; Wang, G.; Han, W.; Ye, H.; Zhu, C., et al., Valley-selective circular dichroism of monolayer molybdenum disulphide. *Nature Communications*. **2012**, *3*, 887.
19. Rouxel, J.; Brec, R., Low-Dimensional Chalcogenides as Secondary Cathodic Materials: Some Geometric and Electronic Aspects. *Annual Review of Materials Science*. **1986**, *16*, 137-162.
20. Ikebe, M.; Katagiri, K.; Watanabe, Y.; Muto, Y., Interlayer coupling strength of layered superconductors, Ta_{1-x}Nb_xS₂ and Ta_{1-x}Nb_xS₂(Py)₁₂. *Physica B*. **1981**, *105*, 453-457.
21. Nabutovsky, V. M.; Eherman, K.; Tenne, R., Collection efficiency of photoexcited carriers of electrochemically etched surface. *Journal of Applied Physics*. **1993**, *73*, 2866-2870.
22. Huang, Z.; Wu, T.; Kong, S.; Meng, Q.-L.; Zhuang, W., et al., Enhancement of anisotropic thermoelectric performance of tungsten disulfide by titanium doping. *Journal of Materials Chemistry A*. **2016**, *4*, 10159-10165.
23. Jiang, P.; Qian, X.; Gu, X.; Yang, R., Probing Anisotropic Thermal Conductivity of Transition Metal Dichalcogenides MX₂ (M = Mo, W and X = S, Se) using Time-Domain Thermoreflectance. *Advanced Materials*. **2017**, *29*, 1701068.
24. Han, J. H.; Lee, S.; Cheon, J., Synthesis and structural transformations of colloidal 2D layered metal chalcogenide nanocrystals. *Chemical Society Reviews*. **2013**, *42*, 2581-2591.
25. Xu, S.; Li, D.; Wu, P., One-Pot, Facile, and Versatile Synthesis of Monolayer MoS₂/WS₂ Quantum Dots as Bioimaging Probes and Efficient Electrocatalysts for Hydrogen Evolution Reaction. *Advanced Functional Materials*. **2015**, *25*, 1127-1136.
26. Jeong, S.; Yoo, D.; Jang, J.-t.; Kim, M.; Cheon, J., Well-Defined Colloidal 2-D Layered Transition-Metal Chalcogenide Nanocrystals via Generalized Synthetic Protocols. *Journal of the American Chemical Society*. **2012**, *134*, 18233-18236.

27. Jeong, S.; Yoo, D.; Ahn, M.; Miró, P.; Heine, T., et al., Tandem intercalation strategy for single-layer nanosheets as an effective alternative to conventional exfoliation processes. *Nature Communications*. **2015**, *6*, 5763.
28. Jin, H.; Ahn, M.; Jeong, S.; Han, J. H.; Yoo, D., et al., Colloidal Single-Layer Quantum Dots with Lateral Confinement Effects on 2D Exciton. *Journal of the American Chemical Society*. **2016**, *138*, 13253-13259.
29. Murphy, C. J.; Orendorff, C. J., Alignment of Gold Nanorods in Polymer Composites and on Polymer Surfaces. *Advanced Materials*. **2005**, *17*, 2173-2177.
30. Rablau, C.; Vaishnava, P.; Sudakar, C.; Tackett, R.; Lawes, G., et al., Magnetic-field-induced optical anisotropy in ferrofluids: A time-dependent light-scattering investigation. *Physical Review E*. **2008**, *78*, 051502.
31. Ryan, K. M.; Mastroianni, A.; Stancil, K. A.; Liu, H.; Alivisatos, A. P., Electric-Field-Assisted Assembly of Perpendicularly Oriented Nanorod Superlattices. *Nano Letters*. **2006**, *6*, 1479-1482.
32. Li, L. S.; Alivisatos, A. P., Origin and Scaling of the Permanent Dipole Moment in CdSe Nanorods. *Physical Review Letters*. **2003**, *90*, 097402.
33. Zijlstra, P.; van Stee, M.; Verhart, N.; Gu, Z.; Orrit, M., Rotational diffusion and alignment of short gold nanorods in an external electric field. *Physical Chemistry Chemical Physics*. **2012**, *14*, 4584-4588.
34. van der Zande, B. M. I.; Koper, G. J. M.; Lekkerkerker, H. N. W., Alignment of Rod-Shaped Gold Particles by Electric Fields. *The Journal of Physical Chemistry B*. **1999**, *103*, 5754-5760.
35. Rossi, D.; Han, J. H.; Jung, W.; Cheon, J.; Son, D. H., Orientational Control of Colloidal 2D-Layered Transition Metal Dichalcogenide Nanodiscs via Unusual Electrokinetic Response. *ACS Nano*. **2015**, *9*, 8037-8043.
36. Ghosh, S. K.; Pal, T., Interparticle Coupling Effect on the Surface Plasmon Resonance of Gold Nanoparticles: From Theory to Applications. *Chemical Reviews*. **2007**, *107*, 4797-4862.
37. Burda, C.; Chen, X.; Narayanan, R.; El-Sayed, M. A., Chemistry and Properties of Nanocrystals of Different Shape. *Chemical Reviews*. **2005**, *105*, 1025-1102.
38. Zaitseva, N.; Dai, Z. R.; Leon, F. R.; Krol, D. J., Optical Properties of CdSe Superlattices. *Journal of the American Chemical Society*. **2005**, *127*, 10221-10226.

39. Kenrick, J. W.; Tisdale, W. A.; Leschkies, K. S.; Haugstad, G.; Norris, J. D., et al., Strong Electronic Coupling in Two-Dimensional Assemblies of Colloidal PbSe Quantum Dots. *ACS Nano*. **2009**, *3*, 1532-1538.
40. Konstantatos, G.; Howard, I.; Fischer, A.; Hoogland, S.; Clifford, J., et al., Ultrasensitive solution-cast quantum dot photodetectors. *Nature*. **2006**, *442*, 180.
41. Hetsch, F.; Zhao, N.; Kershaw, S. V.; Rogach, A. L., Quantum dot field effect transistors. *Materials Today*. **2013**, *16*, 312-325.
42. Rossi, D.; Camacho-Forero, L. E.; Ramos-Sánchez, G.; Han, J. H.; Cheon, J., et al., Anisotropic Electron-Phonon Coupling in Colloidal Layered TiS₂ Nanodiscs Observed via Coherent Acoustic Phonons. *The Journal of Physical Chemistry C*. **2015**, *119*, 7436-7442.
43. Sagar, D. M.; Cooney, R. R.; Sewall, S. L.; Dias, E. A.; Barsan, M. M., et al., Size dependent, state-resolved studies of exciton-phonon couplings in strongly confined semiconductor quantum dots. *Physical Review B*. **2008**, *77*, 235321.
44. Geiregat, P.; Delerue, C.; Justo, Y.; Aerts, M.; Spoor, F., et al., A Phonon Scattering Bottleneck for Carrier Cooling in Lead Chalcogenide Nanocrystals. *ACS Nano*. **2015**, *9*, 778-788.
45. Kioseoglou, G.; Hanbicki, A. T.; Currie, M.; Friedman, A. L.; Gunlycke, D., et al., Valley polarization and intervalley scattering in monolayer MoS₂. *Applied Physics Letters*. **2012**, *101*, 221907.
46. Wang, Y.; Wang, Q.; Zhan, X.; Wang, F.; Safdar, M., et al., Visible light driven type II heterostructures and their enhanced photocatalysis properties: a review. *Nanoscale*. **2013**, *5*, 8326-8339.
47. Toyoda, T.; Yindeesuk, W.; Kamiyama, K.; Katayama, K.; Kobayashi, H., et al., The Electronic Structure and Photoinduced Electron Transfer Rate of CdSe Quantum Dots on Single Crystal Rutile TiO₂: Dependence on the Crystal Orientation of the Substrate. *The Journal of Physical Chemistry C*. **2016**, *120*, 2047-2057.
48. Huang, J.; Yuan, Y.; Shao, Y.; Yan, Y., Understanding the physical properties of hybrid perovskites for photovoltaic applications. *Nature Reviews Materials*. **2017**, *2*, 17042.
49. García de Arquer, F. P.; Armin, A.; Meredith, P.; Sargent, E. H., Solution-processed semiconductors for next-generation photodetectors. *Nature Reviews Materials*. **2017**, *2*, 16100.
50. Sutherland, B. R.; Sargent, E. H., Perovskite photonic sources. *Nature Photonics*. **2016**, *10*, 295.

51. Liang, J.; Wang, C.; Wang, Y.; Xu, Z.; Lu, Z., et al., All-Inorganic Perovskite Solar Cells. *Journal of the American Chemical Society*. **2016**, *138*, 15829-15832.
52. Park, N.-G., Perovskite solar cells: an emerging photovoltaic technology. *Materials Today*. **2015**, *18*, 65-72.
53. Rolston, N.; Printz, A. D.; Hilt, F.; Hovish, M. Q.; Bruning, K., et al., Improved stability and efficiency of perovskite solar cells with submicron flexible barrier films deposited in air. *Journal of Materials Chemistry A*. **2017**, *5*, 22975-22983.
54. Zhang, F.; Yang, X.; Wang, H.; Cheng, M.; Zhao, J., et al., Structure Engineering of Hole-Conductor Free Perovskite-Based Solar Cells with Low-Temperature-Processed Commercial Carbon Paste As Cathode. *ACS Applied Materials & Interfaces*. **2014**, *6*, 16140-16146.
55. Protesescu, L.; Yakunin, S.; Bodnarchuk, M. I.; Krieg, F.; Caputo, R., et al., Nanocrystals of Cesium Lead Halide Perovskites (CsPbX₃, X = Cl, Br, and I): Novel Optoelectronic Materials Showing Bright Emission with Wide Color Gamut. *Nano Letters*. **2015**, *15*, 3692-3696.
56. Shoaib, M.; Zhang, X.; Wang, X.; Zhou, H.; Xu, T., et al., Directional Growth of Ultralong CsPbBr₃ Perovskite Nanowires for High-Performance Photodetectors. *Journal of the American Chemical Society*. **2017**, *139*, 15592-15595.
57. Cho, J.; Jin, H.; Sellers, D. G.; Watson, D. F.; Son, D. H., et al., Influence of ligand shell ordering on dimensional confinement of cesium lead bromide (CsPbBr₃) perovskite nanoplatelets. *Journal of Materials Chemistry C*. **2017**, *5*, 8810-8818.
58. Parobek, D.; Dong, Y.; Qiao, T.; Rossi, D.; Son, D. H., Photoinduced Anion Exchange in Cesium Lead Halide Perovskite Nanocrystals. *Journal of the American Chemical Society*. **2017**, *139*, 4358-4361.
59. Akkerman, Q. A.; D'Innocenzo, V.; Accornero, S.; Scarpellini, A.; Petrozza, A., et al., Tuning the Optical Properties of Cesium Lead Halide Perovskite Nanocrystals by Anion Exchange Reactions. *Journal of the American Chemical Society*. **2015**, *137*, 10276-10281.
60. Butkus, J.; Vashishtha, P.; Chen, K.; Gallaher, J. K.; Prasad, S. K. K., et al., The Evolution of Quantum Confinement in CsPbBr₃ Perovskite Nanocrystals. *Chemistry of Materials*. **2017**, *29*, 3644-3652.
61. Castañeda, J. A.; Nagamine, G.; Yassitepe, E.; Bonato, L. G.; Voznyy, O., et al., Efficient Biexciton Interaction in Perovskite Quantum Dots Under Weak and Strong Confinement. *ACS Nano*. **2016**, *10*, 8603-8609.
62. and, A. L. E.; Rosen, M., The Electronic Structure of Semiconductor Nanocrystals. *Annual Review of Materials Science*. **2000**, *30*, 475-521.

63. Li, J.; Xia, J.-B., Exciton states and optical spectra in CdSe nanocrystallite quantum dots. *Physical Review B*. **2000**, *61*, 15880-15886.
64. Klimov, V. I.; McBranch, D. W.; Leatherdale, C. A.; Bawendi, M. G., Electron and hole relaxation pathways in semiconductor quantum dots. *Physical Review B*. **1999**, *60*, 13740-13749.
65. Efros, A. L.; Rosen, M.; Kuno, M.; Nirmal, M.; Norris, D. J., et al., Band-edge exciton in quantum dots of semiconductors with a degenerate valence band: Dark and bright exciton states. *Physical Review B*. **1996**, *54*, 4843-4856.
66. Schmidt, M. E.; Blanton, S. A.; Hines, M. A.; Guyot-Sionnest, P., Size-dependent two-photon excitation spectroscopy of CdSe nanocrystals. *Physical Review B*. **1996**, *53*, 12629-12632.
67. Schmidt, M. E.; Blanton, S. A.; Hines, M. A.; Guyot-Sionnest, P., Polar CdSe nanocrystals: Implications for electronic structure. *The Journal of Chemical Physics*. **1997**, *106*, 5254-5259.
68. Schins, J. M.; Trinh, M. T.; Houtepen, A. J.; Siebbeles, L. D. A., Probing formally forbidden optical transitions in PbSe nanocrystals by time- and energy-resolved transient absorption spectroscopy. *Physical Review B*. **2009**, *80*, 035323.
69. Goupalov, S. V., Selection rules for optical transitions in PbSe nanocrystal quantum dots: Drastic effect of structure inversion asymmetry. *Physical Review B*. **2009**, *79*, 233305.
70. Trinh, M. T.; Sfeir, M. Y.; Choi, J. J.; Owen, J. S.; Zhu, X., A Hot Electron–Hole Pair Breaks the Symmetry of a Semiconductor Quantum Dot. *Nano Letters*. **2013**, *13*, 6091-6097.
71. Beaulac, R.; Archer, P. I.; Ochsenbein, S. T.; Gamelin, D. R., Mn²⁺-Doped CdSe Quantum Dots: New Inorganic Materials for Spin-Electronics and Spin-Photonics. *Advanced Functional Materials*. **2008**, *18*, 3873-3891.
72. Hughes, K. E.; Hartstein, K. H.; Gamelin, D. R., Photodoping and Transient Spectroscopies of Copper-Doped CdSe/CdS Nanocrystals. *ACS Nano*. **2018**, *12*, 718-728.
73. Rossi, D.; Parobek, D.; Dong, Y.; Son, D. H., Dynamics of Exciton–Mn Energy Transfer in Mn-Doped CsPbCl₃ Perovskite Nanocrystals. *The Journal of Physical Chemistry C*. **2017**, *121*, 17143-17149.
74. Dexter, D. L., A Theory of Sensitized Luminescence in Solids. *The Journal of Chemical Physics*. **1953**, *21*, 836-850.
75. Chen, H.-Y.; Maiti, S.; Son, D. H., Doping Location-Dependent Energy Transfer Dynamics in Mn-Doped CdS/ZnS Nanocrystals. *ACS Nano*. **2012**, *6*, 583-591.

76. Dong, Y.; Parobek, D.; Rossi, D.; Son, D. H., Photoemission of Energetic Hot Electrons Produced via Up-Conversion in Doped Quantum Dots. *Nano Letters*. **2016**, *16*, 7270-7275.
77. Kambhampati, P., Unraveling the Structure and Dynamics of Excitons in Semiconductor Quantum Dots. *Accounts of Chemical Research*. **2011**, *44*, 1-13.
78. Aneesh, J.; Swarnkar, A.; Kumar Ravi, V.; Sharma, R.; Nag, A., et al., Ultrafast Exciton Dynamics in Colloidal CsPbBr₃ Perovskite Nanocrystals: Biexciton Effect and Auger Recombination. *The Journal of Physical Chemistry C*. **2017**, *121*, 4734-4739.
79. Seth, S.; Mondal, N.; Patra, S.; Samanta, A., Fluorescence Blinking and Photoactivation of All-Inorganic Perovskite Nanocrystals CsPbBr₃ and CsPbBr₂. *The Journal of Physical Chemistry Letters*. **2016**, *7*, 266-271.
80. Shinde, A.; Gahlaut, R.; Mahamuni, S., Low-Temperature Photoluminescence Studies of CsPbBr₃ Quantum Dots. *The Journal of Physical Chemistry C*. **2017**, *121*, 14872-14878.
81. Isarov, M.; Tan, L. Z.; Bodnarchuk, M. I.; Kovalenko, M. V.; Rappe, A. M., et al., Rashba Effect in a Single Colloidal CsPbBr₃ Perovskite Nanocrystal Detected by Magneto-Optical Measurements. *Nano Letters*. **2017**, *17*, 5020-5026.
82. Becker, M. A.; Vaxenburg, R.; Nedelcu, G.; Sercel, P. C.; Shabaev, A., et al., Bright triplet excitons in caesium lead halide perovskites. *Nature*. **2018**, *553*, 189.
83. Yoo, D.; Kim, M.; Jeong, S.; Han, J.; Cheon, J., Chemical Synthetic Strategy for Single-Layer Transition-Metal Chalcogenides. *Journal of the American Chemical Society*. **2014**, *136*, 14670-14673.
84. Parobek, D.; Roman, B. J.; Dong, Y.; Jin, H.; Lee, E., et al., Exciton-to-Dopant Energy Transfer in Mn-Doped Cesium Lead Halide Perovskite Nanocrystals. *Nano Letters*. **2016**, *16*, 7376-7380.
85. Chhowalla, M.; Shin, H. S.; Eda, G.; Li, L.; Loh, K. P., et al., The Chemistry of Two-Dimensional Layered Transition Metal Dichalcogenide Nanosheets. *Nature Chemistry*. **2013**, *5*, 263-375.
86. Wang, Q. H.; Kalantar-Zadeh, K.; Kis, A.; Coleman, J. N.; Strano, M. S., Electronics and Optoelectronics of Two-Dimensional Transition Metal Dichalcogenides. *Nature Nanotechnology*. **2012**, *7*, 699-712.
87. Butler, S. Z.; Hollen, S. M.; Cao, L.; Cui, Y.; Gupta, J. A., et al., Progress, Challenges, and Opportunities in Two-Dimensional Materials Beyond Graphene. *ACS Nano*. **2013**, *7*, 2898-2926.

88. Cheon, J.; Gozum, J. E.; Girolami, G. S., Chemical Vapor Deposition of MoS₂ and TiS₂ Films From the Metal–Organic Precursors Mo(S-t-Bu)₄ and Ti(S-t-Bu)₄. *Chemistry of Materials*. **1997**, *9*, 1847-1858.
89. Zhan, Y.; Liu, Z.; Najmaei, S.; Ajayan, P. M.; Lou, J., Large-Area Vapor-Phase Growth and Characterization of MoS₂ Atomic Layers on a SiO₂ Substrate. *Small*. **2012**, *8*, 966-971.
90. Eda, G.; Yamaguchi, H.; Voiry, D.; Fujita, T.; Chen, M., et al., Photoluminescence from Chemically Exfoliated MoS₂. *Nano Letters*. **2011**, *11*, 5111-5116.
91. Han, J. H.; Lee, S.; Yoo, D.; Lee, J. H.; Cheon, J., Unveiling Chemical Reactivity and Structural Transformation of Two-Dimensional Layered Nanocrystals. *Journal of Chemistry Society Reviews*. **2013**, *135*, 3736-3739.
92. Murray, C. B.; Norris, D. J.; Bawendi, M. G., Synthesis and Characterization of Nearly Monodisperse CdE (E=S, Se, Te) Semiconductor Nanocrystallites. *Journal of the American Chemical Society*. **1993**, *115*, 8706-8715.
93. Bodnarchuk, M. I.; Kovalenko, M. V.; Heiss, W.; Talapin, D. V., Energetic and Entropic Contributions to Self-Assembly of Binary Nanocrystal Superlattices: Temperature as the Structure-Directing Factor. *Journal of the American Chemical Society*. **2010**, *132*, 11967-11977.
94. Murray, C. B.; Kagan, C. R.; Bawendi, M. G., Self-Organization of CdSe Nanocrystallites into Three-Dimensional Quantum Dot Superlattices. *Science*. **1995**, *270*, 1335-1338.
95. Shi, H.; Yan, R.; Bertolazzi, S.; Brivio, J.; Gao, B., et al., Exciton Dynamics in Suspended Monolayer and Few-Layer MoS₂ 2D Crystals. *ACS Nano*. **2012**, *7*, 1072-1080.
96. Beal, A. R.; Knights, J. C.; Liang, W. Y., Transmission Spectra of Some Transition Metal Dichalcogenides: I. Group IVA: Octahedral Coordination. *Journal of Physics: Condensed Matter*. **1972**, *5*, 3531-3539.
97. Reshak, A. H.; Auluck, S., Electronic and optical properties of the 1T phases of TiS₂, TiSe₂ and TiTe₂. *Physical Review B*. **2003**, *68*, 245113.
98. Yun, W. S.; Han, S. W.; Hong, S. C.; Kim, I. G.; Lee, J. D., Thickness and Strain Effects on Electronic Structures of Transition Metal Dichalcogenides: 2H-MX₂ Semiconductors (M=Mo, W; X= S, Se, Te). *Physical Review B*. **2012**, *85*, 033305.
99. Lim, S. J.; Kim, W.; Shin, S. K., Surface-Dependent, Ligand-Mediated Photochemical Etching of CdSe Nanoplatelets. *Journal of the American Chemical Society*. **2012**, *134*, 7576-7579.

100. Thomson, J. W.; Cademartiri, L.; MacDonald, M.; Petrov, S.; Calestani, G., et al., Ultrathin Bi₂S₃ Nanowires: Surface and Core Structure at the Cluster-Nanocrystal Transition. *Journal of the American Chemical Society*. **2010**, *132*, 9058-9068.
101. Park, K. H.; Choi, J.; Oh, D. H.; Ahn, J. R.; Son, S. U., Unstable Single-Layered Colloidal TiS₂ Nanodisks. *Small*. **2008**, *7*, 945-950.
102. Fang, C. M.; Degroot, R. A.; Hass, C., Bulk and Surface Electronic Structure of 1T-TiS₂ and 1T-TiSe₂. *Physical Review B*. **1997**, *56*, 4455-4463.
103. Das, S.; Chen, H.-Y.; Penumatcha, A. V.; Appenzeller, J., High Performance Multilayer MoS₂ Transistors with Scandium Contacts. *Nano Letters*. **2012**, *13*, 100-105.
104. Janisch, C.; Wang, Y.; Ma, D.; Mehta, N.; Elias, A. L., et al., Extraordinary Second Harmonic Generation in Tungsten Disulfide Monolayers. *Scientific Reports*. **2014**, *4*.
105. Splendiani, A.; Sun, L.; Zhang, Y.; Li, T.; Kim, J., et al., Emerging Photoluminescence in Monolayer MoS₂. *Nano Letters*. **2010**, *10*, 1271-1275.
106. Liang, W. Y., Optical anisotropy in layer compounds. *Journal of Physics C: Solid State Physics*. **1973**, *6*, 551.
107. Hualing Zeng, J. D., Wang Yao, Di Xiao and Xiaodong Cui, Valley polarization in MoS₂ monolayers by optical pumping. *Nature Nanotechnology*. **2012**, *7*.
108. Xia, F.; Wang, H.; Xiao, D.; Dubey, M.; Ramasubramaniam, A., Two-dimensional material nanophotonics. *Nature Photonics*. **2014**, *8*, 899.
109. Helveg, S.; Lauritsen, J. V.; Lægsgaard, E.; Stensgaard, I.; Nørskov, J. K., et al., Atomic-Scale Structure of Single-Layer MoS₂ Nanoclusters. *Physical Review Letters*. **2000**, *84*, 951-954.
110. Kundu, S.; Hill, J. P.; Richards, G. J.; Ariga, K.; Khan, A. H., et al., Ultranarrow PbS Nanorod-Nematic Liquid Crystal Blend for Enhanced Electro-optic Properties. *ACS Applied Materials & Interfaces*. **2010**, *2*, 2759-2766.
111. Grasso, V., *Electronic Structure and Electronic Transitions in Layered Materials*; D. Reidel Publishing Company: Dordrecht, Holland, 1986.
112. Kamal, J. S.; Gomes, R.; Hens, Z.; Karvar, M.; Neyts, K., et al., Direct determination of absorption anisotropy in colloidal quantum rods. *Physical Review B*. **2012**, *85*, 035126.
113. Kautek, W.; Decker, F.; Gerischer, H., Optical Anisotropy of Transition Metal Dichalcogenides. A Photoelectrochemical Determination. *Physica Status Solidi B: Basic Solid State Physics*. **1984**, *122*, 651-659.

114. Mantegazza, F.; Caggioni, M.; Jimenez, M. L.; Bellini, T., Anomalous field-induced particle orientation in dilute mixtures of charged rod-like and spherical colloids. *Nature Physics*. **2005**, *1*, 103-106.
115. Stoyl P. Stoylov, M. V. S., *Molecular and Colloidal Electro-Optics*; CRC Press: Boca Raton Florida, 2007; Vol. 134.
116. Kraemer, U.; Hoffmann, H., Electric birefringence measurements in aqueous polyelectrolyte solutions. *Macromolecules*. **1991**, *24*, 256-263.
117. Arcenegui, J. J.; García-Sánchez, P.; Morgan, H.; Ramos, A., Electro-orientation and electrorotation of metal nanowires. *Physical Review E*. **2013**, *88*, 063018.
118. Carrasco, B.; Pérez Belmonte, A.; López Martínez, M. C.; García de la Torre, J., Transient Orientation and Electrooptical Properties of Axially Symmetric Macromolecules in an Electric Field of Arbitrary Strength. *The Journal of Physical Chemistry*. **1996**, *100*, 9900-9905.
119. Asami, K., Characterization of heterogeneous systems by dielectric spectroscopy. *Progress in Polymer Science*. **2002**, *27*, 1617-1659.
120. Kohn, P.; Schröter, K.; Thurn-Albrecht, T., Interfacial Polarization and Field-Induced Orientation in Nanostructured Soft-Ion Conductors. *Physical Review Letters*. **2009**, *102*, 216101.
121. Saville, D. A.; Bellini, T.; Degiorgio, V.; Mantegazza, F., An extended Maxwell–Wagner theory for the electric birefringence of charged colloids. *The Journal of Chemical Physics*. **2000**, *113*, 6974-6983.
122. Zeng, H.; Liu, G.-B.; Dai, J.; Yan, Y.; Zhu, B., et al., Optical Signature of Symmetry Variations and Spin-Valley Coupling in Atomically Thin Tungsten Dichalcogenides. *Scientific Reports*. **2013**, *3*.
123. Li, H.; Zhang, Q.; Yap, C. C. R.; Tay, B. K.; Edwin, T. H. T., et al., From Bulk to Monolayer MoS₂: Evolution of Raman Scattering. *Advanced Functional Materials*. **2012**, *22*, 1385-1390.
124. Ghatak, S.; Pal, A. N.; Ghosh, A., Nature of Electronic States in Atomically Thin MoS₂ Field-Effect Transistors. *ACS Nano*. **2011**, *5*, 7707-7712.
125. Chen, R. S.; Tang, C. C.; Shen, W. C.; Huang, Y. S., Thickness-Dependent Electrical Conductivities and Ohmic Contacts in Transition Metal Dichalcogenides Multilayers. *Nanotechnology*. **2014**, *25*, 415706.
126. Ding, Y.; Wang, Y.; Ni, J.; Shi, L.; Shi, S., et al., First principles study of structural, vibrational and electronic properties of graphene-like MX₂ (M=Mo, Nb, W, Ta; X=S, Se, Te) monolayers. *Physica B: Condensed Matter*. **2011**, *406*, 2254-2260.

127. Muratore, C.; Varshney, V.; Gengler, J. J.; Hu, J.; Bultman, J. E., et al., Thermal Anisotropy in Nano-Crystalline MoS₂ Thin Films. *Physical Chemistry Chemical Physics*. **2014**, *16*, 1008-1014.
128. Jiang, J.-W.; Zhuang, X.; Rabczuk, T., Orientation Dependent Thermal Conductance in Single-Layer MoS₂. *Scientific Reports*. **2013**, *3*.
129. Nayak, A. P.; Bhattacharyya, S.; Zhu, J.; Liu, J.; Wu, X., et al., Pressure-Induced Semiconducting to Metallic Transition in Multilayered Molybdenum Disulphide. *Nature Communications*. **2014**, *5*.
130. Dou, X.; Ding, K.; Jiang, D.; Sun, B., Tuning and Identification of Interband Transitions in Monolayer and Bilayer Molybdenum Disulfide Using Hydrostatic Pressure. *ACS Nano*. **2014**, *8*, 7458-7464.
131. Zhang, X.; Han, W. P.; Wu, J. B.; Milana, S.; Lu, Y., et al., Raman Spectroscopy of Shear and Layer Breathing Modes in Multilayer MoS₂. *Physical Review B*. **2013**, *87*, 115413.
132. Kumar, N.; He, J.; He, D.; Wang, Y.; Zhao, H., Charge Carrier Dynamics in Bulk MoS₂ Crystal Studied by Transient Absorption Microscopy. *Journal of Applied Physics*. **2013**, *113*, 133703-133708.
133. Hodak, J. H.; Henglein, A.; Hartland, G. V., Size Dependent Properties of Au Particles: Coherent Excitation and Dephasing of Acoustic Vibrational Modes. *The Journal of Chemical Physics*. **1999**, *111*, 8613-8621.
134. Gambetta, A.; Manzoni, C.; Menna, E.; Meneghetti, M.; Cerullo, G., et al., Real-Time Observation of Nonlinear Coherent Phonon Dynamics in Single-Walled Carbon Nanotubes. *Nat Phys*. **2006**, *2*, 515-520.
135. Krauss, T. D.; Wise, F. W., Coherent Acoustic Phonons in a Semiconductor Quantum Dot. *Physical Review Letters*. **1997**, *79*, 5102-5105.
136. Zeiger, H. J.; Vidal, J.; Cheng, T. K.; Ippen, E. P.; Dresselhaus, G., et al., Theory for Displacive Excitation of Coherent Phonons. *Physical Review B*. **1992**, *45*, 768-778.
137. Yee, K. J.; Lee, K. G.; Oh, E.; Kim, D. S.; Lim, Y. S., Coherent Optical Phonon Oscillations in Bulk GaN Excited by Far below the Band Gap Photons. *Physical Review Letters*. **2002**, *88*, 105501.
138. Hu, M.; Wang, X.; Hartland, G. V.; Mulvaney, P.; Juste, J. P., et al., Vibrational Response of Nanorods to Ultrafast Laser Induced Heating: Theoretical and Experimental Analysis. *Journal of the American Chemical Society*. **2003**, *125*, 14925-14933.

139. Hartland, G. V., Coherent Vibrational Motion in Metal Particles: Determination of the Vibrational Amplitude and Excitation Mechanism. *The Journal of Chemical Physics*. **2002**, *116*, 8048-8055.
140. Fan, H. M.; Ni, Z. H.; Feng, Y. P.; Fan, X. F.; Kuo, J. L., et al., Anisotropy of Electron-Phonon Coupling in Single Wurtzite CdS Nanowires. *Applied Physics Letters*. **2007**, *91*, 19711-19713.
141. Creti, A.; Anni, M.; Zavelani-Rossi, M.; Lanzani, G.; Lomascolo, M., Ultrafast Carrier Dynamics and Confined Acoustic Phonons in CdSe Nanorods. *Journal of Optics A*. **2008**, *10*, 064004.
142. Cherevko, S. A.; Fedorov, A. V.; Artemyev, M. V.; Prudnikau, A. V.; Baranov, A. V., Anisotropy of Electron-Phonon Interaction in Nanoscale CdSe Platelets as Seen Via Off-Resonant and Resonant Raman Spectroscopy. *Physical Review B*. **2013**, *88*, 041303.
143. Basu, J.; Bhattacharyya, T., Microelectromechanical Resonators for Radio Frequency Communication Applications. *Microsyst Technol*. **2011**, *17*, 1557-1580.
144. Ge, S.; Liu, X.; Qiao, X.; Wang, Q.; Xu, Z., et al., Coherent Longitudinal Acoustic Phonon Approaching THz Frequency in Multilayer Molybdenum Disulphide. *Scientific Reports*. **2014**, *4*.
145. Wang, H.; Zhang, C.; Rana, F. In *Ultrafast Carrier Dynamics in Single and Few layer MoS₂ studied by Optical Pump Probe Technique*, Optical Society of America, **2013**, 2.
146. Yu, Y. G.; Ross, N. L., First-Principles Study on Thermodynamic Properties and Phase Transitions in TiS₂. *Journal of Physics: Condensed Matter*. **2011**, *23*, 055401.
147. Yan-Bin, Q.; Guo-Hua, Z.; Di, L.; Jiang-Long, W.; Xiao-Ying, Q., et al., Strongly Correlated Effect in TiS₂. *Chinese Physics Letters*. **2007**, *24*, 1050.
148. Chen, C. H.; Fabian, W.; Brown, F. C.; Woo, K. C.; Davies, B., et al., Angle-Resolved Photoemission Studies of the Band Structure of TiSe₂ and TiS₂. *Physical Review B*. **1980**, *21*, 615-624.
149. Sánchez, K.; Palacios, P.; Wahnón, P., Electronic Structure of Bulk- and Na-Intercalated TiS₂ Determined from a GGA+U Study with the Hubbard Terms Obtained *Ab Initio*. *Physical Review B*. **2008**, *78*, 235121.
150. Kresse, G.; Furthmüller, J., Efficiency of *Ab-Initio* total Energy Calculations for Metals and Semiconductors Using a Plane-Wave Basis Set. *Computational Materials Science*. **1996**, *6*, 15-50.

151. Kresse, G.; Hafner, J., Ab Initio Molecular Dynamics for Liquid Metals. *Physical Review B*. **1993**, *47*, 558-561.
152. Kresse, G.; Hafner, J., Ab Initio Molecular-Dynamics Simulation of the Liquid-Metamorphous-Semiconductor Transition in Germanium. *Physical Review B*. **1994**, *49*, 14251-14269.
153. Blöchl, P. E., Projector Augmented-Wave Method. *Physical Review B*. **1994**, *50*, 17953-17979.
154. Kresse, G.; Joubert, D., From Ultrasoft Pseudopotentials to the Projector Augmented-Wave Method. *Physical Review B*. **1999**, *59*, 1758-1775.
155. Perdew, J. P.; Burke, K.; Ernzerhof, M., Generalized Gradient Approximation Made Simple. *Physical Review Letters*. **1996**, *77*, 3865-3868.
156. Monkhorst, H. J.; Pack, J. D., Special Points for Brillouin-Zone Integrations. *Physical Review B*. **1976**, *13*, 5188-5192.
157. Dong, L.; Namburu, R.; O'Regan, T.; Dubey, M.; Dongare, A., Theoretical study on Strain-Induced Variations in Electronic Properties of Monolayer MoS₂. *J Mater Sci*. **2014**, *49*, 6762-6771.
158. Shi, H.; Pan, H.; Zhang, Y.-W.; Yakobson, B. I., Quasiparticle Band Structures and Optical Properties of Strained Monolayer MoS₂ and WS₂. *Physical Review B*. **2013**, *87*, 155304.
159. Gajdoš, M.; Hummer, K.; Kresse, G.; Furthmüller, J.; Bechstedt, F., Linear Optical Properties in the Projector-Augmented Wave Methodology. *Physical Review B*. **2006**, *73*, 045112.
160. Reiss, P.; Protière, M.; Li, L., Core/Shell Semiconductor Nanocrystals. *Small*. **2009**, *5*, 154-168.
161. Smith, A. M.; Nie, S., Semiconductor Nanocrystals: Structure, Properties, and Band Gap Engineering. *Accounts of Chemical Research*. **2010**, *43*, 190-200.
162. Milliron, D. J.; Hughes, S. M.; Cui, Y.; Manna, L.; Li, J., et al., Colloidal nanocrystal heterostructures with linear and branched topology. *Nature*. **2004**, *430*, 190-195.
163. Kriegel, I.; Wisnet, A.; Srimath Kandada, A. R.; Scotognella, F.; Tassone, F., et al., Cation exchange synthesis and optoelectronic properties of type II CdTe-Cu_{2-x}Te nano-heterostructures. *Journal of Materials Chemistry C*. **2014**, *2*, 3189-3198.

164. Hassan, Y.; Chuang, C.-H.; Kobayashi, Y.; Coombs, N.; Gorantla, S., et al., Synthesis and Optical Properties of Linker-Free TiO₂/CdSe Nanorods. *The Journal of Physical Chemistry C*. **2014**, *118*, 3347-3358.
165. Tvrdy, K.; Frantsuzov, P. A.; Kamat, P. V., Photoinduced electron transfer from semiconductor quantum dots to metal oxide nanoparticles. *Proceedings of the National Academy of Sciences*. **2011**, *108*, 29-34.
166. Dahl, M.; Liu, Y.; Yin, Y., Composite Titanium Dioxide Nanomaterials. *Chemical Reviews*. **2014**, *114*, 9853-9889.
167. Luo, J.; Ma, L.; He, T.; Ng, C. F.; Wang, S., et al., TiO₂/(CdS, CdSe, CdSeS) Nanorod Heterostructures and Photoelectrochemical Properties. *The Journal of Physical Chemistry C*. **2012**, *116*, 11956-11963.
168. Acharya, K. P.; Hewa-Kasakarage, N. N.; Alabi, T. R.; Nemitz, I.; Khon, E., et al., Synthesis of PbS/TiO₂ Colloidal Heterostructures for Photovoltaic Applications. *The Journal of Physical Chemistry C*. **2010**, *114*, 12496-12504.
169. Carvalho, A.; Ribeiro, R. M.; Castro Neto, A. H., Band nesting and the optical response of two-dimensional semiconducting transition metal dichalcogenides. *Physical Review B*. **2013**, *88*, 115205.
170. Britnell, L.; Ribeiro, R. M.; Eckmann, A.; Jalil, R.; Belle, B. D., et al., Strong Light-Matter Interactions in Heterostructures of Atomically Thin Films. *Science*. **2013**.
171. Hamza, E.-K.; Larbi El, F.; Jamal, S.; Allal, C., Electronic and Optical Properties of TiS₂ Determined from Generalized Gradient Approximation Study. *Chinese Physics Letters*. **2015**, *32*, 096102.
172. Lee, P. A.; Said, G.; Davis, R.; Lim, T. H., On the optical properties of some layer compounds. *Journal of Physics and Chemistry of Solids*. **1969**, *30*, 2719-2729.
173. Rossi, D.; Han, J. H.; Yoo, D.; Dong, Y.; Park, Y., et al., Photoinduced Separation of Strongly Interacting 2-D Layered TiS₂ Nanodiscs in Solution. *The Journal of Physical Chemistry C*. **2014**, *118*, 12568-12573.
174. Kaur, K.; Singh, C. V., Amorphous TiO₂ as a Photocatalyst for Hydrogen Production: A DFT Study of Structural and Electronic Properties. *Energy Procedia*. **2012**, *29*, 291-299.
175. Oku, T.; Kakuta, N.; Kobayashi, K.; Suzuki, A.; Kikuchi, K., Fabrication and characterization of TiO₂-based dye-sensitized solar cells. *Progress in Natural Science: Materials International*. **2011**, *21*, 122-126.

176. Sim, S.; Park, J.; Song, J.-G.; In, C.; Lee, Y.-S., et al., Exciton dynamics in atomically thin MoS₂: Interexcitonic interaction and broadening kinetics. *Physical Review B*. **2013**, *88*, 075434.
177. Cunningham, P. D.; McCreary, K. M.; Hanbicki, A. T.; Currie, M.; Jonker, B. T., et al., Charge Trapping and Exciton Dynamics in Large-Area CVD Grown MoS₂. *The Journal of Physical Chemistry C*. **2016**, *120*, 5819-5826.
178. Seo, M.; Yamaguchi, H.; Mohite, A. D.; Boubanga-Tombet, S.; Blancon, J.-C., et al., Ultrafast Optical Microscopy of Single Monolayer Molybdenum Disulfide Flakes. *Scientific Reports*. **2016**, *6*, 21601.
179. Nedelcu, G.; Protesescu, L.; Yakunin, S.; Bodnarchuk, M. I.; Grotevent, M. J., et al., Fast Anion-Exchange in Highly Luminescent Nanocrystals of Cesium Lead Halide Perovskites (CsPbX₃, X = Cl, Br, I). *Nano Letters*. **2015**, *15*, 5635-5640.
180. Shim, M.; Guyot-Sionnest, P., Permanent dipole moment and charges in colloidal semiconductor quantum dots. *The Journal of Chemical Physics*. **1999**, *111*, 6955-6964.
181. Klimov, V. I., Optical Nonlinearities and Ultrafast Carrier Dynamics in Semiconductor Nanocrystals. *The Journal of Physical Chemistry B*. **2000**, *104*, 6112-6123.
182. Nootz, G.; Padilha, L. A.; Olszak, P. D.; Webster, S.; Hagan, D. J., et al., Role of Symmetry Breaking on the Optical Transitions in Lead-Salt Quantum Dots. *Nano Letters*. **2010**, *10*, 3577-3582.
183. Bekenstein, Y.; Koscher, B. A.; Eaton, S. W.; Yang, P.; Alivisatos, A. P., Highly Luminescent Colloidal Nanoplates of Perovskite Cesium Lead Halide and Their Oriented Assemblies. *Journal of the American Chemical Society*. **2015**, *137*, 16008-16011.
184. Stranks, S. D.; Eperon, G. E.; Grancini, G.; Menelaou, C.; Alcocer, M. J. P., et al., Electron-Hole Diffusion Lengths Exceeding 1 Micrometer in an Organometal Trihalide Perovskite Absorber. *Science*. **2013**, *342*, 341-344.
185. Ramasamy, P.; Lim, D. H.; Kim, B.; Lee, S. H.; Lee, M. S., et al., All-inorganic cesium lead halide perovskite nanocrystals for photodetector applications. *Chemical Communications*. **2016**, *52*, 2067-2070.
186. Beaulac, R.; Archer, P. I.; Ochsenbein, S. T.; Gamelin, D. R., Mn²⁺-Doped CdSe Quantum Dots: New Inorganic Materials for Spin-Electronics and Spin-Photonics. *Advanced Functional Materials*. **2008**, *18*, 3873-3891.
187. Mir, W. J.; Jagadeeswararao, M.; Das, S.; Nag, A., Colloidal Mn-Doped Cesium Lead Halide Perovskite Nanoplatelets. *ACS Energy Letters*. **2017**, *2*, 537-543.

188. Liu, W.; Lin, Q.; Li, H.; Wu, K.; Robel, I., et al., Mn²⁺-Doped Lead Halide Perovskite Nanocrystals with Dual-Color Emission Controlled by Halide Content. *Journal of the American Chemical Society*. **2016**, *138*, 14954-14961.
189. Yang, Y.; Chen, O.; Angerhofer, A.; Cao, Y. C., On Doping CdS/ZnS Core/Shell Nanocrystals with Mn. *Journal of the American Chemical Society*. **2008**, *130*, 15649-15661.
190. Barrows, C. J.; Vlaskin, V. A.; Gamelin, D. R., Absorption and Magnetic Circular Dichroism Analyses of Giant Zeeman Splittings in Diffusion-Doped Colloidal Cd_{1-x}Mn_xSe Quantum Dots. *The Journal of Physical Chemistry Letters*. **2015**, *6*, 3076-3081.
191. Fainblat, R.; Barrows, C. J.; Hopmann, E.; Siebeneicher, S.; Vlaskin, V. A., et al., Giant Excitonic Exchange Splittings at Zero Field in Single Colloidal CdSe Quantum Dots Doped with Individual Mn²⁺ Impurities. *Nano Letters*. **2016**, *16*, 6371-6377.
192. Beaulac, R.; Schneider, L.; Archer, P. I.; Bacher, G.; Gamelin, D. R., Light-Induced Spontaneous Magnetization in Doped Colloidal Quantum Dots. *Science*. **2009**, *325*, 973-976.
193. Rice, W. D.; Liu, W.; Pinchetti, V.; Yakovlev, D. R.; Klimov, V. I., et al., Direct Measurements of Magnetic Polarons in Cd_{1-x}Mn_xSe Nanocrystals from Resonant Photoluminescence. *Nano Letters*. **2017**, *17*, 3068-3075.
194. Wu, K.; Liang, G.; Shang, Q.; Ren, Y.; Kong, D., et al., Ultrafast Interfacial Electron and Hole Transfer from CsPbBr₃ Perovskite Quantum Dots. *Journal of the American Chemical Society*. **2015**, *137*, 12792-12795.
195. Shi, H.; Du, M.-H., Shallow halogen vacancies in halide optoelectronic materials. *Physical Review B*. **2014**, *90*, 174103.
196. Buin, A.; Comin, R.; Xu, J.; Ip, A. H.; Sargent, E. H., Halide-Dependent Electronic Structure of Organolead Perovskite Materials. *Chemistry of Materials*. **2015**, *27*, 4405-4412.
197. Mondal, N.; Samanta, A., Complete ultrafast charge carrier dynamics in photo-excited all-inorganic perovskite nanocrystals (CsPbX₃). *Nanoscale*. **2017**, *9*, 1878-1885.
198. Maiti, S.; Chen, H.-Y.; Park, Y.; Son, D. H., Evidence for the Ligand-Assisted Energy Transfer from Trapped Exciton to Dopant in Mn-Doped CdS/ZnS Semiconductor Nanocrystals. *The Journal of Physical Chemistry C*. **2014**, *118*, 18226-18232.
199. Wei, K.; Zheng, X.; Cheng, X.; Shen, C.; Jiang, T., Observation of Ultrafast Exciton-Exciton Annihilation in CsPbBr₃ Quantum Dots. *Advanced Optical Materials*. **2016**, *4*, 1993-1997.